Composite Contact Metallization on SiC for High Temperature Applications in Air

Except where reference is made to the work of others, the work described in this dissertation is my own or was done in collaboration with my advisory committee. This dissertation does not include proprietary or classified information.

Adetayo V. Adedeji

Certificate of Approval:

Chin-Che Tin Professor Department of Physics	John R. Williams, Chair Professor Department of Physics
Jianjun Dong Associate Professor Department of Physics	Minseo Park Assistant Professor Department of Physics

Stephen L. McFarland
Acting Dean, Graduate School

COMPOSITE CONTACT METALLIZATION ON SiC FOR HIGH TEMPERATURE APPLICATIONS IN AIR

Adetayo V. Adedeji

A Dissertation

Submitted to

the Graduate Faculty of

Auburn University

in Partial Fulfillment of the

Requirements for the

Degree of

Doctor of Philosophy

Auburn, Alabama
August 8, 2005

Composite Contact Metallization on SiC for

High Temperature Applications in Air

Adetayo V. Adedeji

Permission is granted to Auburn University to make copies of this thesis at its discretion, upon the request of individuals or institutions and at their expense. The author reserves all publication rights.

____
Signature of Author

____
Date of Graduation

Dissertation Abstract

Composite Contact Metallization on SiC for High Temperature Applications in Air

Adetayo V. Adedeji

Doctor of Philosophy, August 8, 2005
(B.S., University of Ilorin, Nigeria, 1989)
(DICTP, International Center for Theoretical Physics, Italy, 1994)
(M.S., Obafemi Awolowo University, Nigeria, 1997)

204 Typed Pages

Directed by John R. Williams

Composite ohmic and Schottky contacts fabricated on 4H-SiC for applications in air at 350°C are described and evaluated in this study. The ohmic contacts were fabricated on p^+ implanted and n^+ epitaxial materials, while the Schottky contacts were on n^- epilayers.

These contacts were protected from the harsh environment with the following metallization layers: Ta-Si-N served as diffusion/oxidation barrier, Pt-N sputter-deposited at 250°C promoted adhesion between the diffusion barrier layer and the Au cap layer and it also acts as a barrier to Au diffusion. A gold cap layer was deposited for the purpose of wirebonding to the device or die attach to a carrier.

The composite contact's electrical and physical characteristics were monitored as a function of annealing time in air at 350°C. For the ohmic contact, characteristics such as the specific contact resistance and SiC sheet resistance determined from TLM measurements were monitored with time of anneal. Contact parameters of nickel ohmic contact on heavily implanted p^+4H-SiC materials were very stable up to 4000 hours at 350°C in air. 70-30 wt% Al-Ti ohmic contacts

on implanted p^+, 80-20 wt% Ni-Cr and Ni ohmic contacts on epitaxial n^+4H-SiC were also studied.

Current density - voltage and capacitance - voltage characteristics of nickel silicide and Ta-Si-N schottky contacts were studied as a function of annealing time in air. Parameters such as the barrier height and ideality factor of the devices were monitored and found to be stable as the devices were annealed in air.

Adhesion characteristics of the metallization stack (barrier layer, Pt layer and Au layer) on thermal oxides, Schottky contacts and ohmic contacts were investigated in this study. All the contacts have good adhesion to the metallization as fabricated except for the nickel ohmic contacts that needed Ar ion cleaning to improve its adhesion to the metallization stack.

In all cases, inter-diffusion within the metallization and oxidation of the contacts were monitored with RBS (Rutherford backscattering spectrometry) and AES (Auger electron spectroscopy).

ACKNOWLEDGMENTS

I give thanks to God for the gift of life, good health and the opportunity to be able to take part in this study.

The guidance and support of my advisor, professor John Williams, throughout the period of my graduate study at Auburn University are acknowledged and highly appreciated. Without his wisdom, patience and persistence, it would be impossible to achieve the goals of this study.

I am indebted to Dr. Claude Ahyi, a post-doctoral fellow in our laboratory, for his contributions and useful discussion during the course of this work. The assistance of Dr. Shurui Wang, also a post-doctoral fellow in our laboratory, are appreciated. Valuable contributions of Mrs. Tamara Isaac-Smith for the initiation and successful completion of this work are acknowledged with gratiude. The contributions of Mr. Max Cichon in building and maintaining essential equipment needed for the success of this work - including the heating system used during platinum sputter-deposition - are highly appreciated.

This acknowledgement will fall short without acknowledging the support, encouragement, and assistance of my beloved sweetheart, Dolapo Abimbola Adedeji, during these years of my study. I truly appreciate our boys, Jethro and Enoch, with thanks to the Lord for their endurance during the period of this study.

Style manual or journal used Transactions of the American Mathematical Society (together with the style known as "auphd"). Bibliograpy follows the style used by the American Physical Society.

Computer software used The document preparation package TEX (specifically LATEX) together with the departmental style-file `auphd.sty`.

TABLE OF CONTENTS

LIST OF FIGURES x

LIST OF TABLES xvi

1 GENERAL INTRODUCTION AND SILICON CARBIDE 1
1.1 General Introduction 1
1.1.1 Why This Work? 1
1.1.2 Objectives 2
1.1.3 To Accomplish the Objectives 3
1.2 Silicon Carbide 6
1.2.1 Introduction 6
1.2.2 Crystal Structure 8
1.2.3 Semiconducting Properties 9
1.2.4 Devices and Applications 11

2 METAL-SEMICONDUCTOR CONTACTS AND DIFFUSION BARRIERS 19
2.1 Metal-Semiconductor Contacts 19
2.1.1 General Information 19
2.1.2 Metal-SiC Contacts 29
2.2 Diffusion and Oxidation Barriers 41
2.2.1 Diffusion in Solids 41
2.2.2 Thermodynamics of Diffusion 46
2.2.3 Diffusion Barriers 52

3 ANALYTICAL TECHNIQUES 61
3.1 Electrical Analysis 61
3.1.1 Sheet Resistance Measurement 61
3.1.2 Contact Resistance 64
3.1.3 Linear Transmission Line Model Measurement 66
3.1.4 I-V Charateristics of Schottky Diodes 70
3.1.5 C-V Charateristics of Schottky Diodes 74
3.2 Physical Analysis 77
3.2.1 Rutherford Backscattering Spectrometery (RBS) 77
3.2.2 Auger Electron Spectroscopy (AES) 92
3.2.3 X-ray Photoelectron Spectroscopy (XPS) [166] 97
3.2.4 X-ray Diffraction (XRD) 99
3.3 Mechanical Analysis 102
3.3.1 Introduction 102

4 EXPERIMENTAL PROCEDURES 106
4.1 Standard Procedures 106
4.1.1 Sample Cleaning 106
4.1.2 Photolithography 108
4.1.3 Sputter-deposition 110
4.1.4 Annealing System 111
4.2 Device Fabrication and Measurements 114
4.2.1 Ohmic Contact Fabrication 114
4.2.2 Schottky Contact Fabrication 116
4.2.3 Protective Stack Fabrication and Device Mesurements 118
4.2.4 Wirebonding and Chip Brazing 122
4.2.5 Thermal Aging of Samples 124
4.2.6 Measurements 125

5 RESULTS AND DISCUSSION 128
5.1 The Choice of Barrier Layer Material 128
5.1.1 Silicide Barrier Layer 128
5.1.2 Structure of Ta-Si-N 133
5.2 Results on Ohmic Contacts 133
5.2.1 Contacts Without Protective Metallization 133
5.2.2 Ohmic Contact with Protective Metallization 138
5.2.3 Metallization with Hot Platinum 144
5.3 Results for Schottky Contacts 153
5.3.1 I-V and C-V Results 153
5.4 Wirebonding and Brazing Results 164
5.4.1 Chip Shear Testing 164
5.4.2 Wirebond Pull and Shear Testing 168

6 CONCLUSIONS 174

BIBLIOGRAPHY 178

LIST OF FIGURES

1.1 Typical composite metallization scheme ([2]) 4

1.2 (a) basic structural unit of SiC, (b) 3C-SiC stacking sequence, (c) 4H-SiC stacking sequence and (d) 6H-SiC stacking sequence. The Jagodzinski (kkk, khkh, kkhkkh) and ABCA'B'C' notations are also shown [24]. 10

1.3 Basic FET structure [29] 12

2.1 I-V Characteristics of ohmic and schottky contact 20

2.2 Energy level diagram of metal and semiconductor 21

2.3 Energy level diagram for metal-semiconductor (n-type) contact. For $\phi_m > \phi_s$: (a) just in contact, (b) in equilibrium with built-in potential V_b, (e) forward biased with V_F, (f) reverse biased with V_r. For $\phi_m < \phi_s$: (c) just in contact and (d) at equilibrium [43, 44] 22

2.4 Energy level diagram for metal-semiconductor (p-type) contact. For $\phi_m > \phi_s$: (a) just in contact and (b) in equilibrium. For $\phi_m < \phi_s$: (c) just in contact, (d) at equilibrium with built-in potential V_b, (e) forward biased with V_F, (f) reverse biased with V_r. [43, 44] 23

2.5 Non ideal energy level diagram under forward bias V_F [45] 26

2.6 Image force. 27

2.7 Effect of image force lowering on the barrier height. 29

2.8 Effect of doping concentration on the barrier width. (a) low (b) moderate and (c) high doping [44]. 30

2.9 Atomic energy barrier as a function of atomic position [118]. 48

2.10 Diffusion barrier in multi-layer structure [140] 53

2.11 Stuffed diffusion barrier [140] 56

3.1 (a) Collinear four-point probe measurements (b) van der Pauw four-point probe measurements 62

3.2 van der pauw correction factor plot [151] 64

3.3 Plot of total contact to contact resistance as a function of inter-pad spacing [159] 67

3.4 TLM resistive network [160]. The contact width W is into the page. 68

3.5 Effect of barrier lowering on barrier height 72

3.6 Capacitance measurements under applied bias [151] 75

3.7 Close impact collision and backscattering [166] 78

3.8 $\Omega = S/d^2$ = detector solid angle. S = detector area. d = detector-target distance. t = target thickness. 81

3.9 Energy loss during inward and outward trajectory of incident particle [166] . . 83

3.10 Pelletron tandem accelerator at Auburn University 87

3.11 (a) Sources section of the accelerator. Illustrations of (b) SNICS source (c) He ion source [168] 88

3.12 Pelletron charging system [171] 90

3.13 Illustration of auger electron de-excitation [166] 93

3.14 X-ray diffraction geometry [177] 100

3.15 (a) Bragg-Brentano diffraction geometry for thin films (b) Seemann-Bohlin diffraction geometry [177] 101

3.16 Wire bond pull and shear testing 104

3.17 Chip brazed shear testing 105

4.1 (a) TLM masks (b) Diode/MOS Mask 109

4.2 Sputter-deposition system with disk sample holders having heating capability . 112

4.3 Annealing system with enlarged carbon strips showing sample 113

4.4 Sequence for ohmic contact fabrication 115

4.5 Sequence for Schottky contact fabication 117

4.6 Sequence for protective metallization on (a) ohmic contact (b) Schottky contact 119

4.7 Device cross-section of (a) ohmic (b) initial Schottky (c) new Schottky contacts 120

4.8 Modified sequence for protective metallization (a) ohmic contact with Mo lift-off (b) Schotky contact with Pt etch-back 121

4.9 (a) Large area wire bonded sample for pull and bond shaer testing (b) Chip brazed sample for die shear testing 124

4.10 (a) TLM measurement set-up (b) measurement configuration 126

4.11 (a) Current-Voltage measurement set-up (b) Capacitance-Voltage measurement set-up 127

5.1 RBS spectra of (a) SiC/Mo-Si/Pt (b) SiC/W-Si/Pt and (c) SiC/Ta-Si/Pt 129

5.2 (a) RBS spectra of SiC/Ta-Si/Ta-Si-N with 0, 2, 5, 10% nitrogen content by flow rate (b) van der Pauw sheet resistivity of Ta-Si-N from $TaSi_2$ and Ta_5Si_3 targets (c) Nitrogen aomic percentage against nitrogen flow 131

5.3 (a) Sheet resistance of Ta-Si-N on semi-insulating SiC against anneal time in air at $350°C$ (b) RBS spectra of Ta-Si-N on semi-insulating SiC for 0 and 5000hrs (b) 0% and (c) 2% nitrogen flow 132

5.4 XRD scan of Ta-Si-N with 0, 2, 5, and 10% nitrogen flow (a) as-sputtered samples (b) samples annealed in air at $350°C$ for 750hrs (c) samples annealed in evacuated quartz tube at $350°C$ for 750hrs 134

5.5 Total contact-to-contact resistance against inter-contact spacing for (a) nickel ohmic contact on p^+implanted material (b) nickel-chromium (80-20 wt%) ohmic contact on n^+epitaxial material 135

5.6 Experimental and RUMP simulated RBS spectra of (a) as-deposited nickel contact on SiC (b) nickel ohmic annealed on SiC 137

5.7 Specific contact resistance and SiC sheet resistance against annealing time for (a,c) SiC/Ni(ohmic)/Ta-Si-N/Pt-N/Au/Sn/Au (b,d) SiC/Al-Ti(ohmic)/Ta-Si-N/Pt-N/Au/Sn/Au 139

5.8 RBS spectra of p-ohmic contact after 24, 1500 and 4000hrs annealing (a) nickel ohmic contact with 2% nitrogen in the stack (b) Al-Ti ohmic contact with 2% nitrogen in the stack. 140

5.9 AES spectra for (a) as-deposited nickel contact with no nitrogen in the metallization stack (b) as-deposited nickel with 2% nitrogen in the stack (c) nickel ohmic contact with no nitrogen in the stack (d) nickel ohmic with 2% nitrogen in the stack 142

5.10 AES spectra of nickel ohmic contacts annealed in air at 350°C for 1500hrs (a) nickel ohmic contacts with no nitrogen in the stack (b) nickel ohmic contacts with 2% nitrogen in the stack 143

5.11 (a) Plots of specific contact resistance against annealing time for Ni-Cr (80-20 wt%) ohmic contacts with 2% nitrogen in the stack (b) Plots of SiC sheet resistance against annealing time for Ni-Cr (80-20 wt%) ohmic contacts with 2% nitrogen in the stack 145

5.12 (a) RBS spectra of Ni-Cr (80-20 wt%) ohmic contacts after 24 and 4000hrs annealing; AES spectra of Ni-Cr (80-20 wt%) ohmic contacts with 2% nitrogen in the stack (b) before annealing in air (c) afer annealing in air for 1500hrs 146

5.13 Total contact-to-contact resistance of (a) cold and hot Pt in the metallization stack with no nitrogen content (b) cold and hot Pt in the metallization stack with 2% nitrogen content (c) nickel ohmic contact on n^+epilayer SiC with hot Pt and 2% nitrogen in the metallization stack after different anneal times in air . 148

5.14 RBS spectrum of a nickel ohmic contact on n^+epitaxial 4H-SiC. 149

5.15 Specific contact resistance and SiC sheet resistance for nickel ohmic contacts on n^+epitaxial 4H-SiC with hot Pt and 2% nitrogen content in the metallization stack.150

5.16 Specific contact resistance and SiC sheet resistance of nickel ohmic contacts on p^+implanted 4H-SiC with hot Pt in the metallization stack. 151

5.17 Plots of (a) total contact-to-contact resistance against inter-contact spacing (b) Specific contact resistance against temperature and (c) SiC sheet resistance against temperature for nickel ohmic contact on p^+implanted 4H-SiC with 2% nitrogen in the metallization stack. 152

5.18 Nickel silicide Schottky devices (a) forward J-V dependence on annealing time (b) reverse J-V dependence on annealing time (c) barrier height and ideality factor against annealing time. 154

5.19 Bar chart of current density at -10V reverse bias for nickel silicide and Ta-Si-N Schottky devices (a) 0hr nickel silicide contacts (b) 0hr Ta-Si-N contacts (c) 1500hr nickel silicide contacts (d) 1500hr Ta-Si-N contacts 156

5.20 Nickel silicide Schottky devices (a) forward characteristics with 0% nitrogen (b) reverse characteristics with 0% nitrogen (c) forward characteristics with 2% nitrogen (d) reverse characteristics with 2% nitrogen. 157

5.21 (e) Forward characteristics with 5% nitrogen (f) Reverse characteristics with 5% nitrogen (g) Forward characteristics with 10% nitrogen (h) Reverse characteristics with 10% nitrogen. 158

5.22 Ta-Si-N Schottky devices (a) forward characteristics with 0% nitrogen (b) reverse characteristics with 0% nitrogen (c) forward characteristics with 2% nitrogen (d) reverse characteristics with 2% nitrogen. 159

5.23 (e) Forward characteristics with 5% nitrogen (f) reverse characteristics with 5% nitrogen (g) forward characteristics with 10% nitrogen (h) reverse characteristics with 10% nitrogen. 160

5.24 Nickel silicide Schottky devices (a) barrier height against annealing time (b) ideality factor against annealing time. Ta-Si-N Schottky devices (c) barrier height against annealing time (d) ideality factor against annealing time. 161

5.25 Plots of $(A/C)^2$ against applied bias for nickel silicide diodes with (a) 0% nitrogen (b) 2% nitrogen (c) 5% nitrogen (d) 10% nitrogen content in the metallization stack. 162

5.26 Plots of $(A/C)^2$ against applied bias for Ta-Si-N diodes with (a) 0% nitrogen (b) 2% nitrogen (c) 5% nitrogen (d) 10% nitrogen content in the metallization stack. 163

5.27 Nickel silicide Schottky contacts with 2% nitrogen in the metallization stack (a) RBS spectra (b) AES spectra after 1500hr anneal in air. 165

5.28 Chip shear strength with cold Pt in the metallization stack against annealing time. 166

5.29 Chip shear strength with hot Pt and 2% nitrogen in the metallization stack against annealing time. 167

5.30 Wirebond pull and shear strengths against annealing time for (a) metallization with 2% nitrogen and hot Pt on a thermal oxide (b) metallization stack with 2% nitrogen and hot Pt on a nickel silicide Schottky contact (c) Au wire failure mode and sheared wedged bond. 169

5.31 RBS and AES results for nickel ohmic contacts (a) RBS of ohmic annealed contacts (b) AES of ohmic annealed contacts (c) RBS of RIE cleaned ohmic contacts (d) AES of RIE cleaned ohmic contacts 170

5.32 RBS and AES results for nickel ohmic contacts (a) RBS of Ar ion cleaned ohmic contacts (b) AES of Ar ion cleaned ohmic contacts. 171

5.33 (a) wirebond pull and shear strength of Ar ion cleaned nickel ohmic contacts (b) picture of failed wirebond and (c) picture of good pull and shear bonding. . . 173

List of Tables

2.1 Ideal MS contanct dependence on work functions 21

2.2 Some ohmic contacts on n-type α-SiC. The layers in multi-layered contacts are seperated with slashes, layers at the surface to the interface with SiC proceed from right to left 33

2.3 Some ohmic contacts on p-type α-SiC. The layers in multi-layered contacts are seperated with slashes, layers at the surface to the interface with SiC proceed from right to left 35

2.4 Some ohmic contacts on n-type β-SiC. The layers in multi-layered contacts are seperated with slashes, layers at the surface to the interface with SiC proceed from right to left 38

2.5 Some ohmic contacts on p-type β-SiC. The layers in multi-layered contacts are seperated with slashes, layers at the surface to the interface with SiC proceed from right to left 39

2.6 Elemental diffusion barrier layer for semiconducting devices 58

2.7 Binary compound or alloy diffusion barrier layer for semiconducting devices . 59

2.8 Tenary compound or alloy diffusion barrier layer for semiconducting devices . 59

4.1 Profile of 4H-SiC purchased from Cree research Inc. 106

5.1 Various ohmic contacts fabricated in this study. The metal in contact with the SiC is on the left for the case of two or more layers. The metal sheet resistance ($M - R_{sh}$) column has values before/after contact annealing. t is the contact metal thickness. 136

CHAPTER 1

GENERAL INTRODUCTION AND SILICON CARBIDE

1.1 General Introduction

1.1.1 Why This Work?

The need for cost effective high power/high temperature semiconductor devices is essential to support advancements in power electronic and microelectronic technology that are important and much needed as we enter the 21st century.

Application areas are numerous, including [1] :

- High power switching for electric utilities, industrial motor control and electric vehicles.
- Sensors, controls and power management for the aerospace and automotive industries.
- Control electronics for the nuclear power industry and down-hole well logging in the petroleum drilling industry.

The technological implications of advanced electronics are huge, and so also are the economic implications. Millions of dollars can be saved for aircraft and spacecraft as a result of reduced space and size, higher efficiency for power/fuel usage, simpler system design, and improved long-term reliability [2]. In the automotive industry, high temperature, on-engine sensing will lead to higher fuel efficiency and less pollution of the environment.

The US Department of Defence requires wide band gap devices and component solutions for more electric ships, aircraft and vehicles, space platforms, and directed energy missions. A near-term goal for the Air Force is the development of advanced motor drives for flight control

and space vehicle applications, and converters/inverters for power conditioning applications in more electric aircraft and directed energy systems [2].

It is well known that Si-based devices are not capable of high temperature or harsh environment operation. Therefore, major improvements in system performance for extreme environments will result from the successful development of wide band gap semiconductor materials like SiC, the group III-nitrides (GaN, AlN and BN) and diamond.

Diamond technolgy is still in its early stages of development. The direct band gap nitrides are being developed for blue-UV optoelectronic applications. SiC is the most developed of the wide band gap semiconductors, and the 4H polytype is particularly suited for high power/high temperature applications because of its intrinsic properties such as larger band gap energy, higher breakdown field strength, higher saturated carrier velocity, higher thermal conductivity and more isotropic bulk carrier mobility [3]. For high power applications, 4H-SiC material properties promise higher power density (reduced size and weight), less cooling, improved operating efficiency and greater reliability.

The advantages of SiC for high power/high temperature applications can be translated into practical devices only if advanced metallization and packaging technologies are developed that allow devices to operate under extreme conditions. The development of harsh environment metallization schemes that are compatible with high temperature packaging technology is the focus of this work.

1.1.2 Objectives

The goals of this work are the following:

- Develop an advanced SiC metallization process for ohmic and Schottky contacts that is suitable for long term operation ($\sim$ 10 khr) in air at $350°C$.

- Develop a protection scheme against oxidation and metal-interdiffusion, thereby preserving the characteristics of the metal-semiconductor interface and the electrical performance of the contacts.
- Make the metallization process compatible with high temperature packaging techniques.

1.1.3 To Accomplish the Objectives

Typical composite contact layout

For high temperature/high power devices, composite (multilayer) contacts that are compatible with the techniques and procedures used for packaging (wire bonding and die attach) have been proposed [2]. A typical composite contact is shown in figure 1.1. The simplest composite contact will have three metallization layers: (1) ohmic or Schottky contact, (2) diffusion/oxidation barrier layer and (3) cap layer.

An ohmic contact must have symmetric current - voltage (I-V) characteristics with the lowest possible specific contact resistance. A Schottky contact is a metal-semiconductor contact with asymmetric I-V characteristics. It should be able to turn-on at low forward voltages, and the reverse leakage current should be as low as possible. The diffusion/oxidation barrier layer must have metal-like conduction while preventing, or at least slowing, the intermixing of stack layers as well as reducing the oxidation of the contact layer which can lead to increased contact resistance. Because of the non-ideality of the barrier layer, it may be necessary to introduce other layers (e.g., a suitable adhesion layer) in the metallization stack. Finally, the cap layer must be suitable for packaging through wirebonding or die attach.

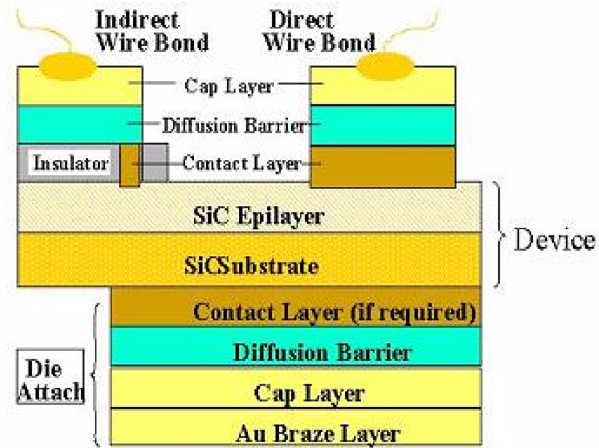

Figure 1.1: Typical composite metallization scheme ([2])

Ohmic contact

Ohmic contacts can be fabricated to either n-type or p-type SiC.

n-type ohmic contact - Nickel-based contacts on n-SiC have been more widely reported compared to other metals [4, 5, 6]. Specific contact resistance between 1×10^{-6} and $1 \times 10^{-2}\Omega - cm^2$ can be found in literature, depending on the processing method and doping concentration. Nickel-based contacts are known to be thermally stable, and so are appropriate for this work. Nickel reacts with SiC at temperatures $\geq 900°C$, forming silicides such as Ni_2Si which is an excellent ohmic contact [5, 6].

p-type ohmic contact - Aluminum based metal alloys (AlTi, NiAl, etc) are widely reported to form ohmic contacts to p-SiC [7, 8]. Al-Ti forms an ohmic contact to moderately doped p-SiC when annealed at temperatures above $800°C$ [7, 8]. A great disadvantage for the Al-based contact is the possibile oxidation of Al during long-term operation. However, ohmic contacts with excellent uniformity and reproducibility have been reported with Al-Ti alloys [9, 10, 11]. The

70-30 weight percent Al-Ti alloy is good for p-SiC ohmic contacts because of reduced spiking of Al into the SiC. The contact is more reproducible, and the contact layer/SiC interface is much smother following the contact anneal. 70-30 Wt% Al-Ti will be used in this work for ohmic contact on p-SiC, and we will investigate the thermal stability of this alloy at $350°C$ in air. Ni-based alloys will also be investigated as possible candidates for ohmic contacts to heavily doped p-SiC ($\sim 10^{20} cm^{-3}$).

Schottky contact

Nickel silicide will be sputter-deposited for Schottky contacts on n^{-}4H-SiC. Pure Ni has been considered, as well. However, Ni reacts with SiC at about $600°C$ to form nickel silicide. This reaction could affect the Schottky characteristics during the long-term thermal stability investigation we intend to carry out. Sputtered nickel silicide is expected to more stable.

Diffusion/oxidation barrier layer

An effective diffusion barrier is necessary, especially where it is impossible to eliminate thermodynamic driving forces for reactions. An extensive body of literature exists for barrier layers used in silicon VLSI/ULSI applications. Transition metal silicides (e.g. $TaSi_2$, $MoSi_2$, WSi_2) have been used successfully. These silicides will be studied as possible diffusion barriers in SiC composite contacts.

The rate of mass transport through a polycrystalline material is noticeably enhanced by migration along grain boundaries. The silicides we will consider for diffusion barriers are sometimes polycrystalline or amorphous depending on the deposition process. Diffusion through a polycrystalline material can be reduced significantly by ”stuffing” the grain boundaries with

small elements such as nitrogen or carbon [139]. Grain boundaries are not a problem if the materials are amorphous; however, crystallization during long-term operation at elevated temperature is a potential problem.

We will sputter the silicide barrier layers in Ar/N_2 gas mixtures in order to produce amorphous barriers or to improve the properties of polycrystalline diffusion/oxidation barrier layers.

Cap layer and packaging issues

Layers above the barrier layer have to be oxidation/corrosion resistant and must be compatible with the diffusion barrier (adhesion and stability). Cap layers need to be suitable for the envisioned packaging sheme: e.g. wirebonding, die attach or brazing.

All composite metallization schemes will be developed for $350°C$ operation in air. Composite contact stacks will be evaluated electrically (LTLM, I-V, C-V) and physically (RBS, AES/XPS, XRD). Mechanical techniques (shear and pull testing) will be used to evaluate the durability of the wirebonds and die attachments. Devices will be subjected to temperature cycling at $350°C$ in air.

1.2 Silicon Carbide

1.2.1 Introduction

Silicon carbide, originally called mineral moissanite, has been known to exist naturally since the late 1800s. It gained attention because of its chemical, thermal and mechanical stability [12]. Based on these properties, SiC has been used largely in industry for grinding and cutting. Acheson [13] was the first to devise a method of producing SiC on a large scale, and the largest market originally was for use as an abrasive. However, other applications were soon exploited

- including cheap heating elements with long lifetimes, coating of uranium grains for the fuel elements of nuclear reactors, reinforced materials, etc. Polycrystalline SiC with binders was first used in commercial electrical devices as lightning arrestors to protect equipment from power surges [12, 13].

Major scientific interest started when crystallographers observed that hexagonal SiC is capable of crystallizing into many different forms called polytypes. ZnS is another semiconductor that occurs with similar structural variations. SiC is however unique because the semiconductor bandgap is polytype dependent, typically between 2.2 eV for cubic SiC to 3.3 eV for the wurtzite structure [12].

SiC is sometimes reffered to as both the oldest and youngest semiconductor [12]. Lossew [14] in 1907 discovered the electroluminescence of the semicondutor while experimenting with SiC crystals. The first systematic analysis of the semiconductor properties was conducted in 1945 by Busch [15] using material from the Acheson SiC crystal collections. Because of the difficulty of growing good quality single crystals at the time, progress was slow towards exploiting the semiconductor characteristics of this material.

Cree, Inc. introduced a 25 mm single crystal wafer of 6H-SiC in 1990 [16]. However, known material problems such as the existence of micropipe defects (small holes penetrating the wafers parallel to the growth direction) persisted. Micropipe diameters varied from less than one micron to tens of microns, and the micropipe density was about $10^4 cm^{-2}$. By the year 2000, noticeable improvements in wafer quality had been achieved. Seventy-five millimeter wafers with $50 - 100 \mu pipes/cm^2$ were available. Wafers with as few as $3.5 \mu pipes/cm^2$ have been reported recently [16]. In 2004, Nakamura, et al.[17] reported a modified growth method that has led to ultra-high quality SiC single crystals that are virtually dislocation free.

1.2.2 Crystal Structure

The fundamental unit of SiC has a tetrahydral structure with four nearest neighbor C atoms bonded to Si (SiC_4) or four nearest neighbor Si atoms bonded to C (CSi_4). Bonding between Si and C is primarily (88%) covalent, the rest of the bonding is ionic. [20]. Polytypism is the most remarkable feature of SiC. Polytypism may be defined as the ability of a substance to crystallize into a number of different modifications in all of which two dimensions of the unit cell are the same and the third dimension is a variable, integral multiple of a common length [12]. Two base vectors of the hexagonal unit cell are $\vec{a}_1 = \vec{a}_2 = 3.078\mathring{A}$ while the third base vector $\vec{c}$ is an integral multiple of $2.518\mathring{A}$. The difference between the polytypes is in the stacking order of the basic building blocks which are close packed Si-C tetrahedra. In all polytypes, any Si or C atom has the same first and second coordination. Every atom has four first neighbors of the other atom and twelve second neighbors of the same atom. There are over 200 known polytypes, and some polytypes do not have a repeating pattern until after hundreds of layers [21]. SiC is a bi-layer compound, above the center of a triangle formed by three Si atoms is a carbon atom. The three Si atoms form in an hexagonal network forming the first Si layer of the structure. The fouth Si atom of the tetrahydral belongs to the second layer of the Si network. The Si atom in the second layer bonds directly to the first carbon layer atoms directly above it. The atoms of the third Si layer are connected also in unilateral position to the atoms of the second carbon layer. They may occupy a position having its projection on the atom of the first Si layer or at the center of the triangle not covered by the projections of the atoms of the first carbon layer. Identical successive layers of tetrahydra are oriented either parallel or anti-parallel. Different structures arise as a result of the characteristic succession or alteration of tetrahydral layers, forming a repeating unit. If every

layer is parallel to a preceeding layer, a cubic structure is formed, but if anti-parallel, a hexagonal structure is formed [20].

The Ramsdell notation [22] for polytypes is the most common notation, while Zhadanov [23] is another notation that is sometimes used. Ramsdell notaion has a bravis lattice type of structure (H - hexagonal, C - cubic, R - rombohydral). Preceeding this letter is a number (eg. 3C, 4H, 6H), which specifies how many bi-layers form the repeating structure along the stacking direction.

The most common of SiC polytypes being developed for electronic applications are 3C (β-SiC), 4H and 6H (α-SiC). 3C-, 4H- and 6H-SiC stacking sequence are shown in figure 1.2 [24].

There is a close correlation between crystallograhpic and semiconducting properties. Even within a given polytype, some important electrical properties are nonisotropic, that is, they are strong functions of crystallographic direction (e.g. electron mobility for 6H-SiC) [25]. It is known experimentally that growth temperature [26] and pressure [27] affect polytype distribution, and impurities may also have an affect [13, 26].

1.2.3 Semiconducting Properties

Silicon carbide is a wide band gap semiconductor (E_g = 2.2-3.3 eV) like GaN (E_g = 3.4 eV) and AlN (E_g = 6.2 eV) [16], and SiC is the only known compound semiconductor that can be oxidized to form a high quality native oxide (SiO_2). Silicon carbide can be doped in-situ during growth by introducing nitrogen or phosphorous for n-type conductivity and either aluminum or boron for p-type conductivity. Doping concentration ranges from $10^{14}cm^{-3}$ to $\geq 10^{19}cm^{-3}$ [28]. Selective doping can be achieved by high energy implantation. The usual doping method for Si of thermal diffusion is not practicable for SiC because of the very low

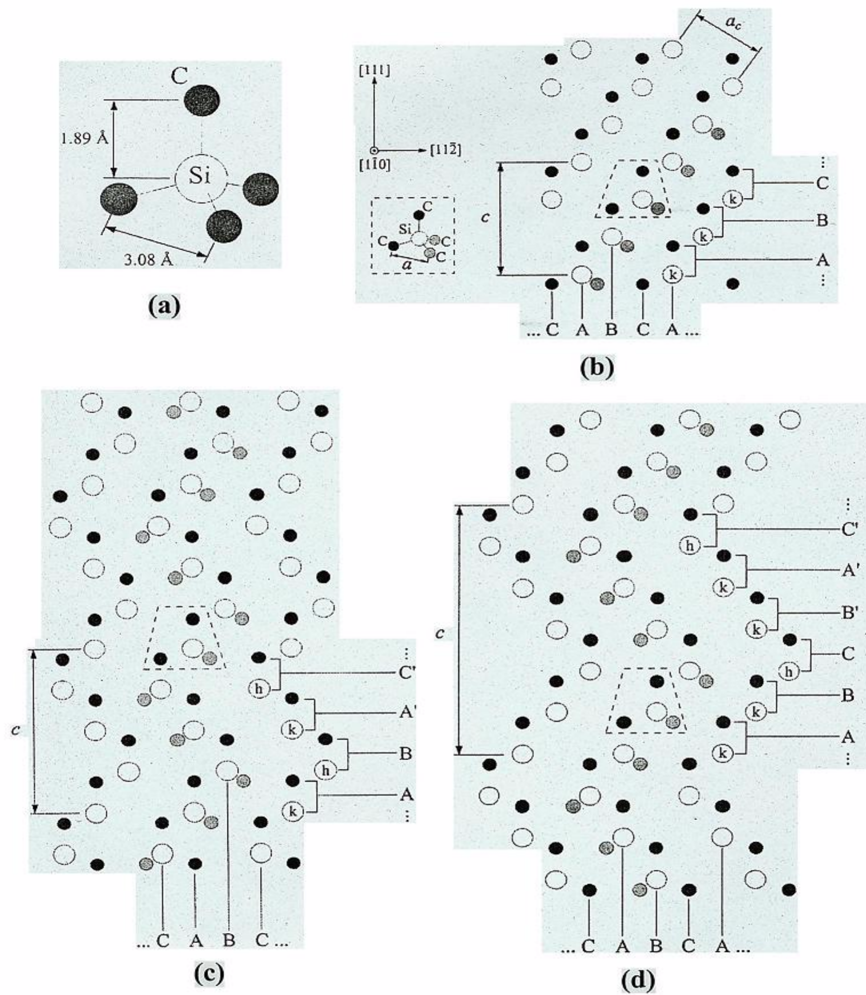

Figure 1.2: (a) basic structural unit of SiC, (b) 3C-SiC stacking sequence, (c) 4H-SiC stacking sequence and (d) 6H-SiC stacking sequence. The Jagodzinski (kkk, khkh, kkhkkh) and ABCA'B'C' notations are also shown [24].

diffusion coefficients below 2000°C for all dopant species. For similar implant and post-implant anneal conditions, activation percentages are lower for Al and B compared to N and P, so that selective p-type doping is more challenging.

Large band gap energy and correspondingly low intrinsic carrier concentration allow SiC to retain its semiconducting characteristics at much higher temperatures compared to Si, since the intrinsic carrier concentration is a pre-factor in the equation governing undesired junction reverse-bias leakage current. As the temperature increases, the intrinsic carrier concentration increases exponentially. The leakage current increases as well, and eventually at high enough temperature, semiconductor device operation is overcome by uncontrolled conductivity as the intrinsic carrier concentration exceeds the intentional device doping [25].

The breakdown field and high thermal conductivity of SiC, coupled with high operational junction temperature, theoretically permit extremely high power density and operating efficiency.

1.2.4 Devices and Applications

FET Structure

All field-effect transistors (FETs), whether MOSFETs, MESFETs or JFETs have similar structure [29]. The gate contact metal and conducting channel form a parallel plate capacitor. The sheet charge density σ_s of the mobile carriers at any point, x, along the channel is controlled by the potential difference between the gate and the channel.

$$\sigma_s = C_i[V_{GS} - V(x) - V_T] \tag{1.1}$$

V_T = threshold voltage, V_{GS} = voltage difference between the gate and the source, $V(x)$ = channel voltage with respect to the source, and C_i = gate capacitance per unit area (ε_i/d_i). The

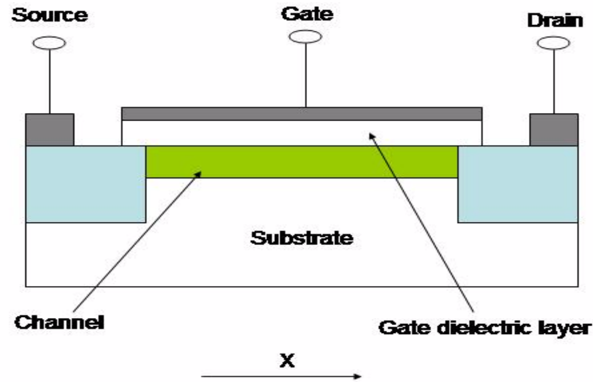

Figure 1.3: Basic FET structure [29]

drain current I_d depends on σ_s and the drain-to-source voltage V_{DS} because $V(x)$ varies with x and tends to reduce σ_s.

The threshold voltage is an important parameter in FETs because it separates the above-threshold regime (or on-state where the charge induced in the device channel is proportional to the gate voltage swing), and the below-threshold regime (or off-state). The potential barrier separating the source and the drain determines the transistors off-current and hence the on-to-off current ratio [29].

MOS techology

The vast majority of semiconductor integrated circuits rely on silicon metal-oxide-semiconductor FETs (MOSFETs). Success with Si-MOSFETs has naturally encouraged the development of

high-performance inversion channel SiC-MOSFETs. The difference in the quality of the thermal oxide grown on Si and SiC has prevented SiC-MOSFETs from realizing their full potential [25].

4H-SiC MOSFET deficiencies can be attributed to differences in Si and SiC thermal oxide quality and an interface structure that causes SiO_2/SiC to exhibit high interface state densities ($> 10^{13} eV^{-1} cm^{-2}$ near the conduction band edge), high fixed oxide charge densities ($\sim 10^{11} - 10^{12} cm^{-2}$), charge trapping, carrier oxide tunneling, and roughness-related scattering of inversion channel carriers. The SiO_2/SiC interface can be much rougher than the SiO_2/Si interface because of the off-angle polishing needed for homoepitaxial growth as well as step-bunching that can occur during annealing to activate implanted dopant species [25].

High-temperature devices

Silicon becomes a conductor at temperatures above about $200°C$ because of a narrow band gap that allows the intrinsic carrier concentration to increase rapidly with temperature. For higher temperature applications, and in high power systems where juction self-heating leads to much higher temperature, Si devices will not be suitable. Hence, transition to SiC is essential for high power/high temperature applications.

Long-term reliability of SiC devices operaing at temperatures between $300 - 600°C$ is a challenge. High temperature gate-insulator reliability is needed for the successful realization of MOSFET-based integrated circuits. Gate-to-channel Schottky diode leakage limits the peak operating temperature of SiC MESFETs to around $400°C$ [25]. Bipolar SiC transistors exhibit poor gain, but improvements in SiC crystal growth and surface passivation could greatly improve SiC BJT performance to make SiC bipolar devices a more viable technology [30]. A common

obstacle to all technologies is reliable long-term operation of contacts, interconnects, passivation and packaging at $T > 300°C$.

Increasingly capable and economical SiC integrated circuits will continue to evolve as SiC crystal growth and device fabrication technology contnue to improve. Currently however, non-ideality in SiC epilayer doping and thickness, surface morphological defects, and slow charge trapping/detrapping phenomena cause unwanted device I-V drift, and limit the yield, size, and manufacturability of SiC high-temperature ICs [31].

High power devices

High power switching devices operate with high electric fields and high current densities, placing great electrical stress on the device. [25]. Current power switching devices are reaching a fundamental limit imposed by silicon's low breakdown field. Silicon carbide has about 10 times the breakdown strength of Si though SiO_2/SiC interface quality is not yet as good as that of SiO_2/Si. Nevertheless, power MOSFETs, IGBTs and various types of MOS-controlled thyristors (MCTs) can all be fabricated on SiC. Because of the higher breakdown field, SiC power devices can have specific-on resistances up to 400 times lower than similar Si devices [32].

$$R_{on} = \frac{4V_B^2}{\mu_n \epsilon_s E_c^3} \tag{1.2}$$

V_B is the breakdown voltage, E_c is the semiconductor critical field, μ_n is the carrier mobility, and ϵ_s is the semiconductor permittivity. For SiC, E_c is about seven times larger compared to Si.

Early on, commercially available SiC epilayers were limited to about $10\mu m$ in thickness with a maximum blocking voltage of about 1600 V. However, with the introduction of thick

layer growth techniques, the epilayer thickness barrier has been removed, and the maximum blocking voltage has increased to > 10 kV for a single device [33, 34].

Micopipes have been a serious problem for SiC device quality and yield, but the desity of micropipes has dropped drastically from hundreds per square centimeter in the early 1990s to ~ 1 per square centimeter in the best material currently available. Apart from micropipes, the density of screw dislocation defects in SiC wafers and epilayers has been measured to be of the order of several thousand per square centimeter. While these defects are not nearly as detrimental to device performance as micropipes, experiments have shown that they can degrade material properties such as breakdown field strength and minority carrier lifetime [25].

For SiC power devices to function successfully, peripheral breakdown owing to edge related electric field crowding must be avoided through careful device design and proper choice of a passivating dielectric material. The peak voltage of most prototype high-voltage SiC devices has been limited by edge related breakdown, especially in SiC devices capable of blocking voltages above a few kilovolts [25].

The high power diode rectifier is a building block of power conditioning circuits. SiC power rectifiers are similar to Si diode device in many ways, except that the current densities, blocking voltages, power densities and switching speeds are typically much higher in SiC. High breakdown field and the wide energy band gap allows SiC Schottky diodes to operate with these improved characteristics [25].

Hybrid Schottky/p-n rectifier structures combine p-n juction reverse blocking capability with low Schottky forward turn-on, and these devices are extremely useful for application-optimized SiC rectifiers [35, 36].

Three terminal power switches (MISFETs, IGBTs and thyristors) that use small drive signals to control large voltages and currents are also critical building blocks of high-power conversion circuits. Silicon carbide solid state switches are similar in structure to Si switches. They are designed to maximize power density via vertical current flow using the substrate as one of the device terminals. Operating current is presently limited by deficiencies in material quality. Nontraditional power switching topologies have also been proposed to reduce the effects of oxide and other material deficiencies while maintaining normally-off insulated gate operation. For example, lateral *and* vertical doped-channel power MOSFETs and JFETs can be completely depleted by built-in potential at zero gate bias [32].

RF and microwave electronics

Based on the electronic and thermal properties, several SiC polytypes should perform better than the semiconductors currently used for high-frequency and microwave electronic devices.

There is interest in SiC devices for applications such as microwave power amplifiers that can be used in phased-array radars, base station transmitters for mobile communications, high-frequency and broad band radar transmitters, and other applications [37]. RF and microwave devices that can be fabricated from SiC include metal-semiconductor field-effect transistors (MESFETs), static induction transistors (SITs), bipolar junction transistors (BJTs), heterojuction bipolar transistors (HBTs) and impact avalanche transit-time (IMPATT) diodes.

Silicon carbide RF devices are used for high-frequency solid state high-power application at frquencies from around 600 MHz (UHF band) to about 10 GHz (X-band). High breakdown voltage and high thermal conductivity coupled with high carrier saturation velocity allow SiC RF transistors to handle much higher power densities than their Si or GaAs counterparts. RF operation at higher drain bias is made possible by the high breakdown field of SiC, and this leads

to high SiC MESFETs output power densities. High thermal conductivity minimizes channel self-heating so that phonon scattering does not seriously degrade channel carrier velocity and current [39].

Silicon carbide is an ideal semiconductor for the fabrication of high power microwave devices operating in the 1 - 10 GHz range [38, 39]. Short channel MESFETs have been operated with an f_t of 22 GHz and an f_{max} of 50 GHz, and static induction transistor (SITs) have reached power levels of 470 W (1.36 W/mm) at 600 MHz and 38 W (1.2 W/mm) at 3 GHz [39].

Optoelectronics and sensors

Wide band gap semiconductor like SiC can be used to realize short-wavelength blue and ultraviolet optoelectronics. 6H-SiC blue p-n juction light emitting diodes (LEDs) were the first commercially available SiC devices, and they were the first mass produced LEDs to cover the blue wavelength range (250 - 280 nm). They were not efficient diodes (efficiency $< 1\%$) since SiC is an indirect band gap material (i.e., the positions of the conduction band minimum and valence band maximum do not coincide in crystal momentum space), in which case, transistion from the valence band maximum to conduction band minimum is phonon assisted. Despite their inefficiency, they were commercially successful from 1989 to 1995 [25]. SiC blue LEDs have now been replace by the brighter and more efficient direct band gap GaN LEDs.

SiC has proved to be much more efficient at absorbing short-wavelength light, which allows the fabrication of UV-sensitive photodiodes that serve as excellent flame sensors for turbine-engine combustion monitoring and control. 6H-SiC has been used to fabricate diodes with low dark current, as well as sensors that are not sensitive to the near infrared wavelengths that are produced by heat and solar radiation [25].

The high temperature capabilities of SiC allow the fabrication of catalytic metal-SiC and metal-insulator-SiC (MIS) prototype gas sensors that show great promise as combustion engine emission monitors [40, 41]. These structures enable rapid detection of changes in hydrogen and hydrocarbon content to sensitivities of parts per million. The sensors are small enough to be place anywhere in an engine. When fully developed, these sensors could assist in active combustion control to reduce harmful pollution emissions from automobile and aircraft engines. [42].

CHAPTER 2

METAL-SEMICONDUCTOR CONTACTS AND DIFFUSION BARRIERS

2.1 Metal-Semiconductor Contacts

2.1.1 General Information

The metal-semiconductor (MS) contact is a crucial part of all solid-state devices. An ideal MS contact can either be rectifying (Schottky) or non-rectifying (ohmic). High quality ohmic contacts are necessary to connect semiconductor devices to external circuit, and stable Schottky contacts are essential for switching or provide rectification, either as a stand alone device or as part of more complex circuits [43].

An ideal MS contact should, on an atomic scale, be an intimate contact between metal and semiconductor with no layer of any type between them. There should be no interdiffusion between them and no adsorbed impurities or surface charges at the MS interface. However, in practical contacts, ideal conditions are seldom achieved and MS devices operate below theoretical predictions. Non-idealities in modern-day structures primarily affect the barrier height characterizing the contact [44]. Controlling the surface parameters that affect the Schottky barrier height guides the development of ohmic and rectifying contacts in semiconducting systems [45].

Ideally, it should be possible to predict the behavior of a metal on a semiconductor if the work function of both are known. But contact performance, as related to surface properties in SiC for example, is poorly understood, and most of the metal-SiC behavior cannot be predicted [45].

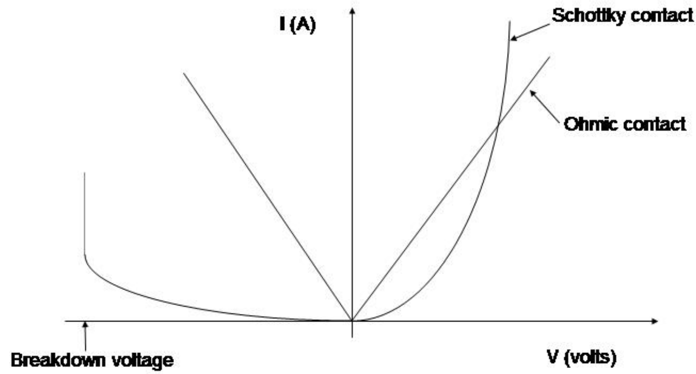

Figure 2.1: I-V Characteristics of ohmic and schottky contact

Schottky contacts are characterized by asymmetric current-voltage (I-V) curve as shown in figure 2.1, similar to a p-n junction. An ohmic contact may be considered a limiting case of Schottky contact in which Schottky characteristics have been converted to ohmic characteristics after certain processing steps. However, some MS contacts may be ohmic as prepared if the barrier height at the MS interface is low enough. In these cases, asymmetric I-V characteristics does not occur [46].

Schottky-Mott and Bardeen limit for barrier height

The Schottky model for ideal, intimate MS contacts is based on energy level diagrams [45] as illustrated in figure 2.2. ϕ_M is the metal work function. The semiconductor work function is $\phi_S = \chi + (E_c - E_F)|_{FB}$ where FB means "flat band" conditions - i.e. no band bending at the MS interface. The electron affinity of the semiconductor at the semiconductor surface is $\chi = (E_o - E_c)|_{surface}$. The energy difference between the conduction energy (E_c)

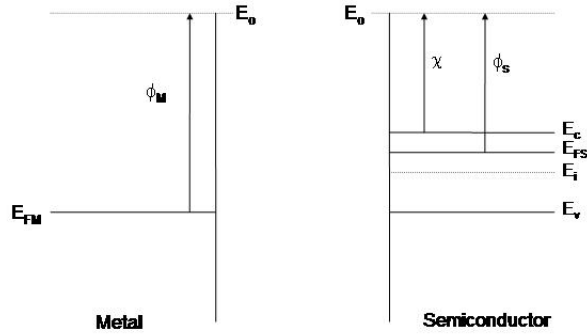

Figure 2.2: Energy level diagram of metal and semiconductor

	n-type semiconductor	p-type semiconductor
$\phi_m > \Phi_s$	Rectifying	Ohmic
$\phi_m < \Phi_s$	Ohmic	Rectifying

Table 2.1: Ideal MS contanct dependence on work functions

and the Fermi energy level at flat band is the other term added to electron affinity to obtain the semiconductor work function expression. The semiconductor can be n-type or p-type depending on the dopant. The energy level diagrams of metal-semiconductor combination (n-type and p-type) are shown in figure 2.3 with different metal and semiconductor work functions.

The barrier to reverse current flow which is not affected by the applied potential is defined as the barrier height for the metal-semiconductor pair [43]. It may also be defined as the energy difference between the Fermi level in the metal and the bottom of the conduction band in the semiconductor at the interface [45].

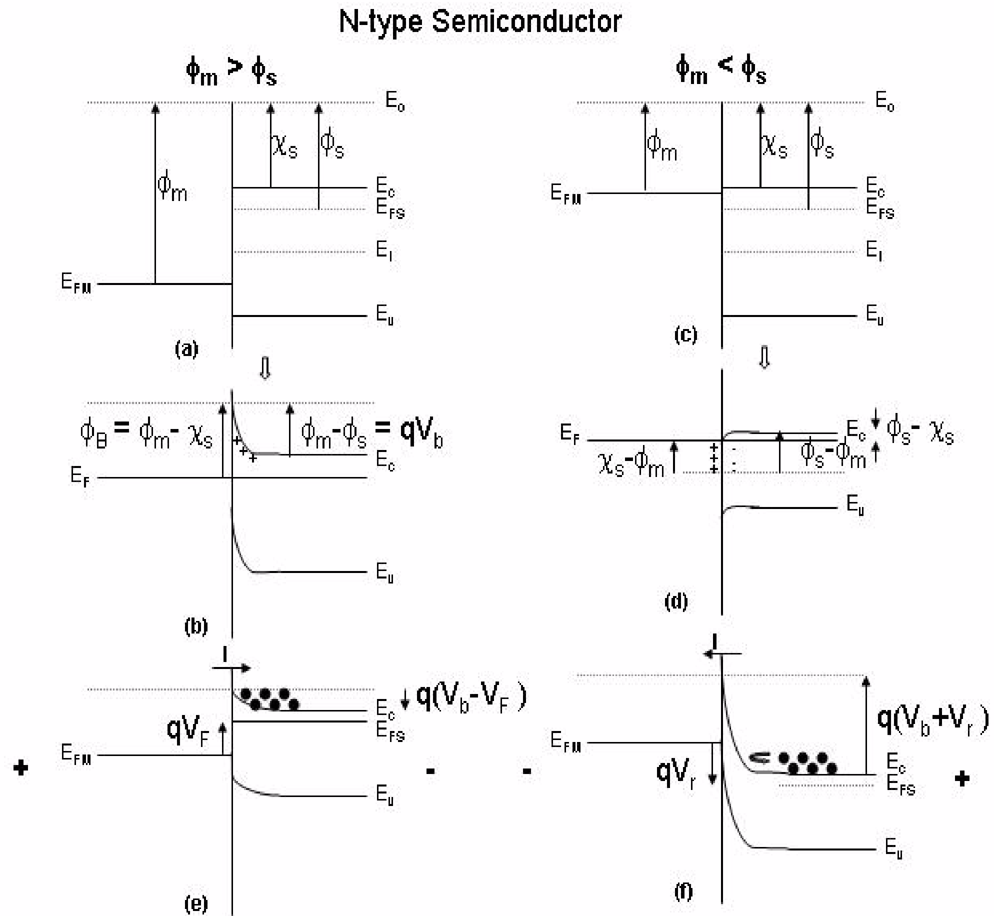

Figure 2.3: Energy level diagram for metal-semiconductor (n-type) contact. For $\phi_m > \phi_s$: (a) just in contact, (b) in equilibrium with built-in potential V_b, (e) forward biased with V_F, (f) reverse biased with V_r. For $\phi_m < \phi_s$: (c) just in contact and (d) at equilibrium [43, 44]

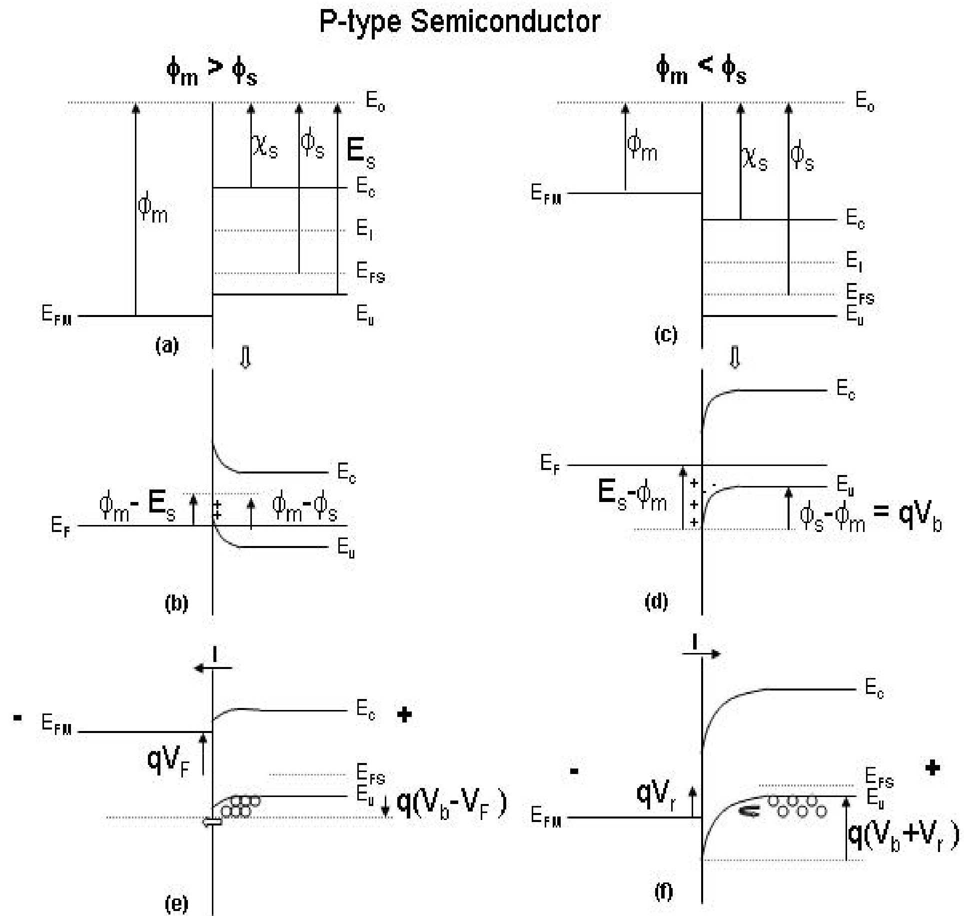

Figure 2.4: Energy level diagram for metal-semiconductor (p-type) contact. For $\phi_m > \phi_s$: (a) just in contact and (b) in equilibrium. For $\phi_m < \phi_s$: (c) just in contact, (d) at equilibrium with built-in potential V_b, (e) forward biased with V_F, (f) reverse biased with V_r. [43, 44]

For the ideal MS contact illustrated in figures 2.3 and 2.4, we have chosen the flat band condition and assumed no electric field exists within the semiconductor. This implies that the semiconductor terminates at the surface without distortion of the electron energy levels and that no surface states exist. For the case of an n-type semiconductor in which the metal work function is greater than semiconductor work function, ($\phi_m > \phi_s$), and taking vacuum level to be the same in the metal and semiconductor, electrons flow from the semiconductor to the metal, leaving positive donor ions, and accumulating at the surface of the metal. The resulting dipole electric field opposes further electron flow, and in equilibrium, the Fremi levels in the metal and semiconductor are equal,

$E_{FM} = E_{FS}$. If the semiconductor is uniformly doped, the charge density is uniform in the depletion layer and the electric field $\mathcal{E}$ is linear with distance. The barrier energy of the Schottky barrier contact is $\phi_B = \phi_m - \chi_s$. This descrption is referred to as the Schottky limit, and ϕ_B is directly proportional to ϕ_m. ϕ_B is the barrier energy that electrons going from metal to semiconductor encounter, while electrons going from semiconductor to metal encounter built-in potential energy qV_b determined by the band bending in the semiconductor at equilibrium. The fact that V_b is bias dependent and ϕ_B is not is the reason for the asymmetric I-V characteristics of Schottky diodes.

The Schottky model predicts that it is possible to obtain a rectifying contact or an ohmic contact by simply choosing a metal with the appropriate work function. This is not always true however, especially for diodes fabricated on III-V semiconductors. Recent evidence for SiC suggests that SiC approximates Schottky behavior [45].

MS contacts are never ideal, and Bardeen [47] proposed that if surface states exist at the MS interface in sufficient number, ϕ_B would be independent on ϕ_m. Surface states are electronic states (e.g., dangling bonds) localized at the semiconductor surface due to the termination of

bulk periodicity. Consider a neutral semiconductor surface, with say a neutral energy level ϕ_o measured relative to the valence band. If the states are filled to an energy greater than ϕ_o, the surface possesses a net negative charge, and the states are acceptor-like in behavior. If the states are filled to a level below ϕ_o, the surface has a net positive charge, and the states behave in a donor-like manner [45].

Assume a very thin ($\sim$ 1nm) insulating layer separates the metal and semiconductor, such that electrons can flow though it with little or no restriction. This layer still support a potential difference, and if the number of surface state is large, the Fermi level at the surface of the semiconductor will be ϕ_o. The energy difference $\phi_m - \phi_o$ for the Schottky model will appear entirely across the thin interfacial layer, since the charges in surface states will fully accomodate the necessary potential difference. Thus, these states contribute some of the electrons and positive space charge needed to bring the structure to equilibrium. The height and width of the barrier shrink substantially [48]. Hence, ϕ_B is independent of ϕ_m, and $E_{FM} = E_{FS}$ at the surface of the semiconductor. The barrier height for Bardeen contact is $\phi_B = E_g - \phi_o$. The Fermi level is "pinned" by the surface states at ϕ_o above the valence band. This is known as Bardeen limit. The Fermi level is found experimentally to be "pinned" at $\phi_o \approx \frac{1}{3}E_g$ which impies the barrier height ϕ_B should be typically close to $\frac{2}{3}E_g$. Most common semiconductors (Si, Ge, GaAs, GaP) have enough surface states to pin the Fermi level at about $\frac{1}{3}E_g$. Surface states are often seen as a pronounced peak in the density of states plot at an energy $E_v + \frac{1}{3}E_g$ [48].

In practice, the value of the barrier height ϕ_B will be somewhere between the Schottky and Bardeen limits [45]. A general relationship that combines both the surface states and workfuntion was first given by Cowley and Sze [49] as

$$\phi_{BO} = \gamma(\phi_m - \chi_s) + (1 - \gamma)(E_g - \phi_o) \tag{2.1}$$

Figure 2.5: Non ideal energy level diagram under forward bias V_F [45]

For a case where no electric field inside the semiconductor (i.e., the flat band condition)

$$\gamma = \frac{\varepsilon_i}{\varepsilon_i + qD_s\delta} \tag{2.2}$$

where ε_i is the permittivity of the interfacial layer, δ is the thickness. D_s is the surface state density per unit energy per unit area.

$qD_s\delta \ll \varepsilon_i \quad \Rightarrow \quad \gamma \approx 1$ Schottky limit

$qD_s\delta \gg \varepsilon_i \quad \Rightarrow \quad \gamma \ll 1$ Bardeen limit

A typical diagram for a non-ideal MS interface under forward bias V_F is shown in figure 2.5. An insulating layer of thickness δ exist between the metal and semiconductor and the interface states are filled to ϕ_o.

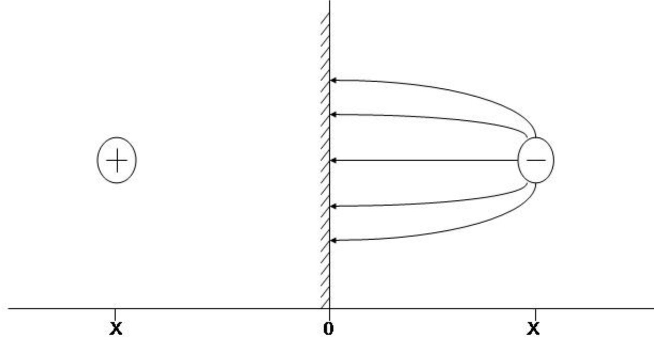

Figure 2.6: Image force.

Image Force Lowering

The practical barrier energy in a Schottky diode is slightly smaller than expected. One likely reason is attributed to image force lowering which occurs when an electron outside the metal induces virtual positive image charge in the metal because of the requirement that the electric field be perpendicular to the interface. The coulomb attractive force on the electron towards the metal surface due to its virtual positive charge is

$$F_i = -q\mathcal{E} = -\frac{q^2}{4\pi\epsilon_s(2x)^2} = -\frac{q^2}{16\pi\epsilon_s x^2} \tag{2.3}$$

The electrostatic energy associated with this image force is determined by the work the image force does as the electron moves from point x to ∞

$$E_i = \int F_i(x)\,dx = -\frac{q^2}{16\pi\epsilon_s x} \tag{2.4}$$

ϵ_s is the high frequency permittivity of the semiconductor rather than static permittivity because the thermal velocity of the electron as it approaches the surface is quite high ($\sim 10^5 ms^{-1}$) [50], and the semiconductor might not be fully polarized in the short time the electric field is produced. The image potential energy has to be added to the potential energy due to the Schottky barrier as shown in figure 2.7.

$$\begin{aligned} E &= E_i + E_s = -qV_i(x) - qV_b(x) \\ E(x) &= -\frac{q^2}{16\pi\epsilon_s x} - qV_b(x) \end{aligned} \tag{2.5}$$

Since the image potential is only important near the surface, and the Schottky barrier field is constant near the surface, the maximum potential energy occurs at a position x_m where the resultant electric field vanishes - that is, where the image force field is equal and opposite to the depletion region field.

$$\mathcal{E}_{max} = \frac{q}{16\pi\epsilon_s x_m^2} \qquad \Rightarrow \qquad x_m = \sqrt{\frac{q}{16\pi\epsilon_s \mathcal{E}_{max}}} \tag{2.6}$$

The amount of barrier lowering can be determined by finding the extremum,

$\frac{dE(x)}{dx} = 0 \qquad at \qquad x = x_m$

$$\begin{aligned} \Delta\phi_{bi} &= x_m\mathcal{E}_{max} + \left(\frac{q}{16\pi\epsilon_s\mathcal{E}_{max}}\right)^{1/2} = 2x_m\mathcal{E}_{max} \\ \Delta\phi_{bi} &= 2\mathcal{E}_{max}\left(\frac{q}{16\pi\epsilon_s\mathcal{E}_{max}}\right)^{1/2} = 2\left(\frac{q\mathcal{E}_{max}}{16\pi\epsilon_s}\right)^{1/2} \end{aligned} \tag{2.7}$$

The effect of the image force is to lower the barrier that the electron has to overcome in passing from the metal into the semiconductor by the amount $\Delta\,\phi_{bi}$. For this contribution to the barrier energy to be present, there must be electrons in the conduction band near the top

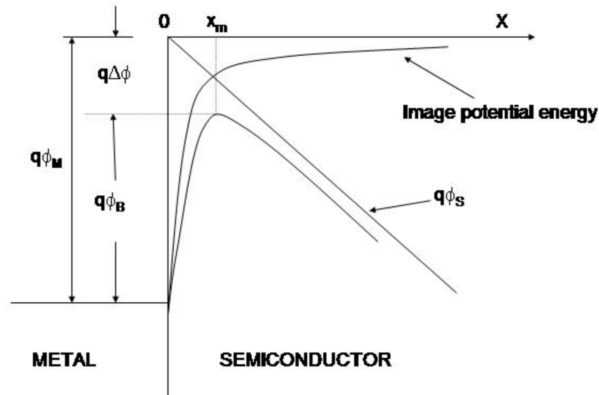

Figure 2.7: Effect of image force lowering on the barrier height.

of the barrier. This requirement does not affect other contributions to ϕ_B from work function difference, surface state charge, etc. [48, 50].

Holes can be attracted to the metal by image force as well. Hole energy is measured downward from the top of the valence band, so that the effect of the image force is to bend the valence band upward near the metal surface.

2.1.2 Metal-SiC Contacts

Ohmic contacts to SiC

An ohmic contact to a semiconductor is usually produced by heavily doping the surface region of the semiconductor immediately under the contact. It is known that, to first order, the equilibrium barrier height is not affected by an increase in semiconductor doping, but that the depletion width decreases with increased doping. Reducing the depletion width increases the

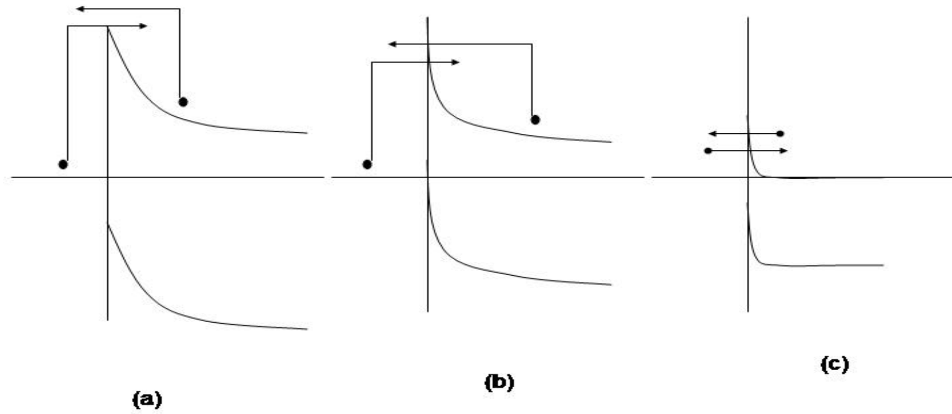

Figure 2.8: Effect of doping concentration on the barrier width. (a) low (b) moderate and (c) high doping [44].

carrier tunneling probability, and contact resistance is generally observed to drop with increased doping as depicted in figure 2.8.

When the semiconductor doping exceeds $\sim 10^{18} cm^{-3}$ (moderate doping regime), significant tunneling can take place through the thin upper portion of the barrier. For doping exceeding $\sim 10^{19} cm^{-3}$ (high doping regime), the entire barrier becomes so narrow that low energy majority carriers can tunnel the barrier; that is, the barrier becomes effectively transparent to carrier flow [44]. The specific contact resistance r_c is the parameter that characterizes ohmic contact. This parameter depends on the doping concentration of the semiconductor, the characteristics of the semiconductor surface (e.g., epilayer or implant/activation) and the high temperature anneal conditions for forming the ohmic contact.

n-type α-SiC

Ohmic contacts on n-type α-SiC (4H and 6H) have been studied over the last two decades. The quality of SiC, both bulk and epitaxial, has improved steadily over the same period. The availability of heavily doped n-type material has improved also because of better understanding of doping processes - both implant/activation and doping during epitaxial growth. Specific contact resistance of the order of $10^{-6}\Omega\, cm^2$ are common for doping concentration of about $10^{19} cm^{-3}$. Much of the contact work was previously done for 6H-SiC, but recently the focus has shifted to 4H-SiC because of its superior mobility characteristics [46].

Metal silicide formation has been the most dominant mechanism for ohmic contact formation, on either 4H- or 6H-SiC polytypes. Results have shown that the specific contact resistance increases with increasing barrier height, but decreases as the doping concentration increases. For heavily doped materials, the specific contact resistance was predicted to increase dramatically. Nickel silicide ohmic contact formed during the high temperature ($\sim 900°C$) annealing of nickel deposited on SiC is the most widely used contact on n-type SiC [51, 52, 4, 53, 54]. Reported specific contact resistance vary from between 1×10^{-6} and $1 \times 10^{-2}\Omega\, cm^2$. With proper processing, nickel makes a relatively good ohmic contact on moderately doped ($\sim 10^{18} cm^{-3}$) SiC [46].

The first ohmic contact fabricated on 6H-SiC was deposited nickel which was subsequently annealed at high temperatures by Palmour, *et al* [55]. Nickel ohmic contacts on 6H-SiC have been characterized electrically and physically by Crofton *et al* [5]. Specific contact resistances $< 5\times 10^{-6}\Omega\, cm^2$ were measured following 2 minute anneals of the samples in vacuum at $950°C$. Nickel layers were deposited on epilayers with doping concentrations between $7-9\times 10^{18} cm^{-3}$. Rutherford backscattering spectroscopy and Auger electron spectroscopy have shown that the

high temperature anneal leads to the reaction of Ni with SiC forming nickel silicide. Nickel silicide formation has also been observed by Liu, *et al* [6]. During the formation of nickel silicide, carbon is set free at the interface and migrates towards the surface of silicide layer. Apart from the formation of nickel silicide, other mechanisms such as vacancy formation might also contribute to forming the ohmic contact. As-sputtered nickel silicide on SiC epilayers does not form an ohmic contact. Ohmic contacts result only from the reaction of Ni and SiC at high temperature. Liu, *et al* [6] included chromium in the contact layer, for example Ni/W/Cr, in order to improve contact stability while retaining the low specific contact resistance of pure nickel. It was suggested that chromium reacts with the carbon liberated by the reaction of nickel with SiC. Stable Cr_3C_2 and Ni_2Si compounds are the product of this coupled reaction. The choice of metal for the formation of a silicide contact to n-type SiC is not limited to Ni. Metals such as Co, Hf, and Ta can also form silicides on SiC with physical and electrical properties similar to nickel silicide contact [46]. Binary alloys and multilayer contacts have also been investigated as possible ohmic contact to n-type SiC. Table 2.2 shows a list of ohmic contacts for n-type α-SiC and some typical values of the specific contact resistance.

TiN reported by Glass, *et al* [56, 57] and TiW reported by Crofton, *et al* [54] are among the special cases of ohmic contact where x-ray photoelectron spectroscopy (XPS) has shown that a thin insulating layer (0.5 - 1.5nm) of silicon nitride at the MS interface formed a metal-insulator-semiconductor (MIS) structure and promoted ohmic behavior. TiN has a low work function which is favorable for an ohmic contact on n-type material. Ohmic behavior was not observed without the formation of a thin Si-N layer [58].

Metallization	SiC carrier conc.(cm^{-3})	Annealing condition	$r_c(\Omega\, cm^2)$	Method of r_c measurement	Ref.
Ni	4.5×10^{17}	1000°C, 20s	1.7×10^{-4}	TLM	[53]
Ni	4.7×10^{18}	950°C, 5mins	mid 10^{-2}	4-pt. probe	[54]
Ni	7.9×10^{18}	950°C, 2mins	$< 5 \times 10^{-6}$	TLM	[5]
Ni	9.8×10^{17}	1050°C, 5mins	$10^{-3} - 10^{-4}$	TLM	[58]
Ni	4.5×10^{20}	1000°C, 5mins	1×10^{-6}	Cont. area	[4]
Ni	3.2×10^{17} and 1.4×10^{18}	1000-1200°C 1min	1.3×10^{-5}– 3.6×10^{-6}	TLM	[87]
Ni	2×10^{18}– 2×10^{19}	950-1000°C	4×10^{-4}– $\sim 10^{-6}$	TLM	[88]
Mo	2×10^{18}– 2×10^{19}	950-1000°C	4×10^{-4}– $\sim 10^{-5}$	TLM	[88]
Ni-Cr (60-40 Wt%)	4.7×10^{18}	950°C, 5min	1.8×10^{-3}–	circular TLM	[54]
Ti	2×10^{18}– 1×10^{20}	as-deposited	1×10^{-2}– $< 2 \times 10^{-5}$	circular TLM	[89]
W	3×10^{18}– 1×10^{19}	1200-1600°C	5×10^{-3}– 1×10^{-4}	4-pt probe	[90]
TiW	4.7×10^{18}	600°C, 5min	7.8×10^{-4}	circular TLM	[54]
Mo	$> 1 \times 10^{19}$	as-deposited	$\sim 1 \times 10^{-4}$	4-pt probe TLM	[92]
Ta	$> 1 \times 10^{19}$	as-deposited	$\sim 1 \times 10^{-4}$	4-pt probe TLM	[92]
Ni, Ni/W Ni/Ti/W	$10^{17} - 10^{18}$	1000-1050°C 5-10min	$10^{-3} - 10^{-6}$	TLM	[93]
Cr/W Cr/Mo/W	$10^{17} - 10^{18}$	1000-1050°C 5-10min	$10^{-2} - 10^{-4}$	TLM	[93]
TiC	4×10^{19}	etched at 1300°C for 15mins in H_2	1.3×10^{-5}	TLM	[94]

Table 2.2: Some ohmic contacts on n-type α-SiC. The layers in multi-layered contacts are seperated with slashes, layers at the surface to the interface with SiC proceed from right to left

p-type α-SiC

It is more difficult to form ohmic contacts to p-type SiC by simply reducing the Schottky barrier height because of the large bandgap and large work function of SiC. Aluminum (pure and alloy) is convetionally used to create ohmic contacts on p-type material [58]. The low melting point and rapid oxidation characteristics of aluminum makes processing the contact difficult. The melting point can be increased by using aluminum alloys, and the most widely used alloys are Al-Ti of different compositions. The thermodynamic driving force for aluminum oxidation is very high, and this places restrictions on using aluminum-based contacts [7, 60]. Another difficulty is the fact that aluminum is very volatile at moderate annealing temperature. Work reported by Crofton, *et al* [9] have shown that 90/10 wt% Al/Ti alloy layer annealed at $1000°C$ can loose aluminum to the annealing environment, thus increasing the metal sheet resistance significantly. Using aluminum-based alloys can place strict requirements to processing and passivating contacts.

As shown in table 2.3, the earliest reported ohmic contacts to p-type SiC contain either aluminum or boron [59] and were annealed at very high temperatures $\sim 1700°C$. An enhanced p-type concentration at the SiC surface, probably due to recrystallization from solution rather than aluminum diffusion into the SiC, was observed.

Ohmic contact on p-type SiC are now achieved primarily by reducing the depletion width via high doping concentration rather than by reduction of the Schottky barrier height. Tunneling current dominates the electron transport for highly doped SiC, and the resulting specific contact resistance varies according to the relation [61, 62]

$$r_c \propto \exp\left(\frac{\phi_B}{\sqrt{N}}\right) \tag{2.8}$$

Metallization	SiC carrier conc.(cm^{-3})	Annealing condition	$r_c(\Omega\, cm^2)$	Method of r_c measurement	Ref.
Al	1.8×10^{18}	700°C, 10min	1.7×10^{-3}	TLM	[54]
Al	8×10^{18}	800°C, 10min	$10^{-2} - 10^{-3}$	TLM	[58]
Al-Si	NR	1700°C	NR	-	[59]
Al-Si	NR	900-1000°C	NR	-	[95]
Al-Ti	5×10^{15}- 2×10^{19}	1000°C, 5min	2.9×10^{-2}- 1.5×10^{-5}	Circular TLM	[96]
Si-B	NR	1700-2000°C	NR	-	[59]
Ta	$> 1 \times 10^{19}$	as-deposited	7×10^{-4}	TLM 4-pt probe	[92]
Ti	$> 1 \times 10^{19}$	as-deposited	3×10^{-4}	TLM 4-pt probe	[92]
Mo	$> 1 \times 10^{19}$	as-deposited	2×10^{-4}	TLM 4-pt probe	[92]
Al/Ti	Al implant dose: 1×10^{15}	500°C, 20min (1650°C, 30min)	5.6×10^{-4}	4-pt probe	[97]
Al/Ti/Ai	9×10^{20}	600-800°C	$1 - 2 \times 10^{-4}$	TLM	[98]
W	NR	1900°C	NR	-	[59]
Al/W/Au-W/W	NR	1900°C, 120s	$2 - 5 \times 10^{-4}$	4-pt probe	[90]

Table 2.3: Some ohmic contacts on p-type α-SiC. The layers in multi-layered contacts are seperated with slashes, layers at the surface to the interface with SiC proceed from right to left

r_c is the specific contact resistance, ϕ_B is the schottky barrier height, N is the carrier concentration.

It may be possible to reduce or elliminate the need for annealing contacts to either n-type or p-type SiC if the surface can be doped heavily enough. As deposited Mo, Ta, and Ti contacts on p+ SiC epitaxial layers grown by chemical vapor deposition (CVD) have been reported to yield ohmic contacts [63]. Specific contact resistances measured by Kuphal's 4-point method were of the order of $10^{-4}\Omega\, cm^2$, though the method does not account for nonuniform current densities.

To reduce the Schottky barrier height on a p-type material, metals with high work function must be used, though empirical evidence shows that the Schottky barrier height has a weak dependence on metal work function because of partial pinning of the Fermi level. Platinum (high work function (5.65eV), high melting point and high resistance to oxidation) has displayed ohmic behavior both as deposited and after contact anneals at $850°C$ [58].

Work on Al-Ti contacts [9] including surface studies of etched Al-Ti contact layers have shown many pits of significant size and density at the contact surface, suggesting that aluminum diffusion may not actually be doping SiC surface, but may instead have resulted in enhanced field emission because of the creation of many hemispherical intrusions into the SiC surface similar to those observed by Braslau [10] for Au-Ge contacts on GaAs.

Specific contact resistance as low as $4 \times 10^{-6}\Omega\, cm^2$ have been reported for a p-doping concentration of $2 \times 10^{19} cm^{-3}$ in 6H-SiC [64] for non aluminum-base contact. Double layers (160nm of silicon on 50nm of cobalt) were annealed at $500°C$ for 5 hours followed by $900°C$ for 2 hours. Cobalt silicide was formed, and the absence of graphite was observed at the interface by RBS. The authors used silicon to prevent the formation of a carbon rich phase, since residual carbon has been reported as the cause of high contact resistance.

n-type β-SiC

Nickel contacts annealed between $900 - 1250°C$ are commonly used for β-SiC [65, 66, 67, 68]. Au-Ta, Cr, $TaSi_2$ and Al are some of the metals that have been used for ohmic contact to n-type β-SiC [66].

Steckl and Su [67] have used as-deposited and annealed nickel for rectifying and ohmic contact, respectively, on the same device. Daimon, *et al* [65] reported that annealed nickel and as-deposited aluminum formed ohmic contacts on n-type β-SiC (100) with low carrier concentrations ($5 \times 10^{16} - 1 \times 10^{17} cm^{-3}$). High specific contact resistance for both contacts were attributed to the low doping concentrations.

Table 2.4 shows a number of ohmic contact metallization schemes. Most of the contacts were annealed at temperatures above 800$°C$. There is no simple formular for creating ohmic contact on β-SiC. Ohmic contact formation may be due to silicide formation, as in the case of Ni, or both silicide and carbide formation (Cr, Ta, W, Ti, Mo), or neither silicide nor carbide as for Au and Ag [69]. Many of the studies reported the specific contact resistance as shown in table 2.4.

Multilevel metallization schemes were investigated by Shor, *et al* [70] based on Ti and W for high temperature (650 - 750$°C$) applications. Electronic and optoelectronic extended operation at high temperature need such a multilevel metallization scheme. Multilevel contact metallization addresses concerns like reactivity, oxidation and diffusivity within the metallization and with the SiC itself. The most promising metallization scheme reported was Au/Pt/TiN/Ti, which remained ohmic for 31 hours at 650$°C$ and then became rectifying. TiN layer was believed to act as a diffusion barrier.

Metallization	SiC carrier conc.(cm^{-3})	Annealing condition	$r_c(\Omega\, cm^2)$	Method of r_c measurement	Ref.
Al	5×10^{16}	as-dep	1.6×10^{-1}	3-cont.	[66]
Ni	5×10^{16}	$1250°C$, 5 min	1.4×10^{-1}	3-cont.	[66]
Cr	5×10^{16}	$1250°C$, 5 min	7.0×10^{-2}	3-cont.	[66]
Ti	$10^{17} - 10^{18}$	$300°C$, 30-90 min	$7.6 - 9.2 \times 10^{-3}$	4-point	[99]
W	$10^{17} - 10^{18}$	as-dep - $600°C$, 10min	1.5×10^{-2}	4-point	[99]
Ta	5×10^{19}	as-dep - $1000°C$, 1hr	$7 \times 10^{-7}-$ 4.3×10^{-6}	circular TLM	[100]
Re	5×10^{19}	as-dep - $900°C$, 30min	$1 \times 10^{-4}-$ 1×10^{-5}	circular TLM	[100]
Pt	5×10^{19}	as-dep - $500°C$, 30min	$6 \times 10^{-6}-$ 1×10^{-5}	circular TLM	[100]
Au/Pt/Ti	$10^{16} - 10^{17}$	650°C, 1hr	1.1×10^{-4}	4-pt probe	[70]
Au/Pt/W	$10^{16} - 10^{17}$	650°C, 8hr	2×10^{-4}	4-pt probe	[70]
Au/Pt/-TiN/Ti	$10^{16} - 10^{17}$	650°C, 31hr	1.4×10^{-4}	4-pt probe	[70]
Pt/TiW/Ti	$10^{16} - 10^{17}$	650°C, 3hr	2.6×10^{-4}	4-pt probe	[70]
$TaSi_2$	5×10^{16}	$850°C$, 5 min	2×10^{-2}	3-cont.	[66]
$TiSi_2$	$10^{17} - 10^{18}$	$1000°C$, 10s + $450°C$, 390min	1.1×10^{-4}	4-point	[99]
WSi_2	$10^{17} - 10^{18}$	$1000°C$, 10s + $450°C$, 390min	3.9×10^{-4}	4-point	[99]

Table 2.4: Some ohmic contacts on n-type β-SiC. The layers in multi-layered contacts are seperated with slashes, layers at the surface to the interface with SiC proceed from right to left

Metallization	SiC carrier conc.(cm^{-3})	Annealing condition	$r_c(\Omega\, cm^2)$	Method of r_c measurement	Ref.
Al	1×10^{16}	$880°C$, 3min	3.1×10^{-2}	3-cont.	[66]
Ni	$10^{17} - 10^{18}$	as-dep - $700°C$, 15min	4.1×10^{-2}- 2.8×10^{-2}	3-cont.	[68]
Au-Ta-Al (91:2:7 at%)	1×10^{16}	$1200°C$, 30min	4.7×10^{-1}	3-cont.	[66]
$TaSi_2$/Al	1×10^{16}	$1200°C$, 30min	2.0×10^{-1}	3-cont.	[66]

Table 2.5: Some ohmic contacts on p-type β-SiC. The layers in multi-layered contacts are seperated with slashes, layers at the surface to the interface with SiC proceed from right to left

p-type β-SiC

There are few reported studies on ohmic contacts to p-type β-SiC. Some of the contacts in literature are listed in table 2.5. Specific contact resistances reported for aluminum contact or aluminum alloy contact are high [58]. The high annealing temperature does not seem to help the contact characteristics significantly, probably because of the high driving force for aluminum oxidation, causing aluminum to diffuse away from the interface and react with oxygen.

Variable and sometimes conflicting results for contacts on β-SiC may be attributed to [58] (1) differences in crystal quality of β-SiC layer due to defect densities that are much higher than in α-SiC polytypes and (2) differences in the state of the surface prior to metal deposition.

Schottkty contacts to SiC

Schottky contact on both n- and p-type SiC are reported in the literature for different contact metals. The first Schottky contact on 6H-SiC were made by fusing small pellets of Si-Al and Si-B alloys to single crystal SiC at $1700°C$ and $> 2000°C$, respectively [59]. These diodes showed sharp breakdown at voltages $\sim 50V$ and high reverse current prior to breakdown. A

forward current of 0.5A at 4.5V is typical of these diodes [43]. After this pioneering work, a lot of 6H-schottky barrier diodes have been fabricated. Mead and Spitzer [71] and Mead [72] had early reports of barrier height studies on 6H-SiC Schottky contacts. Al and Au were used as metal contacts on n-type SiC. They found that Schottky barrier height, determined by capacitance-voltage technique, was almost independent of the work function of the metals used for the contact. Hagen [73] drew similar conclusion for Au, Ag and Al contact on both p- and n-type samples of cleaved and etched 6H- and 15R- polytypes.

Schottky diodes on β-SiC were first reported by Yoshida *et al* [74] on epitaxially grown n-type layers with Au metal contact. Barrier heights in the range of 1.11 - 1.15eV were determined by C-V and photoelectron techniques. Waldrop and Grant [75] investigated the effect of the choice of metal on 3C-SiC Schottky barrier characteristics. Metals such as Pd, Au Co, Ti, Ag, Tb, and Al were considered, but only Pd, Au and Co formed schottky contacts. The interface chemistry and the Schottky barrier height were studied using x-ray photoelectron spectroscopy (XPS), I-V and C-V techniques.

Shenoy, *et al* [76] have also reported Pt-Schottky barrier diodes on n^-/n^+ 3C-SiC grown on n^+-Si substrates. The diodes had low specific-on resistance ($6.1 \times 10^{-4}\Omega\, cm^2$) and a breakdown voltage of about 85V for a $0.4\mu m$ thick drift layer. Schottky barrier heights of about 0.85V with an ideality factor of 1.25 were obtained.

High-voltage Schottky barrier diodes on 4H-SiC were first reported by Itoh *et al* [77, 78]. The contact metals used include Au, Ni and Ti. I-V and C-V techniques were used for barrier height determination. They reported barrier height dependence on work function because surface ”pinning” of the Fermi level did not occur. The room temperature breakdown voltage was around 800V, and a current density of $100A\, cm^{-2}$ was obtained for forward bias of 1.67V.

The breakdown voltage of Ti/4H-SiC diodes increased to 1100V when a highly resistive layer is formed at the periphery of the contact, serving as edge termination [79]. The edge termination was formed by boron ion implantation followed by high temperature heat treatment to remove damage to the lattice sustained during implantation.

Raghunathan *et al* [80] have reported high breakdown voltage (1000V) for Ti/4H-SiC. Weitzel *et al* [81] reported 1400V breakdown on 4H-SiC with an on-resistance of $1.5m\Omega\, cm^2$. Saxena and Steckl [82, 83] have also reported Ni and Pt Schottky contacts on 4H-SiC. Barrier heights extracted from common techniques (C-V, I-V, XPS) have generally indicated Fermi level ”pinning”.

All nickel contacts (ohmic and schottky) on 6H-SiC have been reported by several authors [84, 85, 86, 83], and breakdown voltages exceeding 1000V at 25 and 300$^\circ C$ have been observed. Most of the diodes used an oxide for surface passivation and device isolation.

2.2 Diffusion and Oxidation Barriers

2.2.1 Diffusion in Solids

Fick’s laws are the ealiest mathematical basis for macroscopic diffusion. For an inhomogenous single phase binary alloy with diffusion coefficient (D_1) of component 1, the concentration gradient in steady state is defined by Fick’s first law as

$$J_1 = -D_1 \left(\frac{\partial C_1}{\partial x} \right)_t + C_1\, v = -\Delta_t\, C_1 + C_1 v \tag{2.9}$$

where J_1 is the flux of atoms of component 1 at a given time, C_1 is the concentration and v is the velocity of mass moving because of the application of forces such as electromigration,

thermal or chemical potential gradient [118]. An inhomogenous specimen becomes homogenous if annealed long enough, and the net flow of matter will cease.

The diffusion coefficient is called the self-diffusion coefficient if no external forces and chemical gradient are involved. For diffusion under a chemical gradient, where the diffusion is affected by the motion of all atomic species, the diffusion process is called inter-diffusion with a chemical diffusion coefficient.

Under non-steady state conditions where the concentration is changing with time, Fick's second law states that the rate of change of concentration is equal to the gradient of the flux

$$\frac{\partial C}{\partial t} = -\Delta\,\vec{J} = D\Delta^2 C \tag{2.10}$$

It is generally assumed that D is not a function of position. Fick's second law is the basis for most of the diffusion measurements and calculations in solids. It can be applied for different kinds of sample geometry [118].

Solving a diffusion equation with all the possible driving forces included can be a challenging mathematical problem. The simplest mathematical treatment assumes the absence of chemical driving forces, which is strictly valid only if thermodynamic equlibrium is established between two samples with different diffusion coefficients. Chemical driving forces may be absent if the components of the diffusion couple are identical and hence have identical diffusion properties, or if the two components of the diffusion couple are chemically different but co-exist in thermodynamic equilibrium. For example, a metal can be in equilibrium with its oxide [119]. The solution to Fick's second law depends largely also on sample geometry. Several geometry specific solutions are described below.

Thin film on bulk sample

Consider an infinitesimally thin layer of areal density M with thickness less than the diffusion distance $(Dt)^{1/2}$ such that it can be represented by a Dirac delta function δ. Assuming no surface flux or flux through imperfections, the boundary conditions in one-dimension are

$C(x,0) = M\,\delta(x)$ and $\frac{\partial C(0,t)}{\partial x} = 0$

The solution to Fick's second law is

$$C(x,t) = \frac{M}{2\sqrt{\pi D t}} \exp\left(-\frac{x^2}{4Dt}\right) \tag{2.11}$$

M is the total amount of diffusant per unit area, t is the diffusion time and C is the concentration at position x and time t. This geometry is widely used in radioactive tracer work compatible with a delta function type of diffusant distribution and infinitesimally small mass thickness.

Most thin film work on bulk layers is conducted with an initial thickness of the source of diffusant (h) that is greater than the diffusion distance $(Dt)^{1/2}$ when the following boundary conditions are satisfied

$C(x,0) = C_o$ if $h \geq x \geq 0$, $C(x,0) = 0$ for $x > h$

and for $t > 0$, $\frac{\partial C(0,t)}{\partial x} = 0$,

the solution is given by

$$C(x,t) = \frac{C_o}{2}\left[erf\left(\frac{x+h}{2\sqrt{Dt}}\right) - erf\left(\frac{x-h}{2\sqrt{Dt}}\right)\right] \tag{2.12}$$

Diffusion couple with constant surface composition

For a diffusion couple with two samples having uniform initial concentrations of C_o and C_1, the initial boundary conditions at $t = 0$ can be witten as

$C(x,0) = C_1$ for $x < 0$ and $C(x,0) = C_o$ for $x > 0$. The solution to the diffusion equation is then

$$\frac{C(x,t) - C_o}{C_1 - C_o} = \frac{1}{2}\left[erfc\left(\frac{x}{2\sqrt{Dt}}\right)\right]. \tag{2.13}$$

In the diffusion couple solution, if the difference between C_1 and C_o is large such that $x \gg 2\sqrt{Dt}$ the diffusion coefficient will vary with composition along x. To determine the diffusion coefficient at known composition, Boltzmann-Matano analysis is used [118].

Diffusion in structurally inhomogenous sample

Thin film diffusion samples are almost never structurally homogenous. That is, defects like dislocations and grain boundaries are always present. Diffusion occurs in the lattice through equilibrium point defects such as vacancies, interstitial atoms, divacancies, etc, but engineering materials are mostly polycrystalline in nature, and they contain non-equilibrium defects such as dislocations, stacking faults and grain boundaries. Diffusion along these defects is greater than in monocrystalline samples. The diffusive process in thin films may be largely controlled by grain boundary diffusion, especially at low temperature ($\sim 100°C$) [118].

In polycrystalline materials, there is simultaneous diffusion within the grain and along the grain boundaries, and these two diffusion mechanism are coupled. The ease with which lattice atoms go into the grain boundary or vice-versa will determine the diffusion kinetic regime that prevails in the whole sample. According to Harrison [120], three types of kinetic regime labelled A, B, and C are possible.

A-Kinetics: Extensive lattice diffusion that causes the diffusion fields from adjoining grains to overlap.

B-Kinetics: Each boundary is assumed to be isolated and the flux at large distance from a grain boundary approaches zero.

C-Kinetics: Lattice diffusion is considered negligible, and significant atomic transport occurs only within the boundaries.

Grain boundary diffusion measurements in bulk materials invariably involve B-kinetics. Little evidence has been obtained from profiling experiments on bulk materials that clearly support the existence of A- or C-kinetics. In this respect, thin films are both unique and challenging as candidates for diffusion studies because the very high density of structural defects makes it possible to observe any of the three kinetic regimes given the appropriate annealing condition [121, 122].

Diffusion in amorphous materials

Diffusion in amorphous solids is a common phenomenon. According to the Stokes-Einstein equation [123], the frictional force impeding the motion of particle i of radius r_i is given by the viscosity of the liquid in which it moves. Einstein's diffusion coefficient is, $D = K_B T/\zeta$ where ζ is the friction coefficient. The Einstein equation becomes the Stokes-Einstein coefficient given by $D_i = K_B T/A\pi r_i$. The general feeling is that this equation has broad validity despite the fact that it was derived for a macroscopic sphere moving steadily through a viscous fluid. However, there is nothing in the equation to adjust for the existence of measurable diffusion in glassy solids or metallic systems, where the viscosity may depend on time in some way.

Diffusion in solids can be studied via experimental, statistical and atomic mechanism [124]. One of the reasons for the poor understanding of mass transport in amorphous solids is the lack of a consistent approach to the problem. First, proper knowledge of the experimental characteristics

of diffusion is needed. The next thing is to propose an atomic mechanism and then build its proper statistical mechanisms in order to compare the experimental data to the macroscopic consequences of the atomic behavior.

Experimental diffusion coefficients are frequently expressed in terms of a pre-exponent D_o and the activation energy E_A,

$$D = D_o \exp\left(-\frac{E_A}{kT}\right). \tag{2.14}$$

The temperature range over which this equation is valid is quite narrow, two to three orders of magnitude for the diffusion coefficient at most [125, 126, 127]. Determining D_o precisely can also be difficult. Inconsistencies between various authors for the same alloy point to measurement error and cast doubt on the stated values of D_o and E_A.

2.2.2 Thermodynamics of Diffusion

Metallizations in microelectronics are composed of many layers of dis-similar materials, and the knowledge of the stability of the interfaces between different materials is important. The total Gibbs free energy of the system (the two materials in contact and the interface between them) can be decreased by different processes including enrichment of the components at the interface with respect to one or both of the components or via chemical reaction of the components followed by the formation of additional phases [129]. The change in Gibbs free energy of the system can be used as a criteria for possible reaction products that form at the interface. The Gibbs free energy is defined from the combination of the first and second laws of thermodynamics. In a closed system the Gibss free energy is given by the relation

$$G \equiv U + pV - TS = H - TS \tag{2.15}$$

where U, V, H, and S are the internal energy, volume, enthalpy and entropy of the system, respectively. In an open system however, the Gibbs free energy also depends on the number of moles of each of the components, and the differential form of the free energy equation becomes

$$d\,G(T, P, n_i) = -S d\,T + V d\,p + \sum_i \gamma_i\, dn_i \tag{2.16}$$

where γ_i is the chemical potential of component i. The equilibrium state of the system can be investigated with the Gibbs free energy function.

There are three stable equilibrium states: (i) complete, (ii) partial and (iii) local thermodynamic equilibrium [130]. A system in complete equilibrium has its Gibbs free energy function minimum, $d\,G = 0$. Systems in equilibrium with respect to only certain components are said to be in partial equilibrium. For local equilibrium, equilibrium exists only at the interfaces between different phases present in the system. In thin films systems, complete equilibrium is seldom achieved, and the concept of local equilibrium is therefore important. Local equilibrium is treated using chemical potential.

In the treatment of multicomponent open systems, the most common process considered in defining the thermodynamic functions for a solution is called the mixing process. The mixing process is the change in state experienced by the system when appropriate amounts of components in their reference states are mixed together forming a homogenous solution brought to the same temperature and pressure as the initial state [131]. The molar Gibbs free energy of mixing or formation can be expressed as

$$\Delta G_m = \Delta H_m - T \Delta S_m \tag{2.17}$$

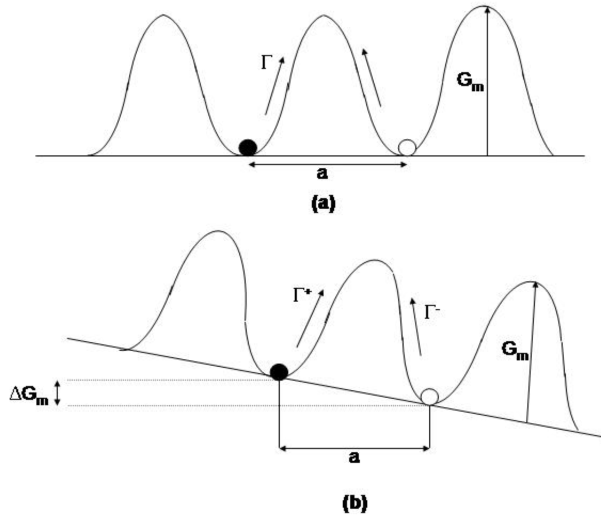

Figure 2.9: Atomic energy barrier as a function of atomic position [118].

The mixing process is strongly influenced by forces between atoms and molecules (ΔH_m). The fundametal cause of mixing, however, is entropy (ΔS_m).

Diffusion in solids involve atomic exchange with some kind of lattice imperfection, and it is usually thermally activated. We will consider some thermodynamic factors involved in determining the diffusion coefficients in chemically inhomogenous samples.

The energy barrier seen by atoms as a function of atomic position is depicted in figure 2.9. Each atom sees the same energy barrier in the absence of a driving force, the probability of a forward or backward jump is the same, and there is no net velocity in any direction. Atoms make a jump if given enough free energy G_m to go over the barrier and occupy an equivalent equilibrium position by an exchange with defect state. The probability (W) that an atom will acquire an energy G_m is given by [118]

$$W = \nu_o \exp\left(-\frac{G_m}{kT}\right) \tag{2.18}$$

ν_o is the atomic vibration frequency.

However, a successful jump is subject to the availability of a defect state in the adjoining position.

The average probability of finding a defect is

$$N_d = Z \exp\left(-\frac{G_f}{kT}\right) \tag{2.19}$$

where G_f is the free energy needed to form the defect and Z is the coordination factor.

The frequency of successful jumps can be written as

$$\Gamma = W\,N_d = Z\nu_o \exp\left[-\frac{(G_m + G_f)}{kT}\right] \tag{2.20}$$

In 3-D, the difussion coefficient can be expressed as

$$D = \frac{a^2}{6} f\Gamma \tag{2.21}$$

where a is the nearest neighbor atomic distance and f is a correction factor (f $\leq$ 1) for non-random jump.

Hence,

$$W = \frac{1}{6}a^2 f Z\nu_o \exp\left[\frac{(S_f + S_m)}{k}\right] \exp - \left[\frac{(H_f + H_m)}{kT}\right] \tag{2.22}$$

ΔH_f and ΔH_m are the enthalpies of formation and motion of defects, respectively, and S_f and S_m are the corresponding entropies. The temperature dependence of the diffusion coefficient is normally written as

$$D = D_o \exp\left(-\frac{Q}{kT}\right) \tag{2.23}$$

with

$D_o = \frac{1}{6}a^2 f Z \nu_o \exp\left[\frac{(S_f + S_m)}{k}\right]$ and $Q = H_f + H_m$.

The diffusion of atoms in a solid can occur via the movement of interstitial atoms in the lattice. Lattice atoms can be displaced into the interstitial sites (self-interstitial), and the vacancy left behind is annihilated at an interface, surface or by another interstitial atom. Self-interstitial diffusion is of high probability at high temperature because higher initiation energy is available. When an interstitial atom is formed and vacancy is left behind, the defect is called a Frenkel defect. Frenkel defects dominate in radiation damaged solids. Frenkel defects are very mobile and contribute to mass transport. Interstitial atoms may also be foreign or impurity atoms which are generally of small size, for example, H, C, O and N. Because of their sizes, they move into the interstitial sites easily, and their formation emergies (S_f and H_f) are negligible compared with the motion energy. Hence, the diffusion of foreign or impurity interstitials may be very fast.

Diffusion kinetics change dramatically in the presence of non-equilibrium vacancies and interstitial atoms. Deviation from stoichiometry in intermetallic componds can yield non-equilibrium vacancies. In non-stoichiometric alloys, the size of the species that is larger in concentration may dictate whether the diffusion will be enhanced.

Finite driving force on atoms

For non-zero driving force on an individual atom (linear chemical diffusion regime), a net flux of atoms in a particular direction is observed. A finite mass velocity term is included in Fick's first law. Free energies between adjoining sites are not the same, and the change in free energy between adjacent sites can be written as $\Delta G_m = aF$.

The number of forward and backward jumps are not the same, and the net number of jumps can be written as

$$\Gamma^{+} - \Gamma^{-} = \Gamma(e^{-\varepsilon} - e^{+\varepsilon}) \tag{2.24}$$

where $\varepsilon = \frac{1}{2}\frac{\Delta G_m}{kT}$

$$\frac{\Gamma^{+} - \Gamma^{-}}{2\Gamma} = \sinh\left(\frac{aF}{kT}\right) \tag{2.25}$$

Possible driving forces in thin film metallizations include [118]:

Electromigration $\rightarrow\ Ze\mathcal{E}$, where Ze is the effective charge, and $\mathcal{E}$ is the electric field

Thermomigration $\rightarrow \left(\frac{Q^*}{T}\right)\frac{\partial T}{\partial x}$ where Q^* is the heat of transport.

Chemical inhomogeniety $\left(\frac{\partial \mu}{\partial x}\right) \rightarrow -kT\left(\frac{\partial \ln \gamma}{\partial x}\right)$ where γ is the activity coefficient.

Stress field $\rightarrow \left(\frac{\partial U}{\partial x}\right)$ where U is the interaction energy.

Chemical composition variations give rise to chemical potential gradients in non-ideal solid reactions. The atomic force over N lattice planes due to a chemical potential grdient can be written as

$F = \frac{kT}{aN}(\ln C_2\gamma_2 - \ln C_1\gamma_1)$ for a binary solution with components 1 and 2. γ_1 and γ_2 are the activity coefficients for non-ideal solution, C_1 and C_2 are the concentration terms. Generally if

$10 < \frac{C_2\gamma_2}{C_1\gamma_1} < 1000$ over 10 atomic planes, $\left(\frac{aF}{kT}\right) = \frac{\Gamma^{+} - \Gamma^{-}}{\Gamma} \ll 1$

This is refered to as the linear regime and

$C_1 v = C_1 \Gamma a^2 F/kT$ *or* $v = \frac{D_1 F}{kT} = B_1 F$, the Nernst-Einstein relation

where B_1 is the mobility.

Fick's first law without a concentration gradient becomes $J_1 = B_1 F C_1$.

2.2.3 Diffusion Barriers

Introduction

It is known that reliable contact and metallization schemes for microelectronics require thin film diffusion barriers. Though atomic diffusion in the solid phase is a relatively slow process, the distances (film thicknesses) are small, and diffusion can be significant, even at room temperatures in some cases. The idea of a diffusion barrier came to prominence because Al-based metallizations that are commonly used in VLSI technology for contacts and interconnects are highly reactive with Si. Aluminum must be kept away from Si where such reactions could be detrimental to device performance. Electromigration problems with the Al-based interconnects forced researchers look for alternative metals and copper with lower electrical resistivity and higher resistance to electromigration, became a candidate [132, 133, 134, 135]. However, Cu is very mobile in metals and semiconductors even at quite modest temperatures. Copper creates deep traps in Si, resulting in serious degradation of the device performance and reliability [136, 137, 138]. Therefore the need for a very effective diffusion barrier layer became paramount.

The initiative of diffusion barrier effort for VLSI technology has been extended to contact metallizations for harsh environment and high power devices fabricated with wide band gap materials (SiC, GaN, etc.). Effective barriers will prevent rapid deterioration of the contact properties and device performance as the result of oxidation and inter-mixing driven by high temperature operation. Reliable long-term operation in harsh environment is the primary goal of this work.

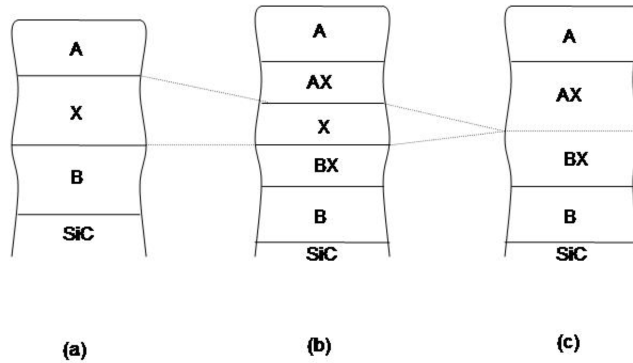

Figure 2.10: Diffusion barrier in multi-layer structure [140]

Definitions

A diffuion barrier material (X) physically separates material (A) from material (B) as shown in figure 2.10. Material B may be an ohmic or Schottky contact or the semiconductor, while material A is suitable for connection with an external circuit.

An ideal diffusion barrier should meet the following conditions [139]

- The transport of A across X and of B across X should be small
- The loss rate of X into A and into B should be small
- X should be stable thermodynamically against A and B
- There should be strong adhesion of X with A and with B
- The specific contact resistance of A on X and B on X should be small
- X should be laterally uniform in thickness and structure

- X should be resistant to mechanical and thermal stresses
- X should be highly conductive (thermally and electrically)

Most of the materials used as diffusion barrier may not be able to satisfy all the conditions listed, and compromises usually have to be made.

Diffusion barriers can be loosely classified in three groups:

(a) sacrificial barriers (b) stuffed barriers and (c) amorphous barriers.

When two materials, A and B are separated by diffusion barrier X, layer X only slows down the eventual mixing of A and B, and the ultimate state of equilibrium is not eliminated by X. The question then is, how long can X serve its purpose of separating A and B? [139]

(a) Sacrificial barrier

The length of time that a sacrificial barrier will be useful can be estimated. This means that the point of possible failure is foreseeable. A typical sacrificial barrier is illustrated in figure 2.10. It is essential to fully characterize the compound formed betwween X - A and X - B, and to know the reaction rates and the activation energies. Predicting the time it will take for X to be totally consumed at a given temperature allows the pre-determination of how much of X is needed for a given temperature-time cycle to prevent its total consumption. If X is totally consumed, it is assumed that the metallization will fail catastrophically.

The advantage of the sacrificial barrier is its adaptability. Many binary metal combinations form compounds, so that the choice of material is wide, even taking into consideration other constraints which are important for the proper functioning of the barrier. However, compounds X-A and X-B formed in the process must be compatible with the constraints - e.g., for electrical contacts, X-A and X-B must be good conductors, maintaining good thermal and mechanical properties and resistant to corrosion and/or oxidation. The diffusion of A and B in X must be

negligible compared with the growth of X-A and X-B.

(b) Stuffed barriers

Grain boundaries and other structural defects in the diffusion barrier material could serve as rapid diffusion paths when there is no thermodynamic driving force for X to react with A and B as in the case of sacrificial barriers. It is essential to be able to stop the diffusion of A and B along the grain boundaries and structural defects. One way to do this is to eliminate the diffusion paths by plugging the paths with suitable impurity atoms or molecules (e.g., carbon or N_2), and this process is called ”stuffing” the barrier. There are evidence to suggest that stuffing the barrier can indeed be effective. The interpretation of this evidence in terms of atomistic mechanisms is largely conjecture, but the resulting effect can be striking [139]

Reactive sputtering is one of the ways of stuffing barriers. Sputtering Mo for example, in an Ar/N_2 gas mixture can produce a nearly stoichiometric Mo_2N layer which works well as stuffed barrier [139, 140]. Electrically conductive nitrides (TiN, Mo_2N), borides (TiB_2) and carbides (TiC, NbC) used as diffusion barriers have had varying success. Stuffing the barriers generally makes it less conducting.

(c) Amorphous barriers

Apart from plugging the diffusion paths with light atoms and molecules, the diffusion path could be removed by eliminating the grain boundaries altogether by making the diffusion barrier either single crystalline or amorphous. It is difficult to practically make single crystalline barriers, and many researchers work with amorphous barriers. However, amorphous barrier are metastable, i.e., they are transformed to polycrystalline films at some elevated temperature and the consequences are the problems associated with polycrystalline barriers. It is also possible that the amorphous layer X can react with A and/or B, in which case amorphous barrier becomes sacrificial barrier.

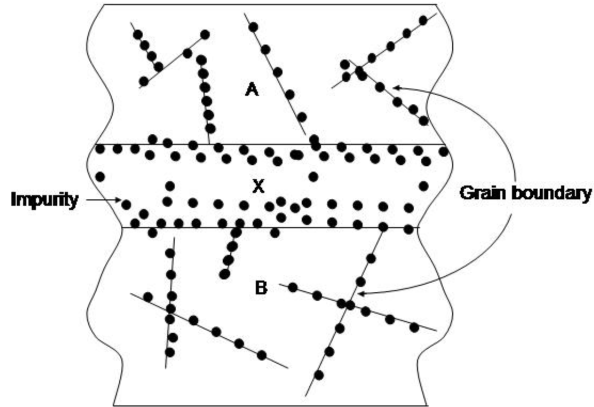

Figure 2.11: Stuffed diffusion barrier [140]

Pure elemental metals do not form an amorphous phase at room temperature, so amorphous metallic alloys are often used as diffusion barriers. There are a number of empirical rules on how to select the elements to obtain amorphous metallic alloys. Generally, the larger the differences between the constituents in terms of atomic size, crystalline structure and electronegativity, the easier it is for the constituents to form metallic alloys. The two parameters used to characterize metallic alloys are the crytallization temperature (T_c) and the reaction temperature (T_r) of the constituents.

Amorphous ternary interstitial alloys of the form MSiN (M = V, Nb, Ta, Cr, Mo, W) have been investigate as diffusion barriers for Cu [141]. Amorphous binary transition metal nitrides of some transition metals have been reported [142, 143, 144, 145]. For tungsten, titanium and tantalum nitrides, researchers have observed that adding silicon stabilizes their amorphous structure. Generally, adding metalloids like (B, C, Si, P, N) to binary amorphous structures has the potential of stabilizing them. The number of ternary amorphous conducting alloys that can be

conceived in the way is very large. Beside the combination of Si_xN_z with transition metals listed above, P_xN_z and B_xN_z have also received attention as possible candidates.

Diffusion barrier literature

In the literature, many materials have been tried as diffusion barriers - from single metal to binary and ternary materials, silicides, nitrides, and carbides barriers. The binary compounds are known for their excellent stability while the tenary systems are primarily amorphous and better at slowing the diffusion process [129]. Many of the composite layers studied involve at least the Si/barrier/Cu structure, with additional layers are sometimes included for adhesion purposes.

Elemental metallic barriers - Pure metals with high melting points have been used as diffusion barriers on electrical contacts because of the conductivity requirement. But pure metals are polycrystalline, and grain boundaries and other defects serve as paths for rapid diffusion, even when the solubility of the materials in the contact is extremely low. Table 2.6 shows examples of single element diffusion barriers. Polycrystalline films can be more effective barrier if they are stuffed; however, a compromise between the amount of stuffing and other barrier properties such as conductivity and adhesion has to be reached.

Binary compound and amorphous materials - In seitching from elemental to compound films, the number of possible materials for the barrier layer increases enormously. However, relatively few binary compound and amorphous barriers have been studied experimentally. The stability of Ti/Pt/Au metallization structure was improved by replacing titanium with tungsten because tungsten has very low solubility in gold and does not react with it. However, to promote adhesion and improve corrosion resistance, titanium was added to the tungsten at levels above the solid solubility requirement [146], and a more effective diffusion barrier was thereby created. Table

sample structure	annealing ambient	barrier effect. (hr/°C)	failure mode	Ref.
SiC/Ni/Au	Vacuum	990/300	Au reaction with Ni	[107]
GaN/Ti/Al/Mo/Au	NR	360/500	NR	[101]
Al_2O_3/Ti/Mo/Au	NR	/$<$ 800	Au diff. throu Mo gb	[102]
Si/Ti/Cu	vacuum	0.5/973	reaction at $500°C$	[103]
Si/Ta/Cu	vacuum	0.5/600	$TaSi_2$ and Cu_3Si	[104]
Si/Ta/Cu	N_2:H_2 = 9:1	0.5/300	reaction at $400°C$	[104]
Si/W/Cu	vacuum	NR	Cu diff throu W gb	[105]
Si/Cr/Cu	vacuum	NR	Cu diff to Si	[105]
Si/W/Ta/Cu	vacuum	0.5/450	NR	[105]

Table 2.6: Elemental diffusion barrier layer for semiconducting devices

2.7 showed examples of binary compounds and binary alloys used as diffusion barriers.

Ternary amorphous barrier - Some attention is currently being given to amorphous ternary alloys as candidates for barrier layer in microelectronics. Binary amorphous alloys of refractory metal silicides films sputtered in argon and nitrogen gas mixtures to form a M-Si-N ternary system, have shown good properties and examples of such systems in litrature are listed in table 2.8.

Conducting oxide diffusion barriers - Oxidation of contacts operating at elevated temperatures is one problem that leads to rapid contact degradation. Even common diffusion barrier materials like TiN and W are sensitive to oxidation [147]. Using thermodynamically stable conducting oxides as diffusion barrier at elevated temperatures in air is one option for generating a good diffusion barrier.

Ruthenium dioxide (RuO_2) is the most thermodynamically stable oxide of ruthenium when formed at temperatures greater than $200°C$. Ruthenium dioxide is almost as conducting as ruthenium metal, and has better conductivity than some silicides that are used as diffusion barriers in integrated circuits [$\rho_{Ru} = 6.7 \times 10^{-6}\Omega - cm,\ \ \rho_{RuO_2} = 4.6 \times 10^{-5}\Omega - cm$] [147].

sample structure	annealing ambient	barrier effect. (hr/°C)	failure mode	Ref.
SiC/NiCr/Au	Vacuum	2500/300	NR	[107]
SiC/Ti/$TaSi_2$/Pt	air	200/600	diff. and oxid.	[108]
Si/TaC/Cu	vacuum	/775	diff. and react. of Cu	[109]
Si/Ta_2N/Cu	vacuum	/650	react. of Cu	[109]
Si/TiN/Cu	vacuum	0.5/600	react. form Cu-Si	[106]
Si/HfN/Cu	vacuum	0.25/500	struct. (SEM)	[115]
Si/HfN/Pd	vacuum	0.25/500	struct.(SEM)	[115]
Si/HfN/Au	vacuum	0.25/500	struct.(SEM)	[115]
Si/a-$W_{72}Si_{18}$/Cu	vacuum	1/700	crystall. at 800°C	[105]
Si/ZrN/Al	vacuum	0.5/600	diffusion	[116]
Si/ZrB_2/Al	vacuum	2/625	diffusion	[117]
Si/a-$Ni_{60}Nb_{40}$/Cu	vacuum	1/600	NR	[105]
Si/a-$W_{76}N_{24}$/Cu	vacuum	0.5/750	reaction	[110]
Si/Ta-N/Cu	vacuum	0.5/750	reaction	[111]
Si/Ta-Si/Cu/Ta	$Ar - N_2$	/550	crystal. and react.	[136]

Table 2.7: Binary compound or alloy diffusion barrier layer for semiconducting devices

sample structure	annealing ambient	barrier effect. (hr/°C)	failure mode	Ref.
Si/SiO_2/W-Si-N/Cu	Vacuum	1/650	crystall.	[112]
Si/SiO_2/Mo-Si-N/Cu	Vacuum	0.5/850	crystall.	[112]
Si/Ta-Si-N/Cu	Vacuum	0.5/900, 10^3/350	crystall.	[112]
Si/a-$TiPN_2$/Cu	vacuum	0.5/600	struct. and elect.	[105]
Si/$TiSi_2$/a-$TiPN_2$/Cu	vacuum	0.5/700	struct. and elect.	[106]
Si/a-Ti-Si-N/Cu	vacuum	0.5/900	TiN grain growth	[113]
GaAs/a-Si-Ti-W/Au	vacuum	944/300	electrical	[114]

Table 2.8: Tenary compound or alloy diffusion barrier layer for semiconducting devices

There are ternary conducting oxides which may be more difficult to prepare, for example, $Bi_2Ru_2O_7$, $SrVO_3$, etc. and oxides with an unstable conducting phase such as $2CrO_2(conducting) \rightarrow Cr_2O_3(non-conducting) + \frac{1}{2}O_2$. Most of the conducting oxides have not been studied with the idea of using them as diffusion barriers, and there is much potential in this area. For example, conducting oxides such as zinc oxide (ZnO) [148], indium tin oxide (ITO) [149], rhodium oxide (RhO_2) [150] and so on, could turn out to be good diffusion barriers.

CHAPTER 3

ANALYTICAL TECHNIQUES

3.1 Electrical Analysis

3.1.1 Sheet Resistance Measurement

The four-point probe technique is the most common technique for thin film sheet resistivity measurements. Parasitic resistances such as the contact resistance (R_c) and spreading resistance (R_{sp}) makes the result of two-point probe measurements difficult to interpret [151]. These resistances are negligible in the four-point probe configurations because the potential differences are measured with zero or very small currents flowing through the potential probes. There are different probe configurations that can be adopted for four-point measurements, including collinear four-point probe and van der Pauw probe arrangements.

Collinear four-point probe

For four probes on a straight line in contact with a semiconductor and with probe separation distance d, the resistivity of an arbitrarily shaped finite sample is given by [151],

$$\rho = 2\pi d F(V/I) \tag{3.1}$$

F is a correction factor that depends on sample geometry and is a product of several independent correction factors,

$$F = \frac{(\ln 2)F_1 F_2 F_3}{\pi} \tag{3.2}$$

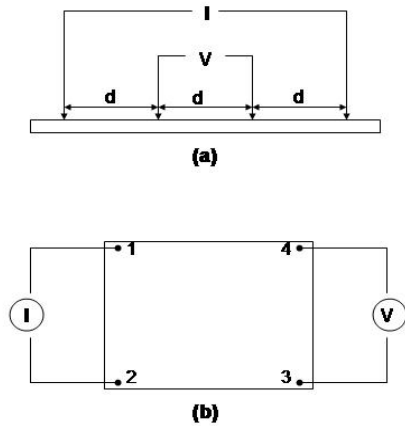

Figure 3.1: (a) Collinear four-point probe measurements (b) van der Pauw four-point probe measurements

F_1, F_2, F_3 are correction factors for sample thickness, lateral sample dimension and probe placement relative to to the sample edges.

For very thin samples, $F_2 = F_3 = 1$ [151], and

$$\rho = \frac{\pi t}{\ln 2}(\frac{V}{I}) = 4.532t(\frac{V}{I}) \tag{3.3}$$

The sheet resistivity ρ_s in Ω/sq is ρ/t or

$$\rho_s = 4.532 \left(\frac{V}{I}\right) \tag{3.4}$$

van der Pauw four-point probe

The theoretical basis for sheet resistivity measurements on irregularly shaped sample was developed by van der Pauw using conformal mapping [152, 153, 154]. Flat, arbitrarily shaped sample must meet the following conditions:

- the contacts are at the circumference of the sample
- the contacts are sufficiently small
- the sample is uniformly thick
- the surface of the sample is singly connected, that is, the sample does not contain any isolated hole.

Under these conditions, the sample resistivity is given by

$$\rho = \frac{\pi t}{\ln 2} \frac{(R_{12,34} + R_{23,41})}{2} F \tag{3.5}$$

where $R_{12,34} = V_{34}/I_{12}$, F is a correction factor satisfying the relation

$$\frac{R_r - 1}{R_r + 1} = \frac{F}{\ln 2} cosh^{-1} \left(\frac{\exp{(\ln 2/F)}}{2} \right). \tag{3.6}$$

For a symmetric and uniform sample, $R_r = R_{12,34}/R_{23,41} = 1$ and $F = 1$. A plot of the corection factor F against R_r is shown in figure 3.2. The sheet resistance for a source current of 4.532mA can be written as

$$\rho_s = 4.532 \frac{(R_{12,34} + R_{23,41})}{2} F = \frac{(V_{34} + V_{41})}{2} F \tag{3.7}$$

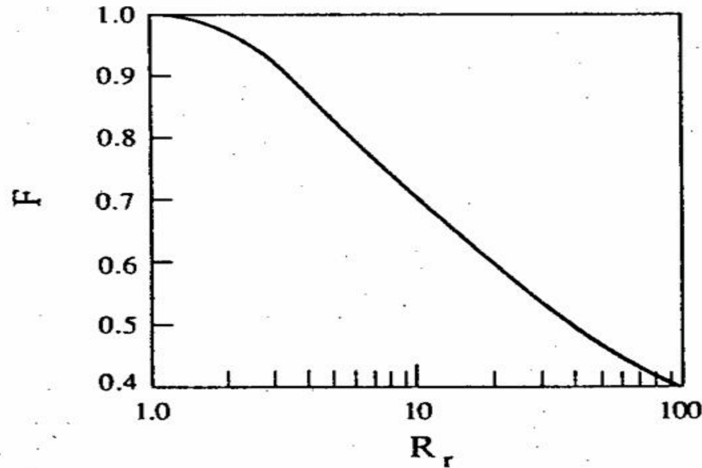

Figure 3.2: van der pauw correction factor plot [151]

where F can be a function of R_r, i.e., F = F(R_r).

Measurement of sheet resistance ρ_s

Sourcing current $I_{12} = 4.532mA$ between conacts 1 and 2, the potential difference between contacts 3 and 4 (V_{34}) was measured using electrometer. The potential difference measured in millivolts translates directly to resistance in ohms, and the sheet resitance is obtained using equation 3.7.

3.1.2 Contact Resistance

Contact resistance is characterized by two parameters: (a) the contact resistance (R_c) in ohms and (b) the specific contact resistance or specific contact resistivity r_c in ohm-cm^2.

The specific contact resistance includes in its definition not only the metal-semiconductor interface but also the regions immediately above and below the interface [151]. For the metal-semiconductor interface only, the specific interfacial resistance ρ_i is defined as,

$$\rho_i = \frac{\partial V}{\partial J}|_{V=0}. \tag{3.8}$$

Practically, the parameter of interest when contact resistance is measured is the specific contact resistance (r_c). It is independent of contact area, and it is a convenient parameter when comparing contacts of different sizes. The current density J in a metal-semiconductor contact is generally a function of the applied voltage and the barrier height. The current density under conditions of thermionic emission is [155]

$$J = A^{**}T^2 \exp(\frac{-q\phi_B}{kT}) \left(\exp(\frac{qV}{kT}) - 1 \right) \tag{3.9}$$

This expression is used to obtain the following expression for the specific interfacial resistance,

$$\rho_i(TE) = \frac{\partial V}{\partial J}|_{V=0} = \rho_1 \exp(\frac{q\phi_B}{kT}) \tag{3.10}$$

where $\rho_1 = \frac{k}{qA^{**}T}$ (TE = Thermionic Emission)

For the thermionic-field emission (TFE), the interfacial resistance is [156]

$$\rho_i(TFE) = C_1 \rho_1 \exp(\frac{q\phi_B}{E_o}), \tag{3.11}$$

and for field emission (FE),the expression for ρ_i is

$$\rho_i(FE) = C_2 \rho_1 \exp(\frac{q\phi_B}{E_{oo}}). \tag{3.12}$$

C_1 and C_2 are functions of the donor concentration (N_D), the temperature (T) and the barrier height (ϕ_B). E_{oo} is a characteristic energy for tunneling process [157]

$$E_{oo} = \frac{qh}{4\pi}\sqrt{\frac{N_D}{k_s \epsilon_o m^*}} \tag{3.13}$$

E_o is related to E_{oo} by [158]

$$E_o = F_{oo} \coth(\frac{E_{oo}}{kT}) \tag{3.14}$$

These are expressions for the specific interfacial resistance. However, it is not possible to obtain accurate theoretical expressions for the specific contact resistance. Experimental measurements yield the specific contact resistance which is contained implicitly in the specific interfacial resistance. That is, it is difficult to compare r_c with theory and ρ_i with experiment.

3.1.3 Linear Transmission Line Model Measurement

The transmission line model (TLM) diagramed in figure 3.3 is a simple method of measuring the total resistance (R_T) between two adjacent contact pads as a function of the inter-pad spacing (L). The ease with which the specific contact resistance and the semiconductor sheet resistance are estimated from the plot of the total resistance against inter-pad spacing is one of the advantages of using the TLM method compared to other methods. The total resistance between any two adjacent contacts is [159]

$$R_T = 2R_c + R_s \tag{3.15}$$

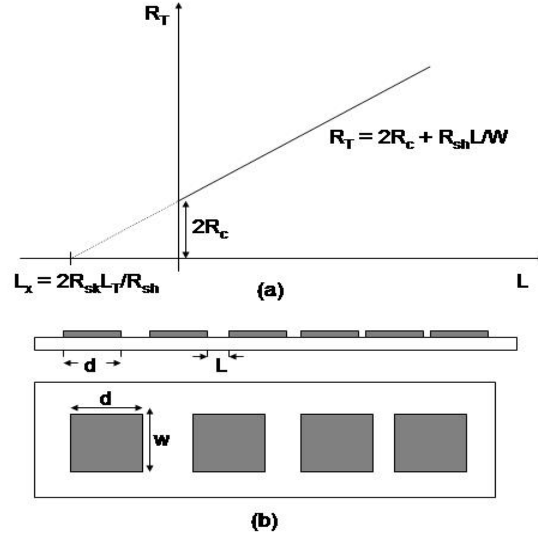

Figure 3.3: Plot of total contact to contact resistance as a function of inter-pad spacing [159]

where R_c is the contact resistance, and R_s is the resistance contribution from the semiconductor bwtween the pad edges.

$$R_T = 2R_c + \frac{R_{sh}L}{W} \tag{3.16}$$

The contact resistance R_c between metal and semiconductor can be described with a resistive network shown in figure 3.4 where [160]

$R_1 = \frac{r_c}{W\Delta x}$ and $R_2 = R_{sk}\frac{\Delta x}{W}$.

r_c is the specific contact resistance ($\Omega - cm^2$), R_{sk} is the modified sheet resistance of semiconductor (Ω/sq) under the contact, and W is the width of the contact. Using Kirchoff's law, the relation between voltages and currents at x and $x + \Delta x$ can be written as,

$V(x + \Delta x) - V(x) = I(x)R_2 = I(x)\frac{R_{sk}}{W}\Delta x.$ In the limit $\Delta x \rightarrow 0$,

$$\frac{dV}{dx} = I(x)\frac{R_{sk}}{W} \tag{3.17}$$

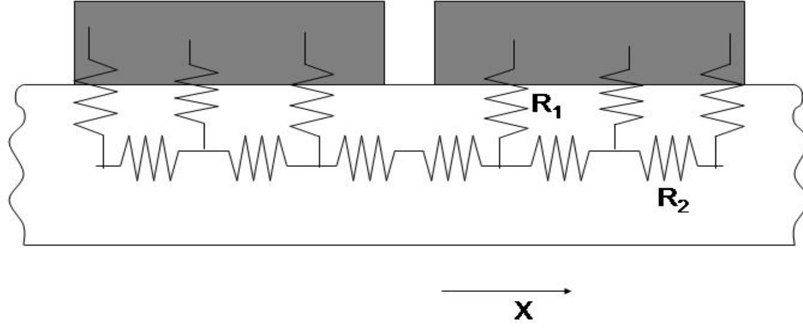

Figure 3.4: TLM resistive network [160]. The contact width W is into the page.

Also,

$I(x + \Delta x) - I(x) = \frac{V(x)}{R_1} = V(x)\frac{W}{r_c}\Delta x,$ and in limit limit $\Delta x \rightarrow 0$,

$$\frac{dI(x)}{dx} = V(x)\frac{W}{r_c}. \tag{3.18}$$

Combining the voltage and current equations yeilds a second order differential equation

$$\frac{d^2I(x)}{dx^2} = \frac{W}{r_c}\frac{dV}{dx} = I(x)\frac{R_{sk}}{W}\frac{W}{r_c} = \frac{R_{sk}}{r_c}I(x) \tag{3.19}$$

$\frac{d^2I(x)}{dx^2} = \frac{I(x)}{{L_T}^2}$ where $L_T = \sqrt{\frac{r_c}{R_{sk}}}$

L_T is referred to as the ”transfer length” or penetration length, and it is the characteristic length

over which the current flows under the contact. The general solution to the second order differential equation is

$$I(x) = I_o \frac{\sinh\left(\frac{d-x}{L_T}\right)}{\sinh\left(\frac{d}{L_T}\right)} \tag{3.20}$$

and

$$V(x) = I_o \frac{L_T R_{sk}}{W} \frac{\cosh\left(\frac{d-x}{L_T}\right)}{\sinh\left(\frac{d}{L_T}\right)}. \tag{3.21}$$

The contact resistance is

$$R_c = \frac{V(0)}{I(0)} = \frac{L_T R_{sk}}{W} \coth\left(\frac{d}{L_T}\right) \tag{3.22}$$

For $d \gg 2L_T, \qquad \coth\left(\frac{d}{L_T}\right) \approx 1$

and $\qquad R_c = \frac{L_T R_{sk}}{W}. \qquad$ Hence R_T becomes

$$R_T = \frac{2L_T R_{sk}}{W} + \frac{R_{sh} L}{W} \tag{3.23}$$

If the semiconductor sheet resistance under the contact is not significantly modified, we have $L_x \approx 2L_T$. For $d \gg L_T \;\Rightarrow\; R_{sk} \approx R_{sh}$, and

$$R_T = \frac{2\sqrt{r_c R_{sh}}}{W} + \frac{R_{sh} L}{W} \tag{3.24}$$

This equation implies a linear relationship between R_T and L. r_c and R_{sh} are calculated from the slope and intercept of the linear curve.

If $L_x \neq 2L_T$, that is $R_{sk} \neq R_{sh}$, the correct value of r_c can be found by additional measurement of the contact end resistance (R_E) [159]. The standard technique for measuring R_E is to pass a constant current between two adjacent contact pads and then measure the potential difference between one of the current pads and a third adjacent pad. It can be shown that R_E

is expressed as [161]

$$R_E = \frac{V}{I} = \frac{\sqrt{R_{sk} r_c}}{W} \frac{1}{\sinh\left(\frac{d}{L_T}\right)}. \tag{3.25}$$

However, $R_{sk} = \frac{r_c}{{L_T}^2}$, so that

$$\begin{aligned} R_E &= \frac{r_c}{L_T W} \frac{1}{\sinh\left(\frac{d}{L_T}\right)} \\ \frac{R_c}{R_E} &= \cosh\left(\frac{d}{L_T}\right) \end{aligned} \tag{3.26}$$

3.1.4 I-V Charateristics of Schottky Diodes

The Schottky diode is a "majority carrier device", and minority charge carriers play insignificant role in the determination of the I-V characteristic. For an n-type Schottky barrier, electron injection from the semiconductor into the metal dominates the observed current because of the relatively low potential barrier. However, recombination and hole injection currents still exist [44].

Injection of electrons or holes over a potential barrier is reffered to as thermionic emission current. High mobility semiconductors have I-V characteristics given by thermionic emission theory, provided the forward bias is not too large [50]. The thermionic emission current can be derived as follows. An electron in the semiconductor is capable of jumping over the potential barrier if it has a velocity v_x and kinetic energy,

$$\begin{aligned} K.E &= \frac{1}{2} m_n^* v_x^2 \geq q(V_{bi} - V_A) \\ |v_x| &\geq v_{min} \equiv \left[\frac{2q}{m_n^*}(V_{bi} - V_A)\right]^{1/2} \end{aligned} \tag{3.27}$$

where V_A is the applied potential. If there are n electrons per unit volume in the semiconductor with velocity v_x then the current will be, $dI_{s \to m} = -qAv_x n(v_x)$. Integrating over the velocity

differential,

$$
\begin{aligned}
I_{s \to m} &= -qA \int_{-\infty}^{-v_{min}} v_x n(v_x)\, dv_x \\
n(v_x) &= \left(\frac{4\pi k T {m_n^*}^2}{h^3}\right) \exp \frac{(E_F - E_c)}{kT} \exp - \left(\frac{m_n^*}{2kT}\right) {v_x}^2 \\
I_{s \to m} &= AC^* T^2 \exp(-\frac{\phi_B}{kT}) \exp(\frac{qV_A}{kT})
\end{aligned}
\tag{3.28}
$$

where

$$
C^* \equiv \left(\frac{m_n^*}{m_o}\right) \frac{4\pi q m_o k^2}{h^3} = 120 A cm^{-2} K^{-2} \left(\frac{m_n^*}{m_o}\right) \tag{3.29}
$$

Richardson constant = $120 A cm^{-2} K^{-2}$

Electrons going from the metal into semiconductor see a constant potential ϕ_B, where ϕ_B is defined in figure 3.5.

$$
I_{m \to s}(V_A) = I_{m \to s}(V_A = 0) = -I_{s \to m}(V_A = 0) = -AC^* T^2 \exp(-\frac{\phi_B}{kT}) = I_s \tag{3.30}
$$

Total current is

$$
I = I_{s \to m} + I_{m \to s} = I_{s \to m} + I_{m \to s}(V_A = 0) = I_s \left(\exp(\frac{qV_A}{kT}) - 1\right). \tag{3.31}
$$

For $V_A >$ a few kT/q, $I = I_s \exp \frac{qV_A}{kT}$ and

for $V_A >$ a few kT/q in the reverse bias mode, $I = -I_s$

The expressions above are for ideal diodes. However, real diodes exhibit phenomena such as breakdown voltage and reverse current that are not constant because the potential barrier ϕ_B is not constant. The barrier height ϕ_B associated with image force barrier lowering is expressed

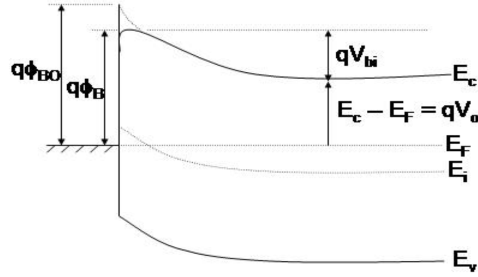

Figure 3.5: Effect of barrier lowering on barrier height

as

$$\phi_B = \phi_{BO} - \Delta\phi_B \tag{3.32}$$

$$q\phi_B = qV_o + qV_{bi} = q(V_o + V_{bi}) \tag{3.33}$$

The ideal barrier height becomes a good approximation if the diode is operated at a strong forward bias. I-V characteristics of a real diode depend on the barrier height that can be a function of the applied bias, under this condition an ideality factor (n) can be introduced into the thermionic current expression by including a linear, voltage dependent term in the modified barrier height expression. The thermionic current becomes [151],

$$I = I_s\left(\exp\left(\frac{qV_A}{nkT}\right) - 1\right) = I_s \exp\left(\frac{qV_A}{nkT}\right)\left(1 - \exp\left(-\frac{qV_A}{nkT}\right)\right). \tag{3.34}$$

$I_s = AC^*T^2 \exp(-\frac{q\phi_B}{kT})$, and the current density $J = I/A$ so that

$$J = C^*T^2 \exp(-\frac{q}{kT}(\phi_B - V_A/n)) \left(1 - \exp -\frac{qV_A}{kT}\right) \tag{3.35}$$

For $V_A \gg \frac{q}{kT}$,

$$J = C^*T^2 \exp(-\frac{q}{kT}(\phi_B - V_A/n)). \tag{3.36}$$

Taking the natural log of this equation yields

$$\ln J = C' - \frac{q}{kT}\phi_B + \frac{q}{nkT}V_A \tag{3.37}$$

where $C' = \ln C^*T^2$. A plot of $\ln J$ against V_A should be linear for $V_A >$ a few kT/q. The ideality factor n is determined from the slope, while the barrier height ϕ_B is determined from the intercept of the linear plot.

$$\begin{aligned} n &= \frac{q}{kT\,(slope)} \\ \phi_B &= \left[\ln(C^*T^2) - \ln J_i\right] \frac{kT}{q} \end{aligned} \tag{3.38}$$

However, removing the condition $V_A \gg q/kT$, a linear graph could be obtained for all V_A if what is ploted against V_A is $\ln \left[\frac{J}{\left(1 - \exp(-\frac{qV_A}{kT})\right)}\right]$.

The Richadson constant C^* is one major uncertainty in the J-V expression. It is modified to take into account the effective mass of electrons in the semiconductor, quantum-mechanical reflection of those electrons which are able to negotiate the barrier, and phonon scattering of the electrons between the top of the barrier (as determined by image forces) and the surface of the metal [50]. It can also depend on experimental factors such as semiconductor surface cleaning [162], annealing conditions, contact metal thickness and method of metal deposition [163].

Series resistance (r_s) is also present during diode operation. It depends on the semiconductor resistivity, contact resistance and sometimes on geometrical factors [151]. Series resistance can be included in the thermionic current expression by replacing (V_A) by ($V - Ir_s$), where (V) is the measured voltage across the entire diode including substrate and contact resistance. The current expression becomes

$$I = I_s \left(\exp\left(\frac{q(V - Ir_s)}{nkT}\right) - 1 \right). \tag{3.39}$$

The series resistance is obtained by plotting $I\frac{dV}{dI}$ or $\frac{dV}{d(\ln I)}$ against I, the slope is the series resistance, and the intercept is $\frac{nkT}{q}$ from which the ideality factor n can be obtained.

3.1.5 C-V Charateristics of Schottky Diodes

Schottky diodes exhibit capacitance associated with their depletion regions. In this regard, they are similar to p-n junction diodes. The capacitance of an n-type Schottky barrier is identical to that of an abrupt $p^+ - n$ junction, with the p^+ side behaving as the metal side of the Schottky diode. One major difference is that there is no minority carrier storage in a Schottky diode. There is also no diffusion capacitance.

The capacitance of a Schottky barrier resembles a parallel-plate capacitor with the separation between the plates controlled by the applied reverse bias potential. The differential capacitance ($C = \frac{dQ}{dV}$) is usually measured by superimposing a small alternating voltage on a reverse dc bias [50]. The differential capacitance depends on the applied reverse bias. Under favorable circumstances, measurements of the capacitance as a function of time and reverse bias voltage can yield not only the concentration of interfacial traps, but also their time constants and energies

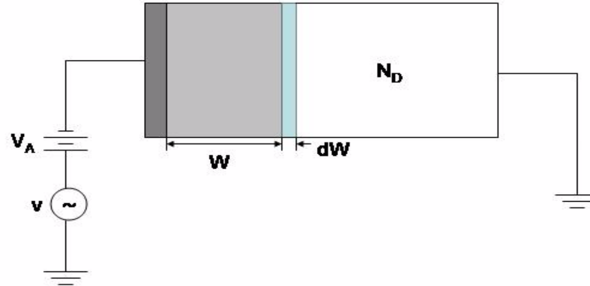

Figure 3.6: Capacitance measurements under applied bias [151]

relative to the band edges. Applied external stimuli such as light, temperature or forward bias can change the occupation of these traps.

Figure 3.6 shows an n-type Schottky diode with doping concentration N_D and an applied dc bias V_A. The differential capacitance is

$$C = \frac{dQ_s}{dV_A} \tag{3.40}$$

where dQ_s is the charge increment in the semiconductor and dV_A is the applied voltage increment.

The superimposed small amplitude ac voltage is typically applied at a frequency of 1MHz with an amplitude of 10 to 20mV. The ac voltage changing from zero to small negative value adds a small charge increment $-dQ_m$ to the metal contact. The semiconductor reacts to the charge increment in the metal with a corresponding charge increment of dQ_s leading to a slight

increase in space charge region (scr) width dW to maintain a overall charge neutrality [151].

$$dQ_s = qAN_D(W)\,dW \tag{3.41}$$

$$C = \frac{dQ_s}{dV_A} = qAN_D(W)\frac{dW}{dV_A} \tag{3.42}$$

For parallel plate capacitor

$$\begin{aligned} C = \frac{\kappa_s \epsilon_o A}{W} \Rightarrow \frac{dC}{dV_A} = \frac{-\kappa_s \epsilon_o A}{W^2}\frac{dW}{dV_A} \\ \frac{dW}{dV_A} = \frac{-W^2}{\kappa_s \epsilon_o A}\frac{dC}{dV_A} \end{aligned} \tag{3.43}$$

Using equations 3.42 and 3.43,

$$N_D(W) = \frac{C}{qA(dW/dV_A)} = \frac{-C^3}{qA^2\kappa_s\epsilon_o(dC/dV_A)} = \frac{2}{qA^2\kappa_s\epsilon_o\left[\frac{d(1/C^2)}{dV_A}\right]} \tag{3.44}$$

The doping concentration is obtained from a C-V measurement using the slope of the plot of $\frac{1}{C^2}$ against V_A and the dopant depth obtained from
$W = \frac{\kappa_s\epsilon_o A}{C}$. The width of the space charge region (W) extends only into the semiconductor and is negligible in the metal. The $\frac{1}{C^2} - V_A$ plot shows immediately the uniformity of the doping concentration, with a uniformly doped semiconductor characterized by a straight line.

The capacitance per unit area of a schottky diode is given by [164],

$$\frac{C}{A} = \sqrt{\frac{q\kappa_s\epsilon_o|N_D - N_A|}{2(V_{bi} + |V| - kT/q)}} \tag{3.45}$$

For an n-type substrate $N_D > N_A$ and $V < 0$, kT/q accounts for the majority carrier tail in the scr. The barrier height is related to the built-in potential V_{bi} by,

$\phi_B = V_{bi} + V_o$ and $V_o = \frac{kT}{q} \ln\left(\frac{N_C}{N_D}\right)$

The effective density of states is $N_C = 2\left[\frac{2\pi m_n^* kT}{h^2}\right]^{3/2}$.

For $N_A = 0$, the capacitance per unit area expression can be linearized as,

$$\left(\frac{A}{C}\right)^2 = \frac{2(V_{bi} - kT/q)}{q\kappa_s\epsilon_o N_D} + \frac{2|V|}{q\kappa_s\epsilon_o N_D} \tag{3.46}$$

Again the plot of $(A/C)^2$ against $|V|$ yeilds a slope and an intercept.

$slope = \frac{2}{q\kappa_s\epsilon_o N_D}$ $\Rightarrow$ $N_D = \frac{2}{q\kappa_s\epsilon_o (slope)}$

The intercept gives $V_i = V_{bi} - \frac{kT}{q}$

However $V_{bi} = \phi_B - V_o$ so that $V_i = \phi_B - V_o - kT/q$.

$$\phi_B = V_i + V_o + kT/q = V_i + \frac{kT}{q}\left[1 + \ln\frac{N_o}{N_D}\right]. \tag{3.47}$$

3.2 Physical Analysis

3.2.1 Rutherford Backscattering Spectrometery (RBS)

Introduction

The model of an atom as a positive nucleus enclosed by cloud of negative electrons was put forward by Ernest Rutherford and confirmed experimetally by Geiger and Marsden (1913). They reported sinlge collision, large angle, scattering of alpha particles by positively charged nuclei. Their experiment not only established Rutherford's model but also formed the basis for Rutherford Backscattering Spectrometry (RBS) as a modern analytical technique [166].

Rutherford backscattering is simply understood because it is a classical scattering process in a central force field. High energy helium ions undergo close-impact collisions which are

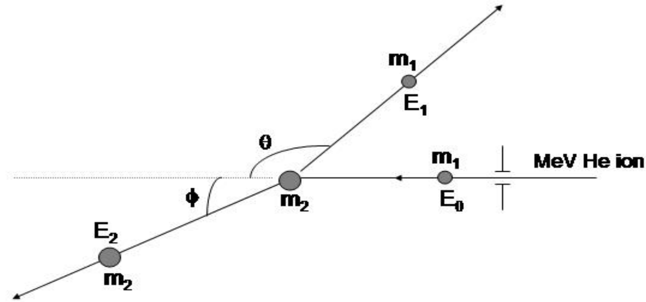

Figure 3.7: Close impact collision and backscattering [166]

governed by coulomb repulsion between the positively charged incident projectile and the nuclei of the target atoms.

Definitions

kinematic factor in an elastic collision

A very small fraction of incident beam is backscattered on collision with atomic nuclei. Backscattered particles of energy (E_1) get to the detector. The reduction in the energy of the particles ($E_1 < E_o$) is a function of the mass of the incident particle and the target nucleus. Assuming an elastic collision, the principles of conservation of kinetic energy and momentum can be applied to obtain a solution for the kinematics of the collision. The collision is depicted in figure 3.7.

Kinetic energy conservation:

$$\frac{1}{2}m_1{v_0}^2 = \frac{1}{2}m_1{v_1}^2 + \frac{1}{2}m_2{v_2}^2 \tag{3.48}$$

Momentum conservation:

$$\begin{aligned} m_1v_0 &= m_1v_1\cos\theta + m_2v_2\cos\phi \qquad (x-direction) \\ 0 &= m_1v_1\sin\theta - m_2v_2\sin\phi \qquad (y-direction) \end{aligned} \tag{3.49}$$

Solving the kinetic energy and momentum conservation equation yield,

$$\begin{aligned} \frac{v_1}{v_0} &= \pm\frac{({m_2}^2 - {m_1}^2\sin^2\theta)^{1/2} + m_1\cos\theta}{m_1+m_2} \\ \Rightarrow \frac{E_1}{E_0} &= \left[\frac{({m_2}^2 - {m_1}^2\sin^2\theta)^{1/2} + m_1\cos\theta}{m_1+m_2}\right]^2 \end{aligned} \tag{3.50}$$

The ratio of the backscattered energy to incident energy is called the kinematic factor ($k = E_1/E_0$). The eqation aboved shows that k is determined only by the masses of incident particle and target atom and by the scattering angle, θ. For a fixed incident particle mass and scattering angle, k becomes a function of the target mass m_2 only. Therefore, the energy of backscattered particle is a direct signature of the target atom.

In practice, when a target contains two types of atoms that differ in massses by a small amount Δm, it is important that this difference produce as large a change in ΔE_1 as possible. This gives the largest Δk when $\theta = 180°$ (ideal location for a detector). $\theta = 170°$ is a practical location because of detector size. It is this arrangement that has given the method its name, Backscattering Spectrometry [167]. Quantitatively,

$$\Delta E_1 = E_o\left(\frac{dk}{dm}\right)\Delta m \tag{3.51}$$

Every practical detection system has a finite resolution. If ΔE_1 falls below this limit, the distinction between two masses is lost. To obtain good mass resolution, it is desirable to [167]:

(1) increase the incident particle energy E_o

(2) use a large projectile mass m_1, but with $m_1 < m_2$

(3) measure at scattering angle as close as possible to 180°

Scattering cross section σ

After an elastic collision, the target atom is identified by the energy lost by the scattered particle. The collision probability between the incident particle and the target nucleus is determined by the number of target nuclei per unit area. The scattering cross section relates the number of target nuclei to the number of particles detected after scattering. For particles scattered through an angle θ into a differential solid angle, $\Delta\Omega$, the differential scattering cross section is defined as

$$\frac{d\sigma}{d\Omega} = \frac{1}{Nt}\left[\frac{dQ/\Omega}{Q}\right] \tag{3.52}$$

Q is the total number of incident particle on the target. dQ is the number of particles getting to the detector. N is the volume density of atoms in the target, and t is the sample thickness. Hence, Nt is the number of target atoms per unit area (areal density). $d\sigma/d\Omega$ has the dimension of area, and it can be interpreted as the effective area each nucleus presents to the incident beam. In backscattering spectrometry, the detector solid angle Ω is small ($\sim 10^{-2}$ sterradian or less). The average differential scattering cross section is defined as

$$\sigma(\theta) = \frac{1}{\Omega}\int_{\Omega}\frac{d\sigma}{d\Omega}d\omega \tag{3.53}$$

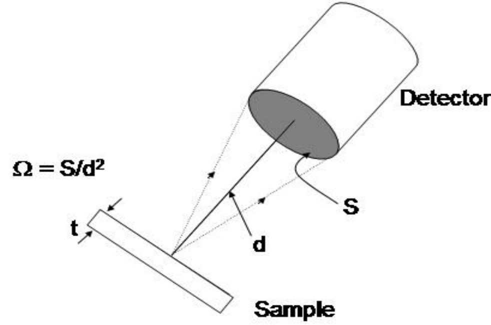

Figure 3.8: $\Omega = S/d^2$ = detector solid angle. S = detector area. d = detector-target distance. t = target thickness.

The number of particles detected by the detector is called the yield and is given by,

$$Y = \sigma(\theta)\Omega Q N t \tag{3.54}$$

Q is determined by time integration of the current of charge particles incident on the target.

In the backscatteing spectrometry, it is assumed that the incident particle is scattered by the unscreened nucleus of the target atom because the distance of closest approach is well within the inner electron orbits. The unscreened scattering cross section originally derived by Rutherford is

$$\frac{d\sigma}{d\Omega} = \left(\frac{\kappa Z_1 Z_2 e^2}{2E}\right)^2 \frac{1}{\sin^4\theta}. \tag{3.55}$$

$Z_1 e$ is the incident particle charge and $Z_2 e$ target particle charge.

Rutherfor assumed that the target atom was infinitely heavy while deriving the scattering cross

section expression. If the target atoms are considered to have finite mass, then the collision becomes a two-body central force problem which can be analyzed as a one-body collision by replacing m_1 by the reduced mass $\mu = m_1 m_2/(m_1 + m_2)$. The modified scattering cross section becomes

$$\frac{d\sigma}{d\Omega} = \left(\frac{\kappa Z_1 Z_2 e^2}{2E}\right)^2 \frac{4}{\sin^4\theta} \frac{\left[\left(1 - \left(\frac{m_1}{m_2}\sin\theta\right)^2\right)^{1/2} + \cos\theta\right]^2}{\left(1 - \left(\frac{m_1}{m_2}\sin\theta\right)^2\right)^{1/2}}. \qquad (3.56)$$

For the coulomb potential to govern the backscattering process, distance of closest approach, d, must be less than k-shell electron radius, estimated to be a_o/Z_2, $a_o = 0.53\mathring{A}$, the Bohr radius.

$$E = \frac{Z_1 Z_2 e^2}{d} \qquad and if \qquad d < a_o/Z_2, \qquad E > \frac{Z_1 {Z_2}^2 e^2}{a_o}. \qquad (3.57)$$

$E \sim 10keV$ for a Si target and $E \sim 340keV$ for scattering from Au. Because part of the trajectory will always be outside the electron cloud leading to deviation from Rutherford scattering cross section, the screened coulomb cross section is
$\sigma_{sc} = \sigma(\theta)F$ where $F = \left(1 - \frac{0.049 Z_1 {Z_2}^{3/4}}{E}\right)$ and E is in keV. For 1MeV He ions incident on Au, $F \approx 3\%$. For 2MeV He ions, the screening correction can be neglected for most targets [166, 167].

Energy loss (dE/dx) and stopping cross section (ε)

Composition depth profiles can be obtained from RBS analysis. The depth scale is determined by the energy loss at high energies as the incident particles traversed the sample. Energy is lost by energetic particles mostly through excitation and ionization during inelastic collisions

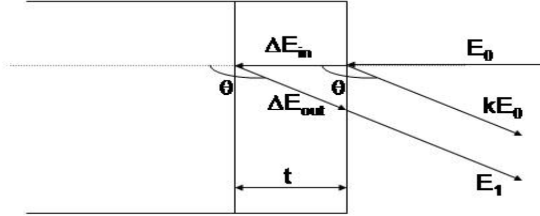

Figure 3.9: Energy loss during inward and outward trajectory of incident particle [166]

with atomic electrons. Energy loss due to an interaction with the nucleus, is much less than electronic energy loss. The amount of energy ΔE lost per distance Δx by a particular ion depends on the density and composition of target and on the ion energy. For an incident energy E_o, the ion energy at any depth x can be written as

$$E(x) = E_o - \int_0^x \frac{dE}{dx} dx \tag{3.58}$$

The stopping cross section ε can be defined as

$$\varepsilon = \frac{1}{N} \frac{dE}{dx} \left(eV - cm^2 \right) \tag{3.59}$$

where N is the atomic density.

In a compound target, the total energy loss is the sum of the losses to each of of the constituent elements weighted by the abundance of each element. This postulate is known as Bragg's

rule, and it states that the stopping cross section of SiO_2 for example is given by

$$\epsilon^{SiO_2} = (1)\epsilon^{Si} + (2)\epsilon^{O} \tag{3.60}$$

where ϵ^{Si} and ϵ^{O} are the stopping cross section of the atomic constituents. ϵ^{SiO_2} is sometimes called the stopping power per molecule, and $\frac{dE}{dx} = N\epsilon^{SiO_2}$. N is the number of molecules per volume.

Energy width and depth profile

In thin films, the total energy loss, ΔE, into a depth x is proportional to x. This is true if dE/dx is constant, which is a good assumption if E_o is large ($>$ 1MeV) and x is the order of a few microns.

$$\Delta E_{in} = \int_0^x \frac{dE}{dx}dx \approx x\frac{dE}{dx}|_{in} \tag{3.61}$$

The energy at depth x is

$$E(x) = E_o - x\frac{dE}{dx}|_{in}. \tag{3.62}$$

After large angle scattering, the ion energy can be written as

$$E_1(x) = kE(x) - \frac{x}{|\cos\theta|}\frac{dE}{dx}|_{out} \tag{3.63}$$

where k is the kinematic factor, θ is the scattering angle and $x/\cos\theta$ is the path length traveled by the ion after scattering.

$$\begin{aligned} E_1(x) &= k\left(E_o - x\frac{dE}{dx}|_{in}\right) - \frac{x}{|\cos\theta|}\frac{dE}{dx}|_{out} \\ E_1(x) &= -x\left[k\frac{dE}{dx}|_{in} + \frac{1}{|\cos\theta|}\frac{dE}{dx}|_{out}\right] + kE_o \end{aligned} \tag{3.64}$$

The energy width ΔE is

$$\Delta E = kE_o - E_1(x) = x\left[k\frac{dE}{dx}|_{in} + \frac{1}{|\cos\theta|}\frac{dE}{dx}|_{out}\right] = xS \tag{3.65}$$

E_{in} and E_{out} are the energies at which dE/dx is evaluated. S is the backscattering energy loss factor.

In evaluating dE/dx, two possible approximations can be adopted

(i) The surface energy approximation SEA is a good approximation for very thin films ($x < 0.5\mu m$). In this case, dE/dx is evaluated at $E_{in} = E_o$ and $E_{out} = kE_o$.

(ii) The mean energy approximation MEA is used when path length traversed by the ions is $> 0.5\mu m$, dE/dx is evaluated at at mean energies

$\overline{E_{in}} = \frac{1}{2}[E_o + E(x)]$ and $\overline{E_{out}} = \frac{1}{2}[E_1 + kE(x)]$

Assuming also that the measured ΔE is divided equally between the inward and outward paths, we have approximately $E(x) = E_o - \frac{1}{2}\Delta E$. Then

$\overline{E_{in}} = [E_o - \frac{1}{4}\Delta E]$ and $\overline{E_{out}} = [E_1 + \frac{1}{4}\Delta E]$.

The energy E_1 of the detected particle can be related to the depth x at which backscattering occurs. For elemental samples with incident particles striking the sample surface perpendicularly, along the inward and outward paths, respectively,

$$x = \int_{E_o}^{E} \frac{dE}{(dE/dx)} \tag{3.66}$$

$$\frac{x}{\cos\theta} = -\int_{kE}^{E_1} \frac{dE}{(dE/dx)} \tag{3.67}$$

Since E_o and E_1 are the energies in these expressions that can be measured experimantally, it is necessary to obtain x in terms of E_o and E_1. There are three ways of doing this

(1) Assume dE/dx is constant over each path, then the equations can be integrated and E elliminated. This assumption leads to a linear relationship between ΔE and x. Constant dE/dx is an approximation, and the resulting depth scale is subsequently approximate.

(2) Use tabulated values of dE/dx and carry out the integration numerically to find corresponding sets of E and x, and therefore kE and E_1. The numerical calcultaion can be done by dividing the sample into many slabs of equal width Δx small enough that dE/dx can be assumed constant. Alternatively, the sample can be divided into slabs of differing thicknesses such that particles scattered from two boundaries of all slabs have fixed energy difference at detector.

(3) Assume some functional dependence for dE/dx. Matching pairs of E and x and of x and E_1 can then be obtained analytically.

The linear accelerator facility at Auburn

The accelerator at Auburn University (figure 3.10) is a 6SDH-2 pelletron tandem machine purchased from the National Electrostatics Corporation. It has two ion sources, allowing for a wide range of applications. Helium ion beams are produced from an rf exchange ion source, and a wide range of heavy ions are available from the SNICS II (Source of Negative Ions by Cesium Sputtering). For example, nitrogen, aluminum, silicon, phosphorous and gold can be accelerated with energies that range from 100keV to 8MeV. The accelerator is currently used for Rutherford backscatering Spectrometry (RBS), light ion channeling (LIC), nuclear reaction analysis (NRA) and heavy ion implantation (HII). [168].

Ion sources(figure 3.11)

Helium RF Source - Helium gas is bled into a quartz bottle, and the gas is ionized by an 100MHz RF oscillator. The resulting He^{+} is separated by applying about 6kV potential to push the ions

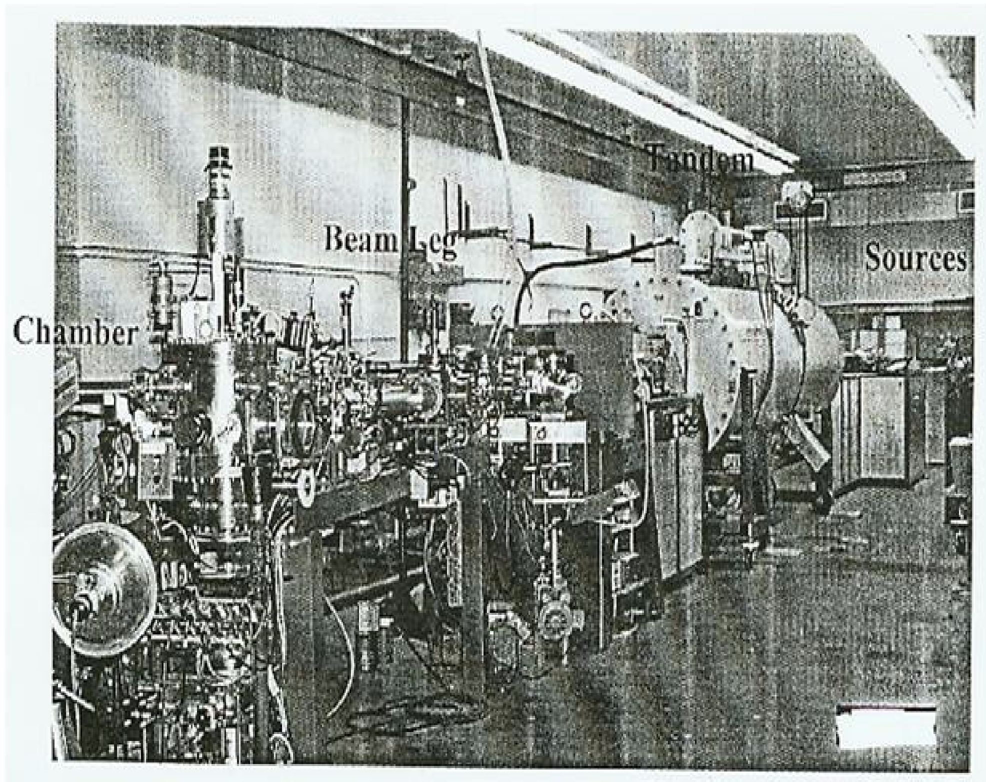

Figure 3.10: Pelletron tandem accelerator at Auburn University

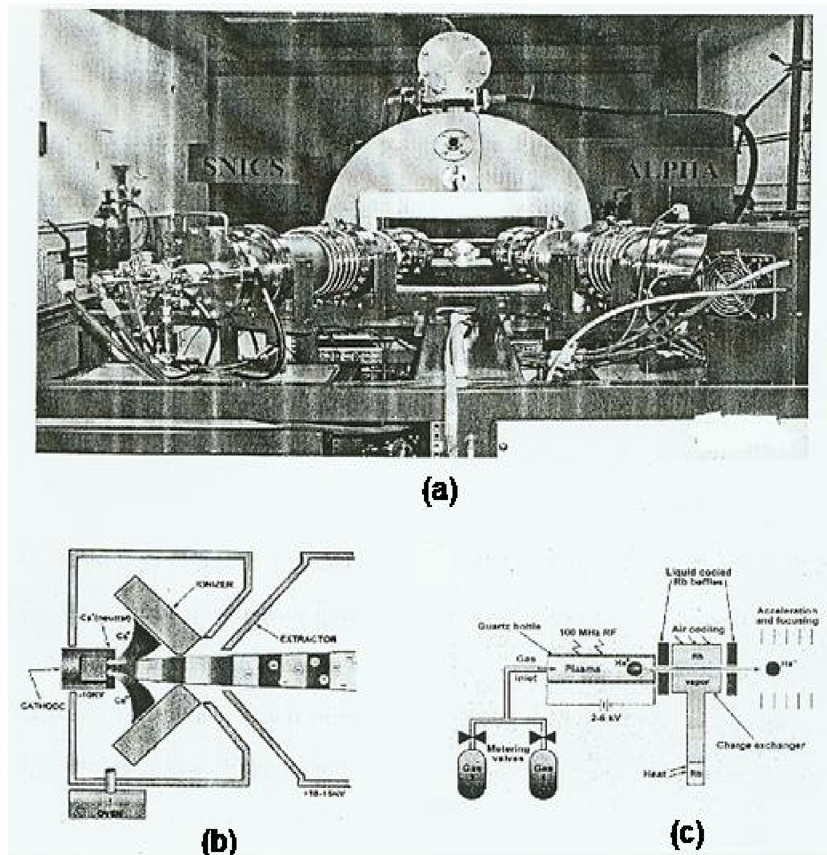

Figure 3.11: (a) Sources section of the accelerator. Illustrations of (b) SNICS source (c) He ion source [168]

through an exit aperture. The He^{+} ions then enter the charge exchange chamber where they are neutralized by Rubidium (Rb) vapor. Some neutralized ions undergo further charge exchange to become He^{-}. The output of RF source is about $100 - 200\mu A$ of neutral He and $1 - 4\mu A$ of He^{-}. Rubidium is used in the charge exchange process because of its high cross section for He^{-} production [169, 170]. To maintain a good charge exchange, the Rb is heated in an oven kept at $250°C$ and circulated in the charge exchange chamber that is warmed to $55°C$ [21].

SNICS Source - Cesium ions (Cs^+) used for sputtering are produced by immersing a tantalum ionizer in a Cs vapor. The ionized Cs is accelerated towards a cold cathode biased at -15kV. The cathode is made of material whose ions are to be accelerated. Cs^+ ions sputter the cathode material, and cathode ions which become negatively charged as they moves through the Cs vapor, repeled by the cathode dias. The negative ion current is a function of many parameters including the cathode composition, cathode potential, Cs^+ flux, etc. It is possible to generate currents of up to several hundred microamps for most heavy elements [21].

Charging system

Pelletron charging chain was developed in the mid 1960s as an improvement over the older Van de Graff charging belt [171]. The chains are made of metal pellets connected by insulating nylon links. The chain is more durable and produces greater terminal stability compared to the belt. The chain eliminates dust from the belt and does not limit ultimate terminal potential.

Pelletron charging system also offers significant advantages over solid state charging systems that require fragile electronics in the high voltage column. A solid state system also takes long time to condition to voltage in order to avoid terminal sparking.

Pelletron chains are charged by a induction scheme instead of corona discharge [171]. To generate a positive terminal voltage, the inductor is negatively charged and pushes electrons off the pellet while they are in contact with the grounded driven pulley. The chain subsequently transports positive charge to the high voltage terminal where the reverse charging process occurs. The chain passes through a suppressor (negatively biased for positively charge chain) to prevent arcing as the pellets make contact with the terminal pulley. Figure 3.12 shows a pelletron charging system. This system can provide a two-way charging (up-charging and down-charging), the difference between ”up” and ”down” is in the reversal of the polarity of the inductor/suppressor.

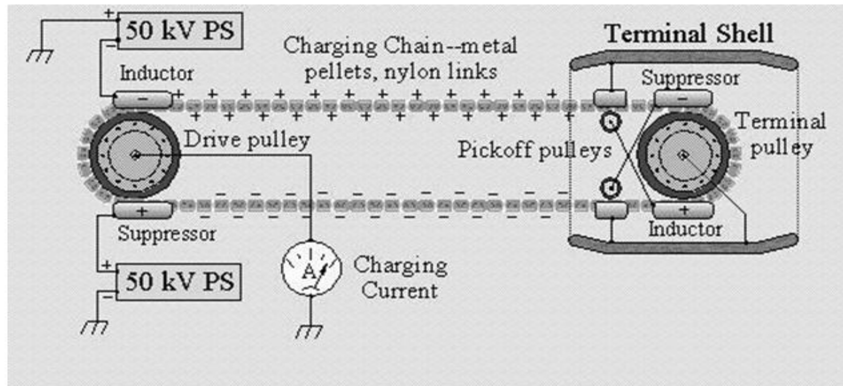

Figure 3.12: Pelletron charging system [171]

The two-way charging system effectively doubles the charging current capacity of the chain. Depending on the design, this system can deliver charging currents of $100 - 200\mu A$ or more per chain to the high voltage terminal.

Acceleration and focus

Ions from the ion source are accelerated to the high voltage terminal. Inside the terminal, the ions collide with Ar or N_2 molecules from a low pressure source. These collision strip electrons to create positive ions that experience a second acceleration due to repulsion from the high voltage terminal. This double acceleration mode of operation where the two ends of the accelerating column are grounded, is called a ”tandem” configuration. Positive ions of different charge state leave the terminal region, and it is imporant to be able to select ions of single charge state and species. An analyzing magnet is used for this purpose. Passing ions through an arc of radius R, with the acceleration terminal voltage V, in a magnetic field B, particular ions with a

charge-to-mass ratio (q/m) will be able to successfully traverse the arc.

$$R = \frac{mv}{qB} = \frac{1}{B}\left(\frac{2m}{q}V\right)^{1/2} \tag{3.68}$$

The RBS beam leg attached to the analyzing magnet (figure 3.10) is 12° left off the direction of the ion beam as it enters the magnet [21]. Ions of specific species, charge state and energy can be selected for the beam leg where the ions are passed through two small apertures for collimation. A faraday cup (biased Ta cone) is used to measure the beam current. The cup is moved in or out of the beam path by a pneumatic cylinder. When the cup is out of the beam path, the beam can get to the samples mounted on a goinometer with computer control of three degrees of freedom - up/down, rotation about a vertical axis and rotation about a horizontal axis.

Detector

RBS and channeling experiments use a solid state surface barrier detector (sbd) mounted at 170° wih respect to the incident beam direction. The detector is a silicon diode with a very thin p-type surface layer [172]. The detector is reverse biased and incident charge particles incident create electrons and holes that are swept in opposite directions to collection electrodes by the electric field in the depletion region. The amount of collected charges is proportional to the incident particle energy. Charge pulses are subsequently converted electronically to voltage pulses.

The beam current integration (BCI) systems counts the number of charged particles incident on the target. About 99.99% of the particles incident on target come to rest in he target, and these induce current in the sample [21]. Detector calibration is performed using ^{241}Am which gives an alpha particle of energy 5.486MeV. This energy is used to calibrate a precision pulse generator

that is in turn used to simulate detector signals at the input of the detector pre-amplifier. Typically a pulse height spectrum with known energies between 0 and 2MeV is accumulated [21].

3.2.2 Auger Electron Spectroscopy (AES)

When an inner shell vacancy is created in an atom by a photon, energetic electron or proton, the excited atom relaxes to equilibrium either radiatively or non-radiatively. For radiative de-excitation, a higher shell electron make a transition to occupy the inner shell vacancy, releasing radiation (photons) in the process. For non-radiative de-excitation, the higher shell electron makes the transition to the inner shell vacancy, and the energy released causes the ejection of secondary electrons (Auger electrons) without emission of photon radiation.

The detection of Auger electron emission dates to the work of P. Auger in 1925 [173]. Auger electron characteristic energies uniquely identify the element from which electrons are ejected. The energy of an Auger electron is determined by the differences in binding energy associated with the de-excitation as the atom rearranges its electron shells by emitting electrons with characteristic energy [166]. An illustration of Auger de-excitation is shown in figure 3.13. The transition nomenclature (KL_1L_1) implies an initial vacancy in the K shell. An outer L_1 electron fills the vacancy, and the energy released is given to another L_1 electron which is ejected from the atom. The Coster-Kronig transition in which the primary vacancy and one of the final state vacancies lie in the same shell has a higher probability than the normal Auger transition, and so affects the relative Auger line intensities.

Auger energies and intensities

Radiationless process consist of transitions involving holes (vacancies). The initial hole can be characterized by the following quantum numbers: principal, angular momentum, magnetic

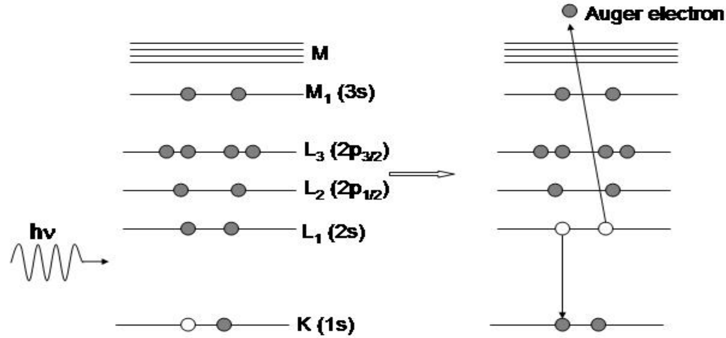

Figure 3.13: Illustration of auger electron de-excitation [166]

and spin $(n\,l\,m_l\,m_s)^i$, and the final two vacancies by $(n\,l\,m_l\,m_s)$ and $(n\,l\,m_l\,m_s)'$ [174]. The transition is

$(n\,l\,m_l\,m_s)^i \longrightarrow (n\,l\,m_l\,m_s)(n\,l\,m_l\,m_s)'$

Enery calculations are carried out via theoretical techniques, a semi-empirical approach or a totally empirical technique based on simplified equations.

Empirical Methods

The simplest equation for the energy of Auger electron is

$$E_{uvw}(z) = E_u(z) + E_v(z) + E_{w'}(z) \tag{3.69}$$

where $E_u(z)$ is the energy level in which the initial hole is located, $E_v(z)$ is the energy level from which an initial electron falls to fill the initial hole, $E_{w'}(z)$ is the energy appropriate to an atom singly ionized after the Auger electron has been ejected from energy level w. $E_{uvw}(z)$ is

the auger energy of the transition uvw of element z. $E_u(z)$ and $E_v(z)$ can be approximated as the atomic binding energies of electrons in the u and v energy levels.

$E_{w'}(z) = E_w(z) + \Delta E_w(z)$ where $\Delta E_w(z) = \frac{1}{2}[E_w(z+1) - E_w(z) + E_v(z+1) - E_v(z)]$.

Therefore,

$$E_{uvw}(z) = E_u(z) - E_v(z) - E_w(z) - \frac{1}{2}[E_w(z+1) - E_w(z) + E_v(z+1) - E_v(z)] \quad (3.70)$$

Transition probabilities

The Auger transistion probability W_A in hydrogenlike atom (KLL transition) can be written, according to first-order perturbation theory, as [166]

$$\begin{aligned} W_A &= \frac{2\pi}{\hbar}\rho(k)|\varphi_f(\overrightarrow{r_1})\psi_f(\overrightarrow{r_2})\frac{e^2}{|\overrightarrow{r_1} - \overrightarrow{r_2}|}\varphi_i(\overrightarrow{r_1})\psi_i(\overrightarrow{r_2})d\overrightarrow{r_1}\, d\overrightarrow{r_2}|^2 \\ \rho(k) &= m\left(\frac{V}{8\pi^3\hbar^2}\right) k \sin\theta\, d\theta\, d\phi \end{aligned} \quad (3.71)$$

where $\rho(k)$ is the density of states associated with normalization.

Practical considerations

Auger electron transitions generally appear as small features superimposed on the large background of secondary electrons. A derivative technique $dN(E)/dE$ is used to minimize the slowly varying background and to enhance observation of the Auger electron signals. Electronic differentiation of the energy distribution function $N(E)$ is readily achieved with a velocity analyser by superimposing a small ac voltage on the energy selector voltage and synchroniously detecting the power output of the electron multiplier. Auger peak-to-peak height of the differentiated signal is a direct measure of the surface concentration of element that produces the Auger electrons.

The sensitivity of Auger technique depends on the transition probability W_A, the incident beam current and energy, and the collection efficiency of the analyser. The limit of detection for the elements varies between approximately 0.02 and 0.2 atomic percent [175].

Qualitative and quantitative analysis

Principal Auger peaks of KLL, LMM and MNN Auger transitions allow identification of all elements above He by scanning the 0-2keV energy range. Major Auger peaks can be identified by using the Principal Auger Electron Energies Chart to reduce the number of possibilities before attempting a detailed analysis of a standard Auger spectrum. A peak shift of a few eV can be considered insignificant if the element is in a different chemical environment from that used for the standard spectrum.

The relationship between Auger electron signal and atomic concentration can be determined as a function of instrumental parameters such as the primary electron beam current (I_p), the primary beam energy (E_p) and for the modulation energy (E_m) [175]. There is a linear relationship between Auger peak-to-peak amplitude and I_p as long as the incident electron beam diameter does not exceed the analyser source diameter, and the current density is not too large to damage the sample surface.

The Auger signal amplitude is proportional to the modulation energy when the modulation energy is small compared with the Auger peak width. For large modulation amplitudes, the peak is broadened and peak-to-peak amplitude becomes nonlinear with E_m. Auger peak-to-peak amplitudes vary with the primary beam energy E_p because of the energy dependence of the electron impact ionization cross section for the core level involved in Auger transition. The Auger yield rises abruptly from zero as E_p crosses the ionization threshold E_c and increases to a maximum for $E_p/E_c \geq 5$ [175].

A first order approximation for quantitative analysis can be accomplished through comaprison of the Auger signal from the sample to the Auger signal from a pure standard. To avoid the need for a large number of elemental standards, another method comparing the signal from the sample with that from a pure silver target has been adopted. Setting E_p to a standard value and E_m low enough to prevent significant distortion due to excessive modulation, the atomic concentration of element X is

$$C_x = \frac{I_x}{I_{Ag} S_x D_x} \tag{3.72}$$

I_x is the peak-to-peak amplitude of element X from the test specimen, and I_{Ag} is the peak-to-peak amplitude from the Ag standard. The relative scale factor between spectra for the sample and the silver standard is

$$D_x = \frac{L_x E_{m,x} I_{p,x}}{L_{Ag} E_{m,Ag} I_{p,Ag}} \tag{3.73}$$

L_x is the lock-in amplifier sensitivity, $E_{m,x}$ is modulation energy and $I_{p,x}$ is the primary beam current.

Without elemental or silver standards, it is possible to express the atomic concentration as

$$C_x = \frac{I_x}{S_x d_x} / \left(\sum_\alpha \frac{I_\alpha}{S_\alpha d_\alpha} \right) \tag{3.74}$$

The sumation is over one peak per element and $d_x = L_x E_{m,x} I_{p,x}$ is the scale factor.

This simple quantitative technique has some inherent errors which include:

(1) matrix effects on electron escape depth and backscattering factors

(2) chemical effect on peak shapes

(3) surface topography

Auger electron escape depth dependence on electronic sttructure of the host material may alter

the depth measurement in the specimen relative to that in a standard. Chemical effect can cause a change in the peak shape and lead to error using peak-to-peak heights of differentiated spectrum. Highly polished surfaces produce larger Auger signals than rough surfaces [175].

The combination of RBS and AES is quite useful in depth profile analysis because RBS gives quantitative information on depth and heavy mass constituents without the complications of intermixing during sputtering. Ion sputtering causes a change in the composition of the surface layer due to surface segregation and preferential sputtering. Compared to RBS, AES depth profiling provides better depth resolution and is sensitive to both heavy and light elements.

3.2.3 X-ray Photoelectron Spectroscopy (XPS) [166]

Photoelectron spectroscopy is one of the major surface analytical tools. This technique arises directly as a result of the interaction between photon and atoms. The source of photons incident on the sample can be ultraviolet light (UPS) or X-ray (XPS). This technique is otherwise called ESCA (Electron Spectroscopy for Chemical Analysis), especially if the focus is on chemical bonding in the sample. A wide range of photon energies can be be used for analysis. Photons with energy as low as 10eV can interact with valence electrons and provide information about chemical bonding in the sample. For elemental identification however, much higher photon energy is required. Photons with energy as high as 0.1MeV can penetrate solids and interact with inner shell electrons. A major advancement for this technique came with the advent of electron synchrotron facilities that provide intense monochromatic photon beams over a broad range of energies. Most laboratory instruments produce X-rays in the 1 - 10keV region.

When a sample is exposed to photons of energy $\hbar\omega$, it absorbs the quantized energy and electrons are ejected from the material. The kinetic energy of an ejected electron is related to the binding energy of an electron in the atom. The energy of the electron also gives the identity

of the element from which the electron is ejected. Photoelectron spectroscopes require both a source of monochromatic radiation and an electron spectrometer.

Sources

UPS generally uses a resonant light source such as a He discharge lamp with energies in the $16 - 41eV$ range. This energy is sufficent for the analysis of the valence band density of states for most solids.

Depending on X-ray energy of interest, characteristic X-ray for XPS analysis is provided by electron bombardment of targets. Magnesium and aluminum targets are used predominantly, and they produce soft X-rays ($\sim 1keV$). Hard X-rays can be produced with a Cu target ($\sim 8keV$), and the associated energy width is about 2.0eV. Molybdenum also gives hard characteristic X-ray energies ($\sim 17keV$) with an energy width of about $6eV$. Because of the poor energy resolution, most of these sources are not suitable for high resolution studies.

Synchrotron radiation from electron storage rings can provide a continuous spectrum with intensities much higher than X-ray or resonance light sources. The use of polarized tunnable radiation from the synchrotron is a distinct advantage in experimental investigations, but access to synchrotron facilities is limited.

Detection system

The electrostatic analyzer is used primarily to determine the energy of photoelectrons. Deflection and reflection (mirror) are the two general operating modes for analyzers. The cylindrical mirror analyzer (CMA) is a common type. Deflection is caused by the potential difference between the inner and outer cylinders. CMAs maintain a constant energy resolution. The

electron analyzer measures the number of photoelectrons at different kinetic energies, and the information is displayed as a spectrum of photoelectron intensity as a function of binding energy.

Quantitative analysis

In quantitative analysis, the area under a photoelectron peak or the line intensity is used. Line intensity depends on factors such as photoelectric cross section σ, the electron escape depth within the sample λ, the spectrometer transmission, surface roughness or inhomogeneities and the presence of satellite structures.

Chemical analysis of a sample with component elements A and B can give the relative concentration, n_A/n_B, in terms of the peak intensities and cross sections if photopeaks from A and B have about same energy and same detection efficiency,

$$\frac{n_A}{n_B} = \frac{I_A}{I_B}\frac{\sigma_B}{\sigma_A} \tag{3.75}$$

Photoelectron peak area can also be compared to known standard for quantitative analysis.

3.2.4 X-ray Diffraction (XRD)

X-ray diffraction is one of the most common tools for material characterization because of its simplicity, reliability and nondestructive nature [176]. The basis of X-ray diffraction is the Bragg equation which describes the condition for constructive interference for X-ray scattering from atomic planes of a crystal.

$$2d\sin\theta = n\lambda \tag{3.76}$$

X-ray diffraction is useful in many technological applications. It is used to identify the crystalline phases present in materials and to measure structural properties such as strain state, grain size,

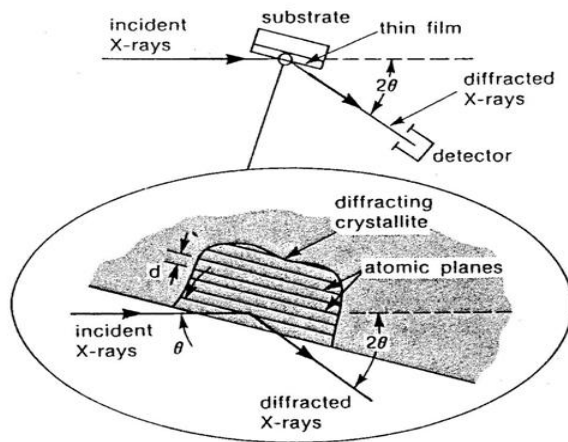

Figure 3.14: X-ray diffraction geometry [177]

defect structure, phase composition and preferred orientation (figure 3.14). It is also used in thin films and multilayer films to determine thicknesses and atomic arrangement in amorphous materials. In packaging materials evaluation, XRD can be used to investigate diffusion and phase formation at interfaces[177]

For ultra thin film analysis (thickness $< 100nm$), the conventional Bragg-Brentano ($\theta - 2\theta$) X-ray geometry (figure 3.15a) is not very useful because of interference effects from the substrate. A better geometry is a low incidence angle (glancing angle) geometry because it allows more material of the thin film to be sampled and provides information about the crystallinity of the sample surface with reduced interference from the substrate.

The grazing incidence X-ray diffraction (GIXRD) geometry has been used to characterize monolayer films [178]. With the incident angle small enough, the X-ray can penetrate $\sim 10 - 20nm$ into the specimen. The exit angle of the diffracted X-ray is also small and structural information is obtained about (hkl) planes perpendicular to the specimen surface. However if

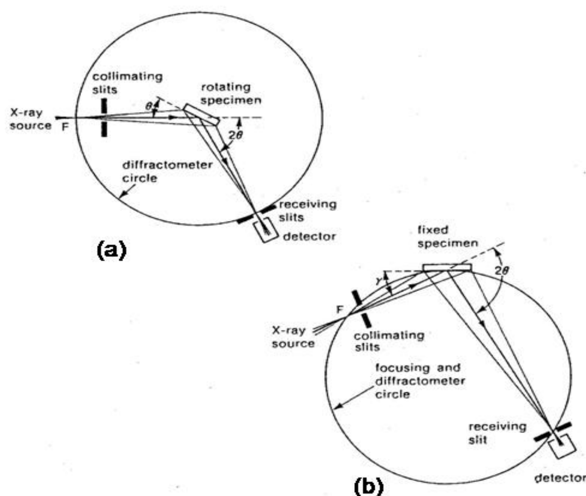

Figure 3.15: (a) Bragg-Brentano diffraction geometry for thin films (b) Seemann-Bohlin diffraction geometry [177]

the incidence angle is too small, the radiation will not penetrate the sample, but will result instead in evanescent wave (due to total external reflection) at the surface [179].

The Seemann-Bohlin diffraction geometry (figure 3.15b)is suitable for thin film XRD. It provides good sensitivity for thin films, due to parafocusing and large diffracting volume because the angle of incidence γ is small ($\sim 5-10°$), and X-ray path length in the film is large because it is proportional to $1/\sin\gamma$. The angle of incidence γ is normally fixed and the angle between the diffracting planes and the incident X-ray moves through 2θ as the detector sweeps the angle. The geometry is most useful for polycrystalline films that have random or nearly random crystallite orientation [177, 180].

Diffraction patterns from amorphous materials do not have sharp peaks that characterize crystalline materials, but rather broad features qualitatively indicate amorphous material. Quantitative analysis of XRD data from amorphous materials is complicated, but can provide important information on local atomic structure (short range order), including bond lengths, number of neighbors and the extent of atomic correlations [177].

3.3 Mechanical Analysis

3.3.1 Introduction

Mechanical reliability for composite contact metallizations is an essential part of metallization evaluation during and after device fabrication. The primary concern is adhesion between layers in the multilayer structure that constitutes the composite contact. Monitoring the degradation of adhesion properties is important, and long-term reliability testing is generally performed under temperature-humidity cycling.

Wirebond pull and shear (push) testing and brazing for die attach are normally used to study adhesion properties. Vertical pull force and horizontal push force on bond points can cause separation within the metallization structure, since the weakest interface in the multilayer structure will give way first. The pull or push strength at which this failure occurs can be measured experimentally. The bond can be either a ball or a wedge depending on the type of wire bonder used. The bonding scheme is a wire loop terminating at two bond points seperated by a horizontal distance (d) (figure 3.16). The length of the loop and the bond-to-bond distance determine the angle of pull on the bond points. A simple analysis of the force distribution is shown below.

Wire Bonding and Die Attach [181]

Bonding between two dissimilar metals (e.g. Au-Al) leads to the formation of intermetallics. The property of the intermetallic formed (e.g brittleness) will mostly determine the strength of the bond. Excessive formation of intermetallics is manifested in the form of an increase in resistance, intermittent conduction, or an open circuit. Intermetallic formation is normally accompanied by Kirkendall voiding, leading to the brittle fracture of the wire bond. Because dissimilar metals diffuse into each other at different rates, an excess of vacancies is formed on the side of the fast diffusing metal. This vacancies coalesce into voids, known as Kirkendall voids, which act as a stress concentrator.

Wirebonding with same metal (e.g., Au-Au, Al-Al) elliminates the possibility of interface corrosion, intermetallic formation, Kirkendall voiding and other bond degrading conditions. However, the cost of a Au-Au system, for example, may be a draw back when considering monometallic wire bonding, apart from additional and/or difficult processing steps that may be involved.

Wirebond pull testing

An applied pull force F on the hook pulling on the loop and the tension on the wire bond T are related as shown in figure 3.16.

$$F = 2T\sin\theta \qquad \Rightarrow \qquad T = \frac{F}{2\sin\theta} \tag{3.77}$$

If the bond-to-bond distance is d, and the length of wire loop between the bond points is l, we define a fractional distance between these lengths as, $\eta = \frac{l-d}{l}$ i.e. $1-\eta = \frac{d}{l}$

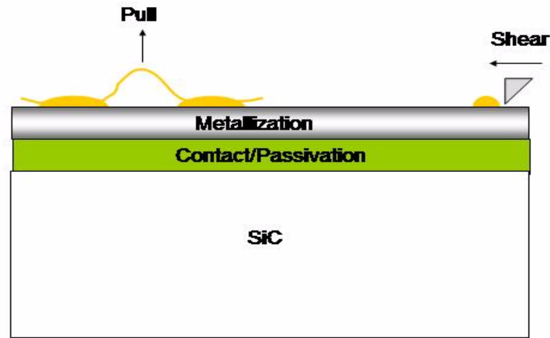

Figure 3.16: Wire bond pull and shear testing

$$\sin\theta = \frac{2h}{l} \qquad and \qquad (l/2)^2 = (d/2)^2 + h^2$$
$$\sin\theta = \frac{2h}{l} = \sqrt{2\eta - \eta^2} \qquad \eta < 1 \tag{3.78}$$

Therefore,

$$T = \frac{F}{2\sqrt{2\eta - \eta^2}} \tag{3.79}$$

This equation implies measuring d and l or the difference between them and the pull force F is enough to estimate the pull strength on the bond.

Wirebond shear testing

An horizontal force can be used to push on the wire bond to its shear point. The shear force is proportional to the bond contact area. Part of figure 3.16 illustrates the bond shear testing structure. Die attach shear testing is similar to the bond shear testing (figure 3.17). The difference is that a larger area chip is brazed to a ceramic carrier. Between the ceramic and the

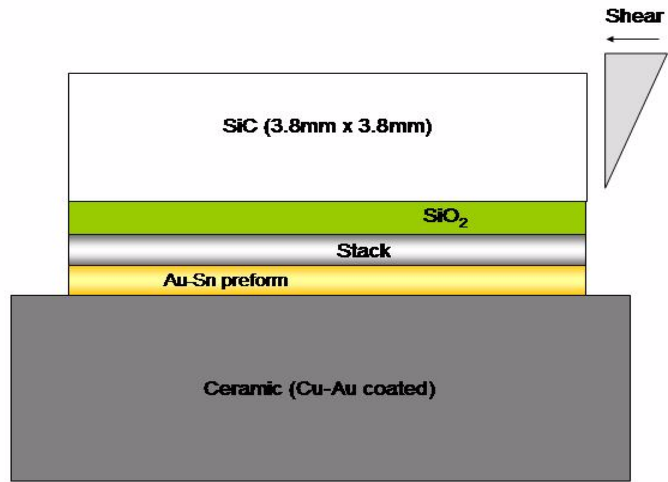

Figure 3.17: Chip brazed shear testing

chip is a preform used to solder or barze the ceramic and the chip together. The chip is then push horizontally while the ceramic substrate is held in place.

CHAPTER 4

EXPERIMENTAL PROCEDURES

4.1 Standard Procedures

Research grade 4H-SiC for this work was purchased from Cree, Inc. The profiles of the $2''$ diameter wafers and their intended uses are listed in the table 4.1. The wafers were diced into 5mm$\times$5mm pieces for fabrication.

4.1.1 Sample Cleaning

Substrate cleaning is required to remove surface particulates as well as traces of organic, ionic and heavy metallic impurities. The two stage substrate cleaning process includes an organic clean and RCA clean.

4H-SiC profile (cm^{-3})	**Purpose**
N sub/$0.7\mu m$ epi $p(7 \times 10^{18})$/ $0.3\mu m$ epi $p^+(3 \times 10^{19})$	p-ohmic contact
N sub/$0.7\mu m$ epi $p(7 \times 10^{18})$/ $0.3\mu m$ epi $p^+(3 \times 10^{19})$/impl. $p^+(1 \times 10^{21})$	p-ohmic contact
P sub/epi $n^+(5 \times 10^{19})$	n-ohmic contact
N^+ sub/epi $n^-(9.8 \times 10^{15})$	n-schottky contact
Semi-Insulating SiC	Metal sheet resistance measurements
Low quality SiC	Samples for RBS, AES and XPS analysis

Table 4.1: Profile of 4H-SiC purchased from Cree research Inc.

Organic clean

The purpose of this cleaning procedure is to remove organic and oily contaminants on the substrate surface. The samples were:

- immersed in acetone and agitated in an ultrasonic bath for 5mins.
- immersed in trichloroethylene and agitated in an ultrasonic bath for 5mins.
- immersed in acetone and agitated in an ultrasonic bath for 5mins.
- immersed in methanol and agitated in an ultrasonic bath for 5mins.
- immersed in fresh mehtanol and agitated in an ultrasonic bath for 5mins.
- rinsed in de-ionized water (DI water) for 3mins.
- immmersed in buffer oxide etch (BOE) for 1min.
- rinsed in DI water for 2mins and dried with N_2 gas.

RCA clean (Radio Corporation of America)

The purpose of this cleaning procedure was to remove ionic and heavy metal contaminants on the samples. The samples were:

- immersed in a 1:1 (solution) of H_2O_2:H_2SO_4 for 15mins. The mixture of H_2O_2 and H_2SO_4 is exothermic.
- rinsed in DI water for 2mins.
- immersed in a 20:6:6 mixture of DI H_2O:H_2O_2:NH_4OH warmed on hot plate to boil gently for 15mins.

- rinsed in DI water for 2mins.

- immersed in a 20:6:6 mixture of DI H_2O:H_2O_2:HCl warmed on hot plate to boil gently for 15mins.

- rinsed in DI water for 2mins.

- immmersed in a buffered oxide etch (BOE) for 2mins.

- rinsed in DI water for 3mins and dried with N_2 gas.

These cleaning procedures are the same irrespective of the type of device that is being fabricated.

4.1.2 Photolithography

Photolithography is the process by which a mask aligner is used to transfer features on a mask onto a sample. A Karl Suss MJB3 UV400 mask aligner was used for this work. Square TLM mask features and circular mask features for diodes and MOS structures are shown in figure 4.1. The light source on the mask aligner is Karl Suss UV lamp with an output power of 160W. The mask aligner is manually controlled and $2 - 3\mu m$ features can be aligned with the help of optical microscope having magnifications of 5, 10 and 20.

The 5mm×5mm sample was held on a 3″ Si wafer, and AZ 5213-EIR photoresist (positive photoresist) was spun onto the sample for 30s at a rotor speed of 4000rpm. The sample was then soft baked on a hot plate at $110°C$ for about 90s to dry the photoresist and make it more photosensitive. Under baking or over baking can reduce or destroy the sensitivity of the photoresist.

The sample on 3″ Si wafer was mounted on the mask aligner, and X, Y, and θ adjustment of the sample table was made to bring the sample into alignment with the mask features. By

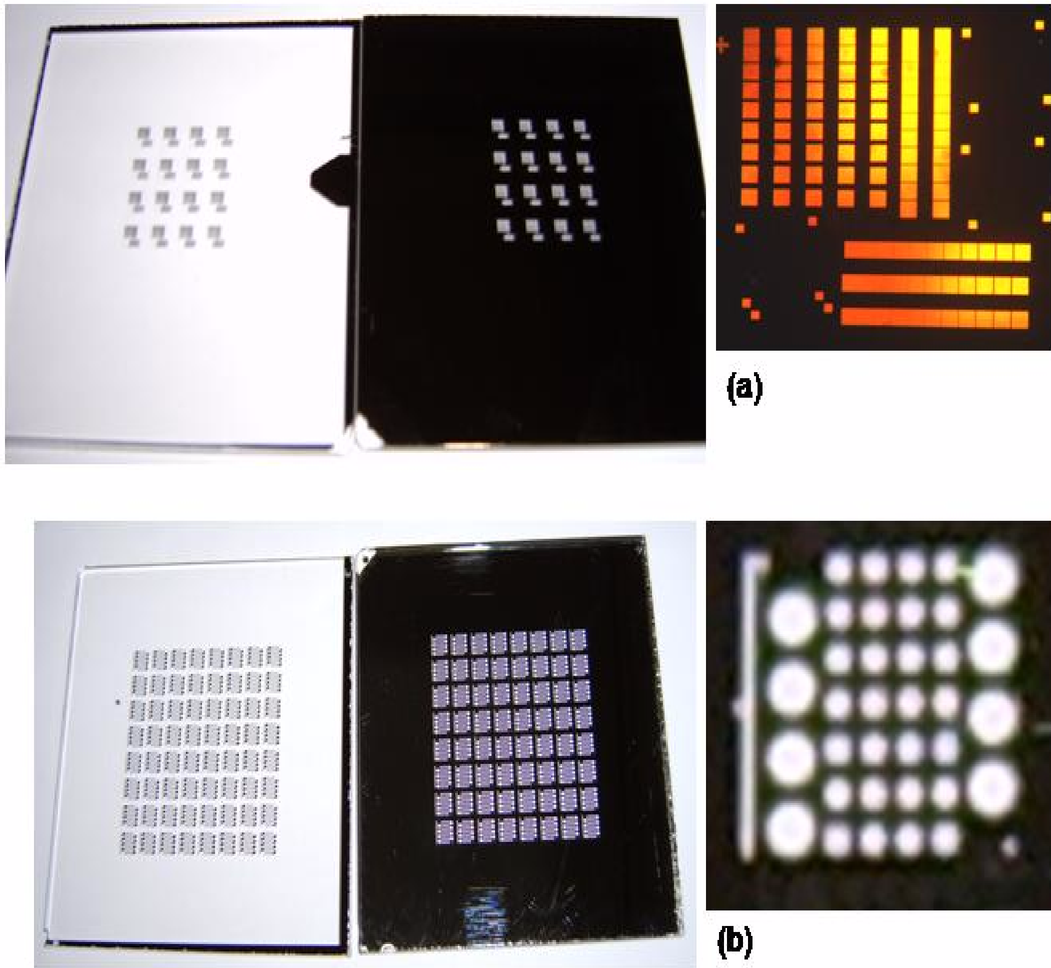

Figure 4.1: (a) TLM masks (b) Diode/MOS Mask

exposing the sample to UV light through the mask, the features on the mask were transfered on the sample. UV exposures was made for about 25s.

Following exposure, samples were developed in a mixture of DI water and Microposit 351 developer or AZ 400K developer. The volume ratio DI water to developer was 4:1. The samples were immersed in this diluted developer for few seconds. During the time of development, the part of the photoresist on the sample exposed to UV light was washed off, and the sample was subsequently rinsed in DI water and dried in N_2 gas. Complete development of the sample was confirmed under a microsope.

Reversing the effect of UV light exposure on photoresist, keeping the photoresist exposed to UV light stays on the sample after development while removing the part not exposed can be achieved by using a negative photoresist or simply reversing the positive photoresist as follows. Spin-on the positive photoresist and soft bake it for 30s, then expose the sample to UV light through the mask for 25s. Then bake the sample after exposure for 60-90s at $110°C$. Expose the whole sample to UV light through a clear mask or no mask for 60s. Develop the sample in 4:1 DI water and developer yeild the same result as obtained using a negative photoresist.

4.1.3 Sputter-deposition

All metals in this study were sputter-deposited in an Argon plasma. The sputter-system is a high vacuum system. It has three $2''$ diameter Polaris magnetron sputtering sources or guns. Three different targets can be sputtered consecutively without breaking vacuum in this system. A sputter target can operate at a maximum dc power of 1000W or maximum RF power of 600W, and cathodes potential can be between 200-1500V. The sputter guns are cooled by $13°C$ water circulating beneath the cathode surface. The deposition rate is limited by the type and quality of target materials. Large area, uniform films can be obtained if the samples were located at height

$4''$ or so from the target. Figure 4.2 shows the sputter-system used for this study. The metals or metallic alloys to be sputtered were mounted on the magnetrons, and sprayed cylindrical glass chimneys were placed on the gun to confine and focus the sputtered materials. Samples on $3''$ Si wafers were mounted on a plain disk carrier or a disk carrier with capability of heating the sample during sputter-deposition. The system was pumped down for about 2 hours to a base pressure of about 5×10^{-7}torr.

To start sputter-deposition, cooling water circulation to the gun to be used was checked. Argon gas flow was set on an MKS 247 mass flow controller at 106.4sccm for most of the deposition in this work. At this flow rate, the chamber pressure rises to about 5mtorr but with a butterfly valve of the turbo-pump slightly closed, the pressure rises to 20mtorr for the depositions. Power was turned-on and the dc voltage to the cathode incresed until an Ar plasma was generated and the pre-determined sputter current attained and stabilized. Off-sample, pre-sputtering was carried out for few minutes, then the sample was rotated to a position over the sputter-gun, and sputtering onto the sample carried out for as long as required to yield a desired thickness. For every target, calibration of the sputtering rate must have been done a priori. A Tecnor profilometer is used for a quick thickness measurement, following deposition.

4.1.4 Annealing System

The high temperature annealing system used for ohmic contact anneals is also used for implant activation annealing. Temperatures up to $1600 - 1700°C$ can easily be attained with this furnace. Heating elements in the annealing system are two carbon strips, and the current through the strips is controlled manually with a variac while temperature is measured with an Omega pyrometer focused on the carbon strip close to the samples. The samples were held on

Figure 4.2: Sputter-deposition system with disk sample holders having heating capability

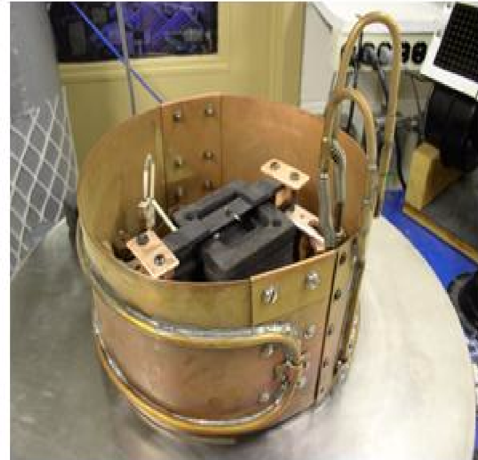

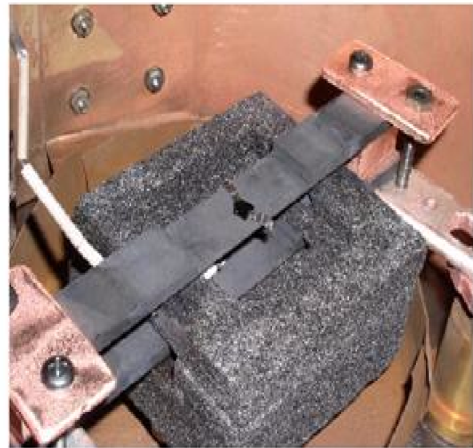

Figure 4.3: Annealing system with enlarged carbon strips showing sample

the carbon strip with tungsten clips. The annealing chamber is pumped to a vacuum of about 1×10^{-7}torr for vacuum annealing.

Power is turned-on when the chamber pressure is about 1×10^{-7}torr, and current through the carbon strips increased slowly. The annealing temperature ($900 - 1000°C$) is reached in 2-3mins with a variac setting of 40-45%. Most of the ohmic contact anneals were carried out for 1-2mins in vacuum. During annealing, the chamber pressure rises to about 2×10^{-6}torr. It is also possible to anneal samples in Ar or N_2 ambients with this system. After annealing the variac is set to zero, and the power switched off. The annealing chamber temperature drops to room temperature in vacuum in about 3 hours. Samples were removed in Ar at atmospheric pressure.

4.2 Device Fabrication and Measurements

4.2.1 Ohmic Contact Fabrication

Ohmic contact to p^+-4H-SiC

Ohmic contacts were fabricated on implanted and epitaxial p^+-4H-SiC. The profiles of these materials are listed in table 4.1. The sequence for ohmic contact fabrication is shown in figure 4.4. An aluminum-titanium alloy (Al-Ti 70-30 wt%) and nickel (Ni-V 93-7wt%) were sputter-deposited. Contact anneals for the Al-Ti contact on the p^+-implanted and p^+-epilayers was carried out at $1000°C$ for 2 minutes in vacuum. These conditions were the optimum for low resistance contacts [11]. Nickel contacts were annealed on p^+-implanted and p^+-epilayer SiC at $900°C$ for 1 minute in vacuum.

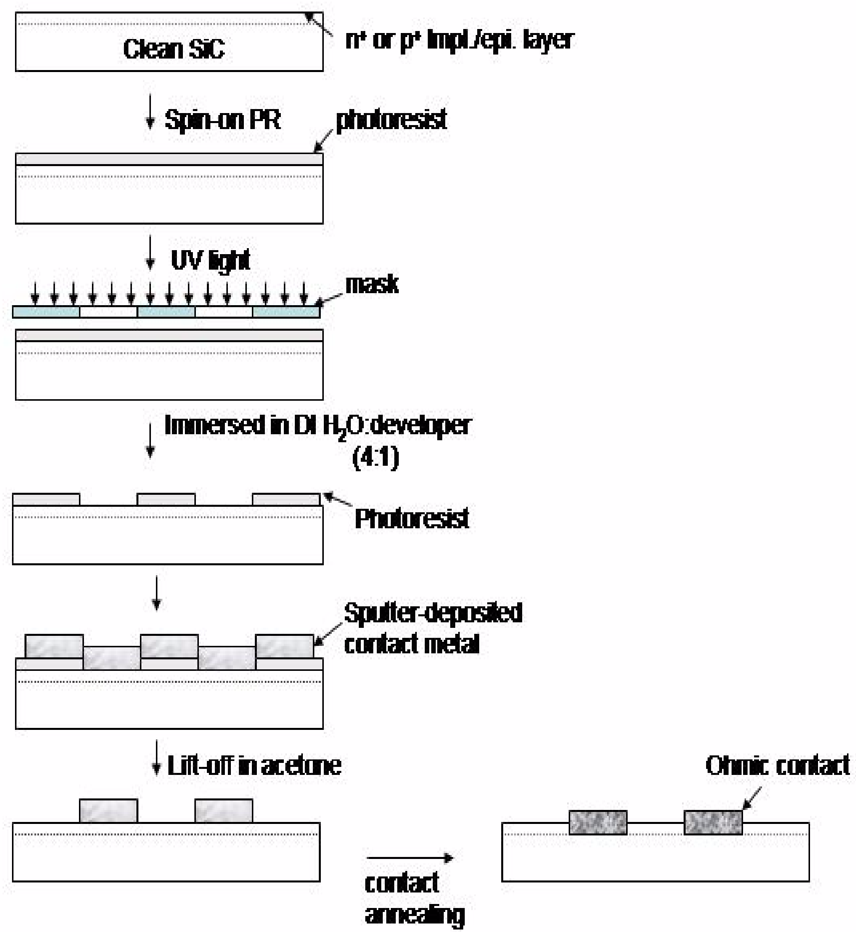

Figure 4.4: Sequence for ohmic contact fabrication

Ohmic contact to n^+-4H-SiC

Ohmic contacts were fabricated on epitaxial n^+-4H-SiC (see table 4.1). The fabrication sequence is the same as for p-ohmic contacts. A nickel-chromium alloy (Ni-Cr 80-20 wt%) and nickel (Ni-V 93-7wt%) were deposited. Contact anneals for Ni-Cr contacts on n^+-epilayers were carried out at $1000°C$ for 2 minutes in vacuum. Nickel contacts were annealed on n^+-epilayers at $950°C$ for 2 minutes in vacuum [5].

4.2.2 Schottky Contact Fabrication

Schottky contacts were fabricated on $10\mu m$ n^--epilayers on n^+-4H-SiC substrates using the sequence shown in figure 4.5. The samples were cleaned using standard procedures after which a 30nm thermal oxide was grown at $1150°C$ in dry O_2 for about 4 hours. These oxide layers were used as either sacrificial or passivating layers. For Schottky diodes, the sacrificial oxide was striped just before photolithography that defined the Schottky diode feaures. After photolithography, nickel silicide was sputtered, and the samples subsequently sintered at $500°C$ for 24 hours.

A second set of Schottky diodes was also fabricated. The back side oxide (oxide on the n^+ side) of the sample was etched in buffer oxide (BOE) for about 1 minute while the front side oxide was protected with crystal bond. Nickel ohmic contacts were fabricated on the back side by sputter-deposition and high temperature annealing at $950°C$ for 2 minutes. After the fabrication of back contact, the Schottky contacts were formed by nickel silicide (Ni_2Si) sputter deposition through windows opened in the front side oxide layer. The contact thickness was about $1000\AA$. The Schottky diodes were formed with passivating SiO_2 surrounding each device. This set of samples was not sintered.

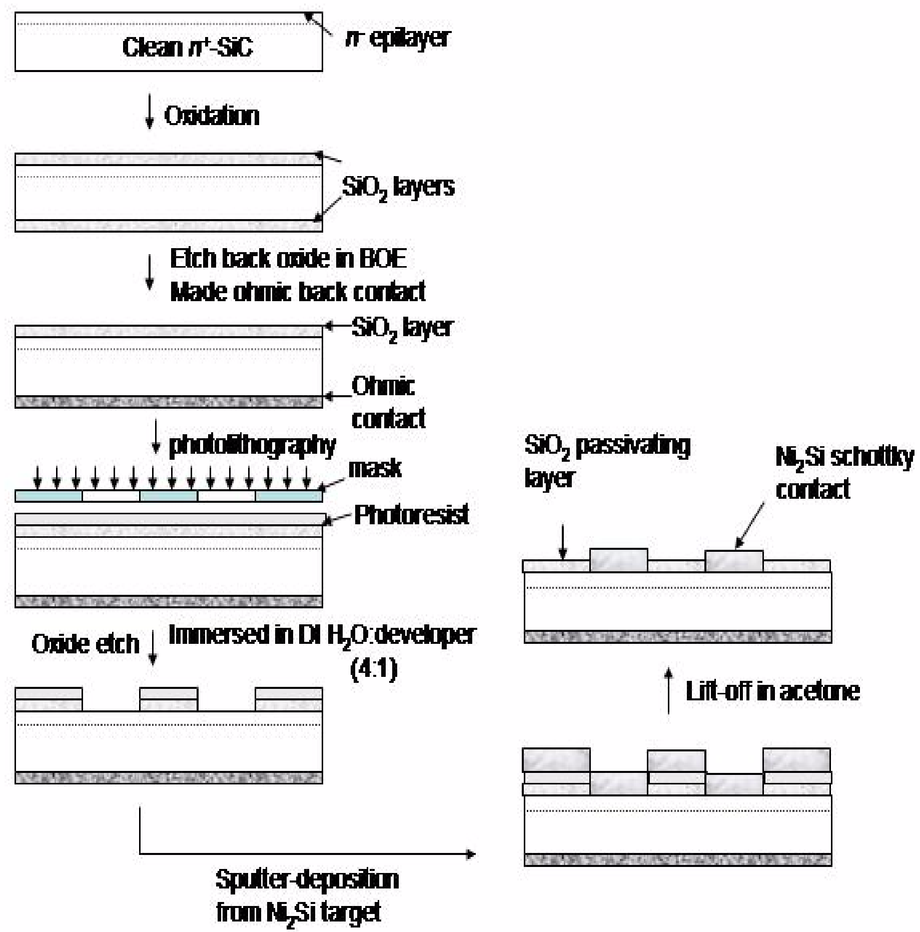

Figure 4.5: Sequence for Schottky contact fabication

4.2.3 Protective Stack Fabrication and Device Mesurements

Devices operating at $350°C$ in air have to be protected from oxidation and cap layer/contact layer inter-diffusion. The protective metallization fabrication sequence is shown in figure 4.6. Tantalum silicide ($TaSi_2$) was sputter-deposited on ohmic and Schottky contacts as diffusion/oxidation barrier. About $1500\mathring{A}$ of tantalum silicide was sputter-deposited in Ar and Ar/N_2 gas mixtures. Then a $1000\mathring{A}$ platinum layer was deposited followed by cap layers of Au ($1200\mathring{A}$) or Au/Sn/Au ($500\mathring{A}$/$25\mathring{A}$/$700\mathring{A}$). Cross-section of ohmic and Schottky contacts with protective stacks are shown in figure 4.7.

During processing, it was observed that sputtering Pt at $250°C$ improved the adhesion with the Ta-Si-N layer considerably. Good adhesion is essential for wire bonding and die attach. The metallization sequence in figure 4.6 was subsequently modified to allow sputter-deposition of Pt at $250°C$. Since photoresist starts to carbonize at this temperature etch back of Pt in an acid solution as well as lift-off with Mo was used. Figure 4.8 shows the modified sequence.

Pt etch back

After sputter-deposition and lift-off of Ta-Si-N layer, the samples were loaded back into the sputter system on the sample holder and Pt was depostited at $250°C$. Photolithography, to define the contact areas, was conducted with the thick photoresist, AZ P4620, UV light exposure time of 1 minute. The photoresist over the defined contact regions was baked for about 7 minutes at $110°C$. The baking reduces undercutting of the Pt during acid etch back. The etchant for Pt is $1HNO_3$/$3HCl$/$4H_2O$ at $95°C$. Etching $1000\mathring{A}$ of Pt was completed in about 6 minutes. The etching process is more effective for diodes/MOS features where the separation between adjacent devices is large. It is a little difficult to etch the fine features in a TLM pattern, especially the

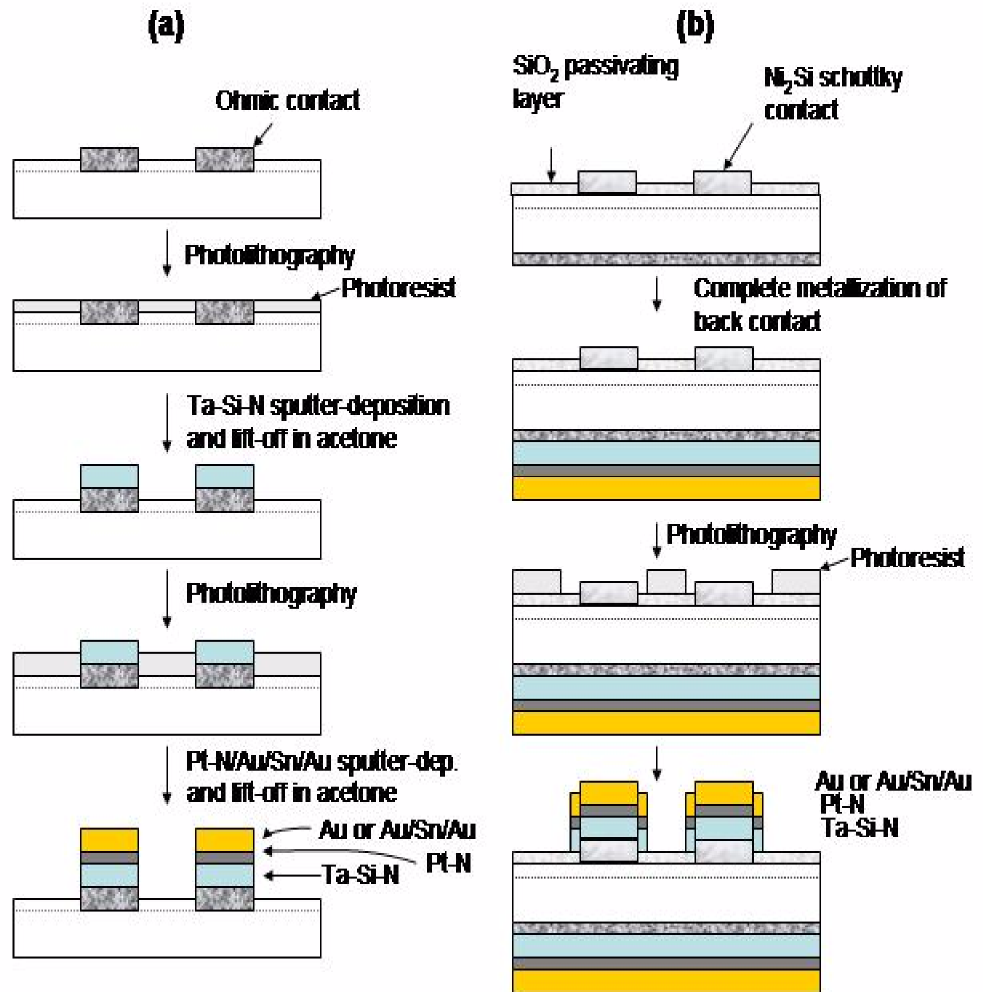

Figure 4.6: Sequence for protective metallization on (a) ohmic contact (b) Schottky contact

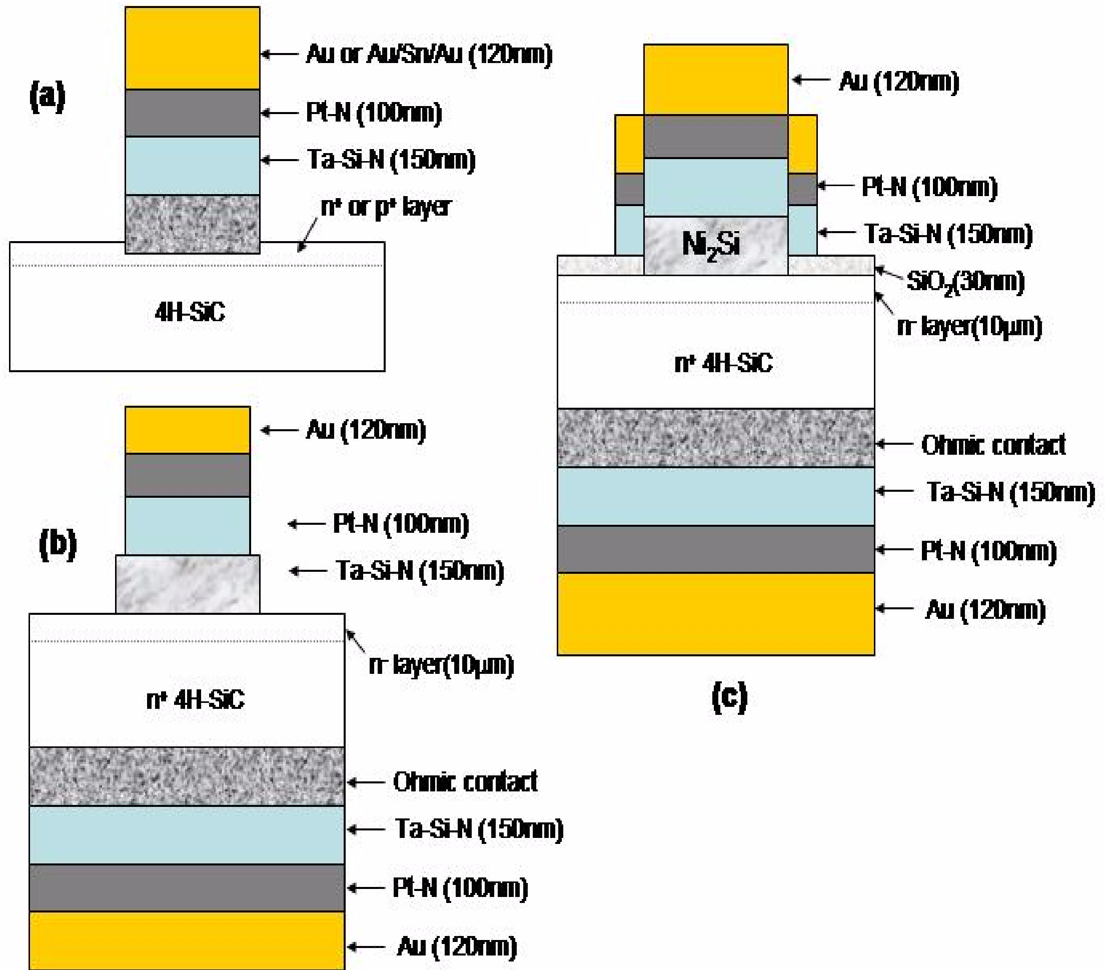

Figure 4.7: Device cross-section of (a) ohmic (b) initial Schottky (c) new Schottky contacts

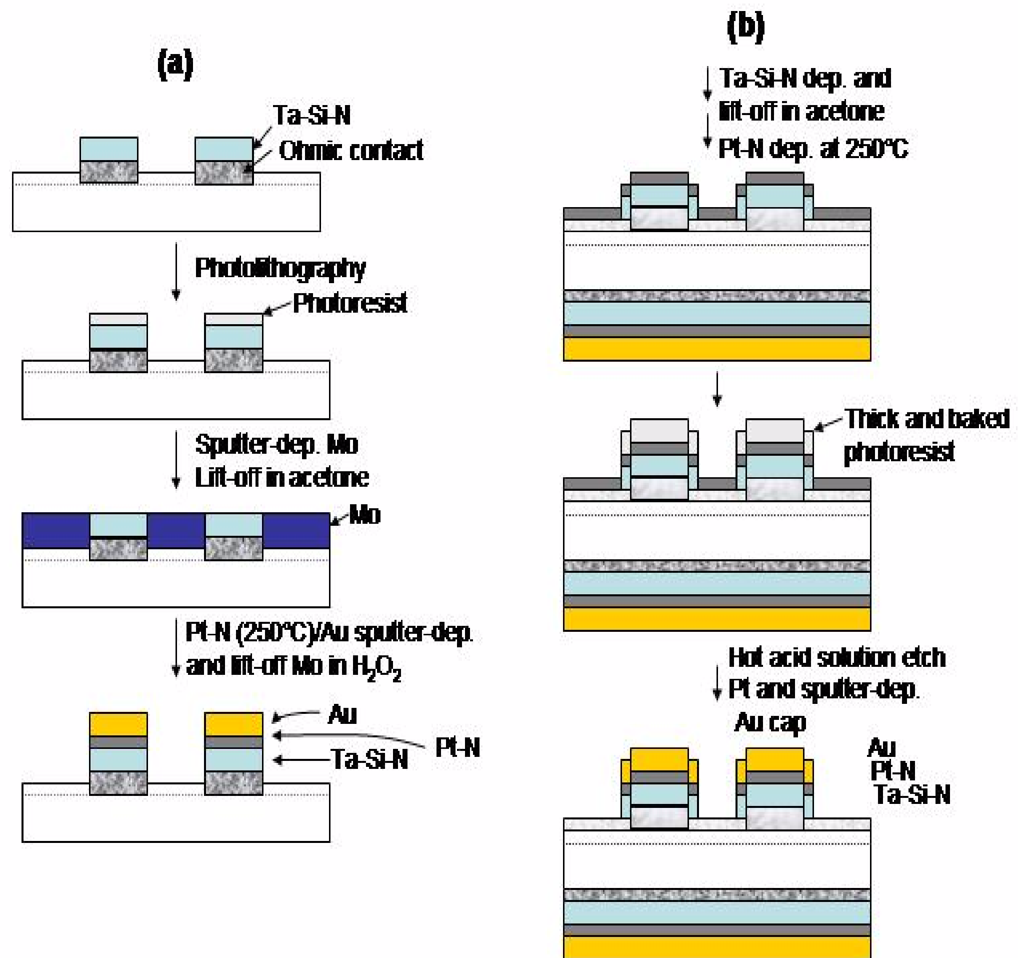

Figure 4.8: Modified sequence for protective metallization (a) ohmic contact with Mo lift-off (b) Schotky contact with Pt etch-back

last two smallest gaps. To be able to etch the fine features ($< 4\mu m$ gaps) effectively, the samples stays longer in the etchant and significant undercutting on lager features will occur.

Thin Au cap layers (about $1200\AA$) were deposited on samples with contact pads re-defined by photolithography. The Au cap layer was then lifted-off everywhere except on the contact pads.

Pt lift-off with Mo

To avoid etching samples in acid, molybdenum was used to lift-off Pt. After Ta-Si-N was deposited and lifted-off in acetone, normal photolithography was carried out to leave photoresist on the contact pads after development. Molybdenum was then deposited on the samples, and the Mo on photoresist above the contact pads was lifted-off in acetone, leaving Mo everywhere except on the contact pads. As a result, Mo serves the function of photoresist if the Pt is not sputter-deposited at $250°C$. At this temperature Mo does not diffuse into SiC or the metallization on the samples. The lift-off of Mo with the Pt layer on top of it is done in H_2O_2 in about 10 minutes for a Mo of about $3000\AA$.

A thin Au cap layer (about $1200\AA$) can be deposited over the Pt before lifting-off the Mo, so that a single process defines the Pt and Au cap layers. For thick Au (about $6000\AA$) needed for wire bonding, another photolithography process may be necessary. For higher Au thicknesses, photoresist spin-on may be repeated 3 or more times to accumulate thicker AZ 5214 photoresist on the sample for easier lift-off in acetone. Alternatively, Au can be etched back.

4.2.4 Wirebonding and Chip Brazing

Large area samples were fabricated using low quality SiC for wire bonding (1.8 × 1.8cm sample size) and for die attach (0.5 × 0.5cm sample size) testing. The samples were cleaned

using standard procedures. For indirect wire bonding, adhesion of the protective stack to SiO_2 was investigated. This structure was also brazed on ceramic carriers. Cleaned SiC was first oxidized, then Ta-Si-N, hot Pt and thick Au layers were sputter-deposited onto the oxide layer.

Adhesion of the protective stack to ohmic contacts and Schottky contacts for the case of direct bonding was also investigated. The protective metallization and cap layers were deposited without breaking the vacuum. The top Au cap layer for wire bonding was about $6000\AA$ thick.

The wire bonder used is a computer controlled ultrasonic model. This equipment is located in the Center for Advanced Vehicle Electronics (CAVE) in the department of Electrical and Computer Engineering. The bonder is capable of using wire diameters in the range $127-508\mu m$. Parameters like bond force, bond power, bond time, loop value, hop distance and so on were preset on the system. This bonder operates by pressing the bonding wire thermosonically onto the sample cap layer and thus forming a wedge bond (not a ball bond) on the sample. Careful selection of the input parameters leads to good wirebonding. For this work $254\mu m$ (10mil) diameter Au wire was used. The Au wire was wedged thermosonically at about $230°C$ to the $6000\AA$ Au cap layer.

Chips were brazed to a direct-bond copper (DBCu) substrate which is simply a Cu-coated ceramic (Al_2O_3) substrate with Ni film on the Cu and a and top thin Au film on the Ni. DBCu substrates were purchased from Stellar industries, then plated with thick Au (few microns) because the flash Au layer is too thin for brazing. The substrates was diced slightly bigger than the SiC chips to allow room for shear testing. The brazing of the chip to the substrate was carried out with the help of a Au-Sn alloy (80-20 wt%) preform. This preform was selected because a Au-Sn alloy eutetic occurs at $< 320°C$ which is very much lower than the melting point of Au. The preform was sandwiched between the chip and the substrate, kept under a load and place in the brazing machine. The brazing was carried out at a pressure of about 10^{-5}torr. The braze

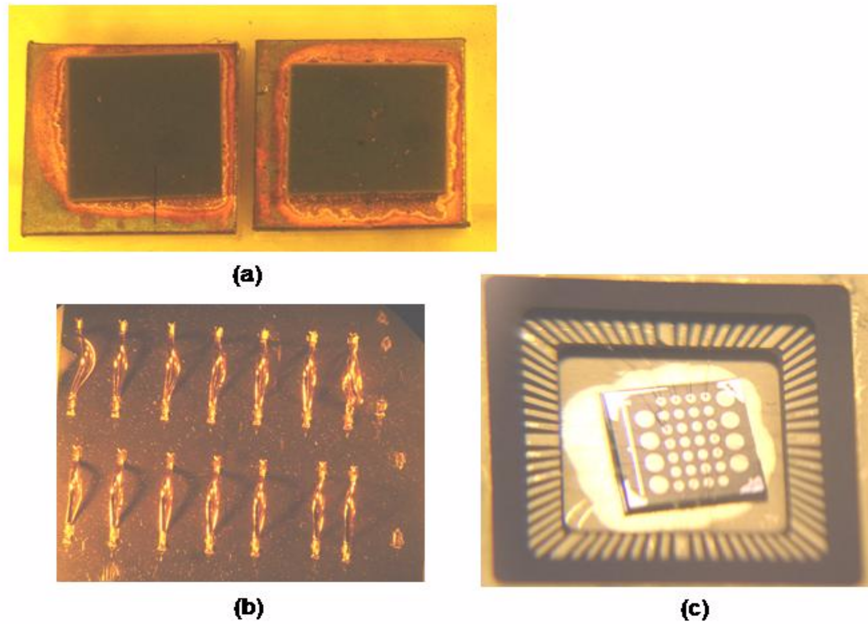

Figure 4.9: (a) Large area wire bonded sample for pull and bond shaer testing (b) Chip brazed sample for die shear testing

temperature profile ramped from room temperature to $300°C$ in 5 minutes, and then from $300°C$ to $400°C$ over 3 hours.

Figure 4.9 shows brazed and wirebonded samples for shear and pull testing. For both, a Dage micro-mechanical test system was used. The Dage-PC2400 can apply a 5kg force for bond shear testing, up to 100kg for die shear testing and up to 10kg for wire-pull testing.

4.2.5 Thermal Aging of Samples

All the samples fabricated were first characterized physically, electrically and mechanically. These pre-aging measurements are referred to as 0-hr data. The samples were then thermally aged at $350°C$ in air using two furnaces - an old furnace operated at $350°C$ 24 hours a day, and a new programmable box furnace with a temperature cycling capability. This furnace was

programmed to cycle from $25°C$ to $350°C$ in 1 hour, remain at $350°$ for 8 hours, then cycle back to $25°C$ in 1 hour, remain at $25°C$ for another 2 hour and then repeat the cycle. At intervals (100, 500, 1000hr, etc.) the samples were removed from the furnaces and characterized again. This process continued for thousands of hours of annealing in air at $350°C$.

4.2.6 Measurements

The set-up for TLM measurements is shown in figure 4.10. The total contact-to- contact resistance was measured by passing a 1mA current between adjacent TLM pads using a Keithley 220 programmable current source. The potential (millivolts) developed between the pads was measured with a Hewlett Packard 3478A multimeter. Thus, what was measured directly by the multimeter is the total contact-to-contact resistance as a function of the inter-contact spacing. The contact resistance, specific contact resistance and semiconductor sheet resistance were then obtained from a TLM analysis. Samples without and with protective metallizations were measured. TLM measurements were also performed for some protected stacks as a function of temperture up to $350°C$.

Current-voltage (I-V) and Capacitance-voltage (C-V) measurements were carried out for the Schottky diodes. The set-ups for the I-V and C-V measurements are shown in figure 4.11. I-V measurements up to 2V forward bias and reverse bias out to -300V were performed.

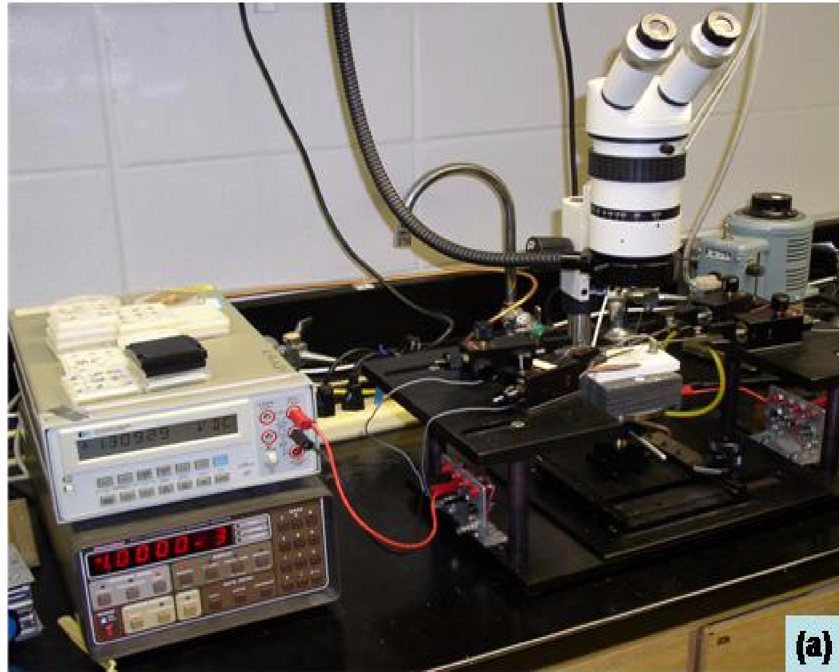

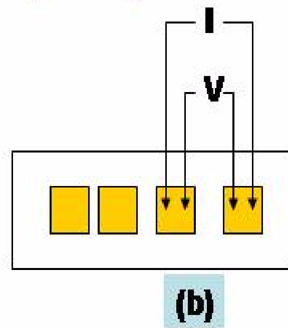

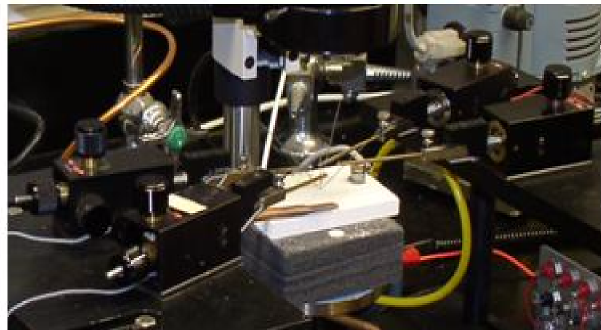

Figure 4.10: (a) TLM measurement set-up (b) measurement configuration

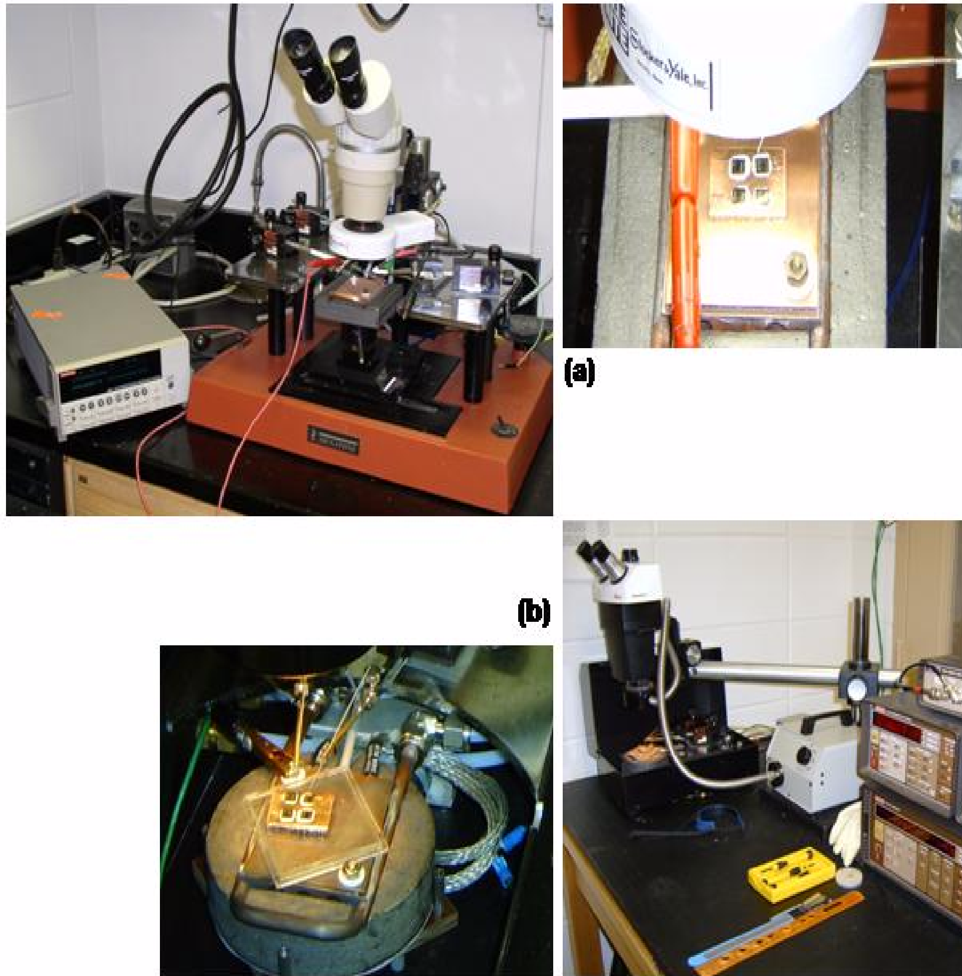

Figure 4.11: (a) Current-Voltage measurement set-up (b) Capacitance-Voltage measurement set-up

CHAPTER 5

RESULTS AND DISCUSSION

5.1 The Choice of Barrier Layer Material

5.1.1 Silicide Barrier Layer

In support of very large or ultra large scale integrated (VLSI or ULSI) microelectronics, metal-silicon-nitrogen (M-Si-N) amorphous films have been studied as candidates for diffusion barrier layers between interconnect metals (Cu, Al) and silicon [112, 106, 136].

In this study, four silicide materials ($MoSi_2$, WSi_2, $TaSi_2$ and Ta_5Si_3) were considered for barrier layers on SiC devices for high temperature applications. The effeciveness of $TaSi_2$, WSi_2 and $MoSi_2$ as diffusion/oxidation barrier layers at $350°C$ in air was investigated by sputter-depositing the silicides on SiC. Platinum cap layers were deposited. RBS data of these samples as a function of annealing time in air at $350°C$ are shown in figure 5.1. Based on the RBS spectra the following conclusions can be made.

1. Platinum permitted oxygen to diffuse in air at $350°C$.
2. Mo-Si and W-Si films under Pt cap layer were oxidized when the samples were annealing in air. Mo-Si and W-Si layers were almost totally oxidized after 120 hours and 780 hours of annealing in air, respectively.
3. Significant mixing of W-Si with Pt cap layer was observed.
4. The Ta-Si layer showed high resistance to oxidation and little mixing with the Pt over-layer.

Based on these results, Mo-Si and W-Si were droped in preference to Ta-Si as candidate for the diffusion/oxidation barrier.

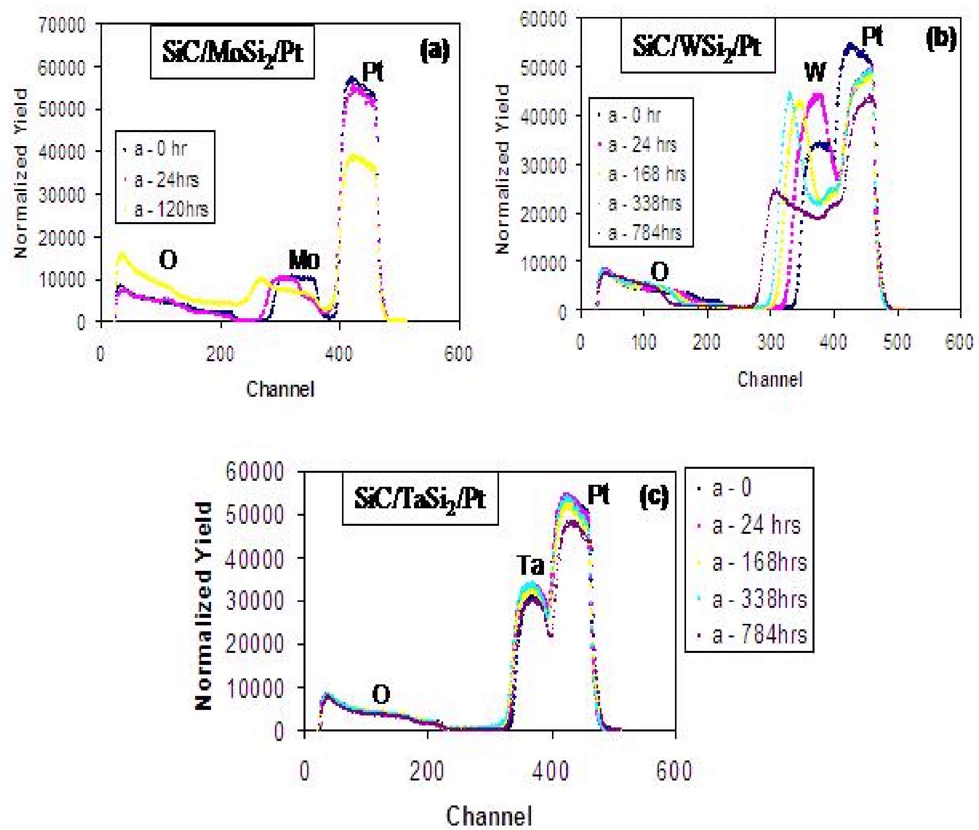

Figure 5.1: RBS spectra of (a) SiC/Mo-Si/Pt (b) SiC/W-Si/Pt and (c) SiC/Ta-Si/Pt

$TaSi_2$ and Ta_5Si_3

The choice between $TaSi_2$ and Ta_5Si_3 for the deposition of Ta-Si-N was made in favor of $TaSi_2$. Figure 5.2(a) shows that nitrogen was actually incorporated in the tantalum silicide films. The amount of nitrogen incorporated increases with increasing percentage of nitrogen flow during sputter-deposition. Van der Pauw sheet resistivity measurements [figure 5.2(b)] showed that above 2% nitrogen flow the resistivity of the Ta-Si-N layer obtained from the Ta_5Si_3 target increses rapidly and is significantly higher than the resistivity of Ta-Si-N layer deposited using $TaSi_2$. Figure 5.2(c) is the plot of nitrogen content in the Ta-Si-N layer as a function of nitrogen flow percentage. Films deposited from Ta_5Si_3 contain more nitrogen and hence are more resistive as indicated by the van der Pauw resistivity measurements. Nitrogen atomic percentages in the films were computed using fit to RBS spectra taken with and without nitrogen in the $TaSi_2$ films. The atomic ratios used in the fits were Ta:Si:N = 1:1.5:x, and the nitrogen atomic fraction was computed as x/(1+1.5+x). The sheet resistance of Ta-Si-N deposited on semi-insulating SiC using $TaSi_2$ is shown in figure 5.3(a) as a function of nitrogen content and time of annealing in air at $350°C$. The sheet resistance increases with increasing nitrogen content in the film. For any particular amount of nitrogen however, the sheet resistance is very stable with anneal time up to 5000 hours. However, it became more difficult to measure the sheet resistance after 2500 hours because of a thin surface oxide layer as indicated by a gradual color change of the surface from metallic gray to light gold. Figures 5.3(b) and (c) show the RBS spectra used to monitor the oxidation kinetics of the Ta-Si-N films. In these spectra, oxygen incorporated during film deposition was observed throughout the films; however, oxygen in the surface oxide layer increases with annealing time.

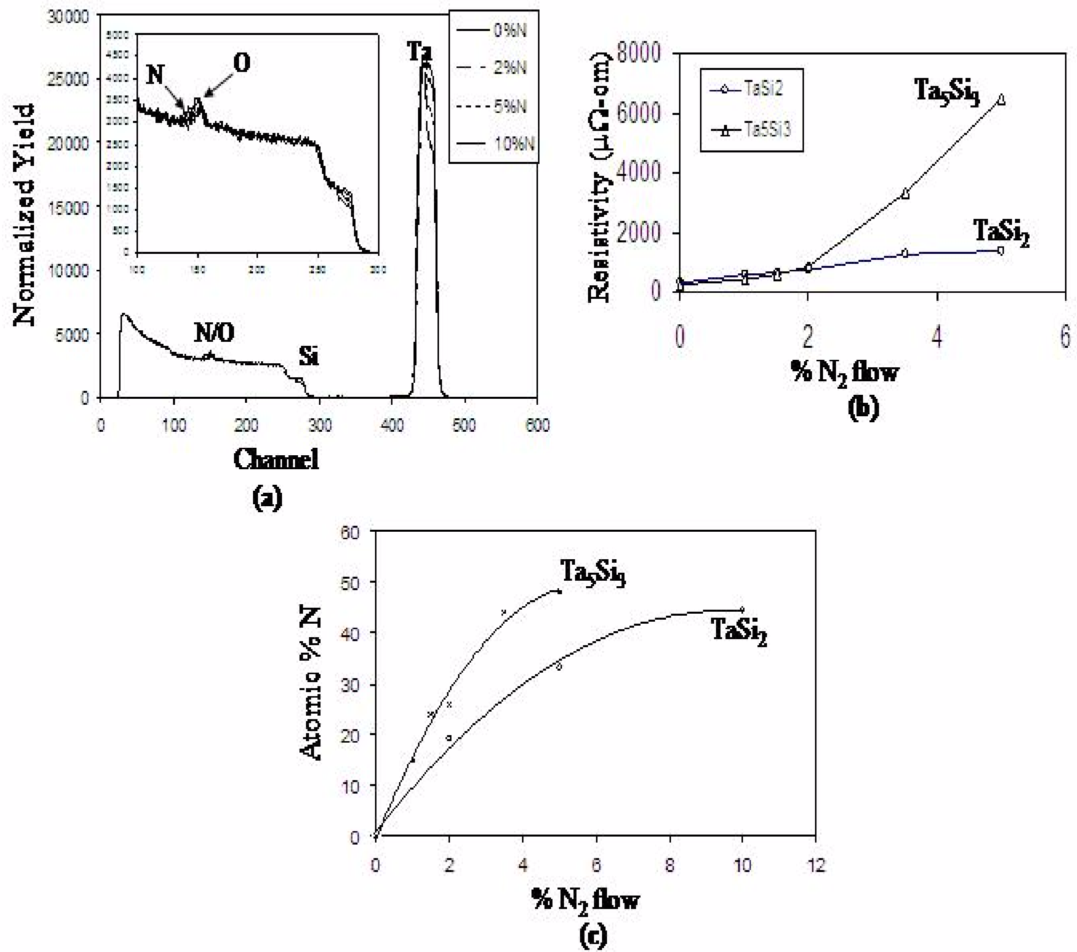

Figure 5.2: (a) RBS spectra of SiC/Ta-Si/Ta-Si-N with 0, 2, 5, 10% nitrogen content by flow rate (b) van der Pauw sheet resistivity of Ta-Si-N from $TaSi_2$ and Ta_5Si_3 targets (c) Nitrogen aomic percentage against nitrogen flow

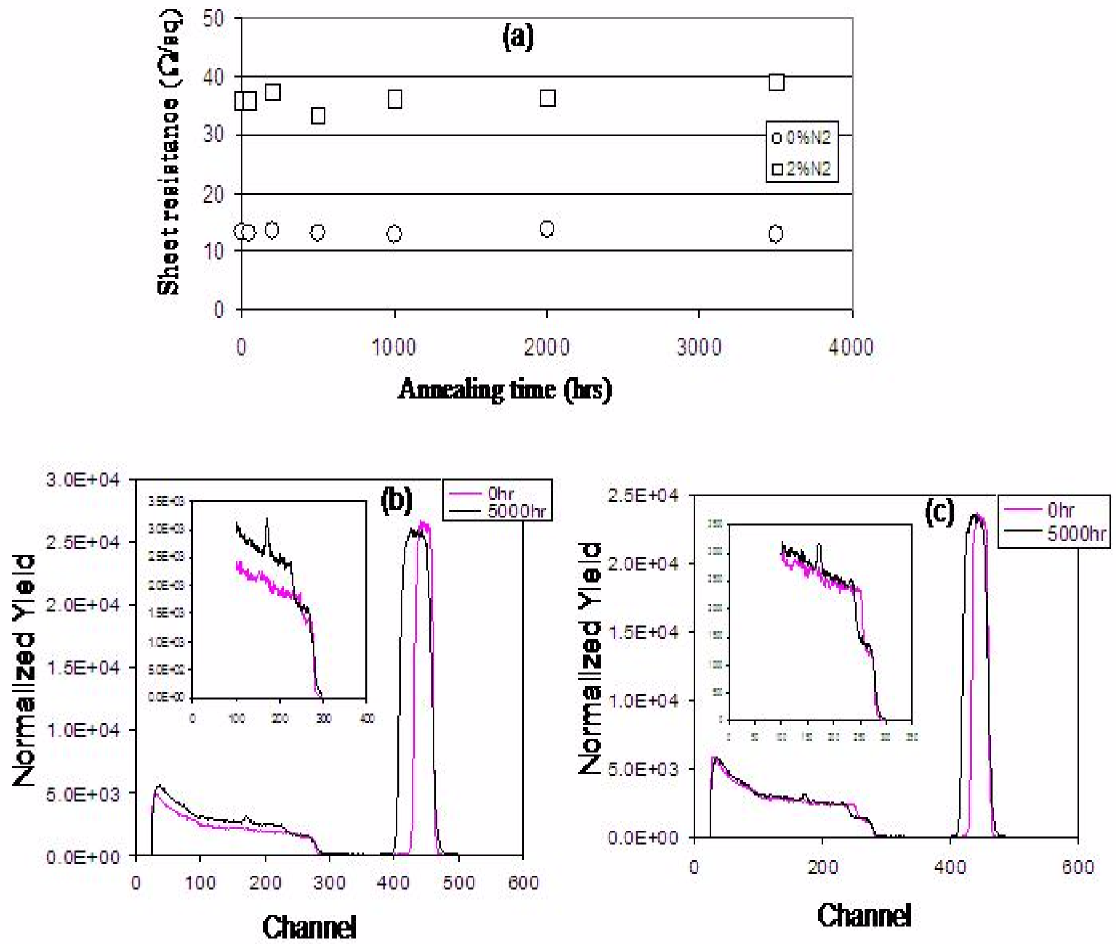

Figure 5.3: (a) Sheet resistance of Ta-Si-N on semi-insulating SiC against anneal time in air at 350°C (b) RBS spectra of Ta-Si-N on semi-insulating SiC for 0 and 5000hrs (b) 0% and (c) 2% nitrogen flow

5.1.2 Structure of Ta-Si-N

X-ray diffraction scans in figure 5.4 show that the Ta-Si-N films with different nitrogen content were amorphous (or possibly nanocrystalline) as deposited. The XRD scans also show that the films are more amorphous as the nitrogen content increases. There are no observable changes in the XRD scans after 750 hours of annealing in air or in an evacuated quartz tube at $350°C$. Annealing was performed to determine whether the films would become polycrystalline. It is known that amorphous materials become polycrystalline with time at elevated temperature [112]. Since amorphous layers are generally good diffusion barriers because of the absence of grain boundaries, the observed amorphous structure and its stability is a plus for Ta-Si-N.

5.2 Results on Ohmic Contacts

5.2.1 Contacts Without Protective Metallization

TLM results on ohmic contacts on p^+-4H-SiC and n^+-4H-SiC are presented in this section for samples without protective metallization. These samples were not annealed in air after fabrication. The results are for as-fabricated ohmic contacts but with different contact metal, metal thicknesses and contact anneal conditions.

Total contact-to-contact resistance was measured on samples annealed between $900-1000°C$ for 1 - 2 minutes. Typical plots of total resistance versus inter-contact spacing is shown in figure 5.5. Using the equation,

$$R_T = \frac{2\sqrt{r_c R_{sh}}}{W} + \frac{R_{sh} L}{W} \tag{5.1}$$

the specific contact resistance and sheet resistace of the implanted or epitaxial samples were

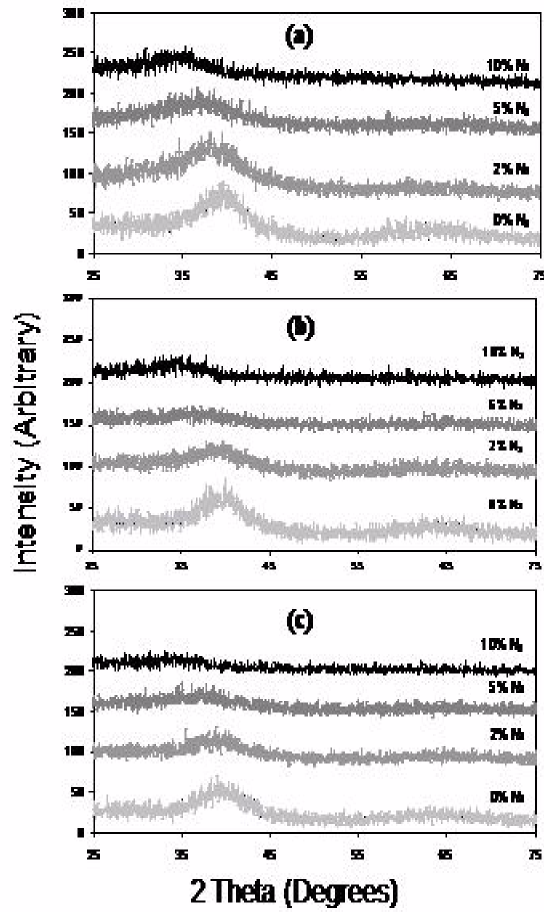

Figure 5.4: XRD scan of Ta-Si-N with 0, 2, 5, and 10% nitrogen flow (a) as-sputtered samples (b) samples annealed in air at 350°C for 750hrs (c) samples annealed in evacuated quartz tube at 350°C for 750hrs

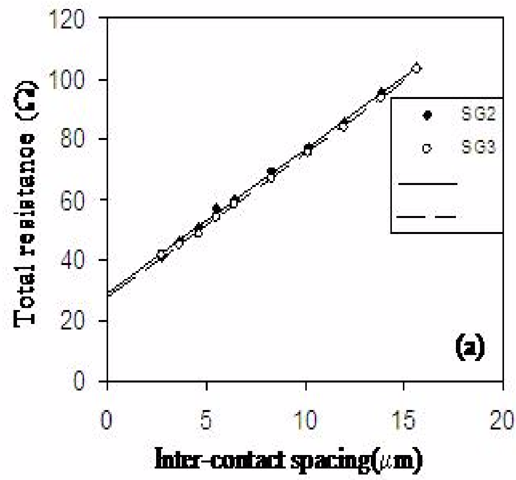

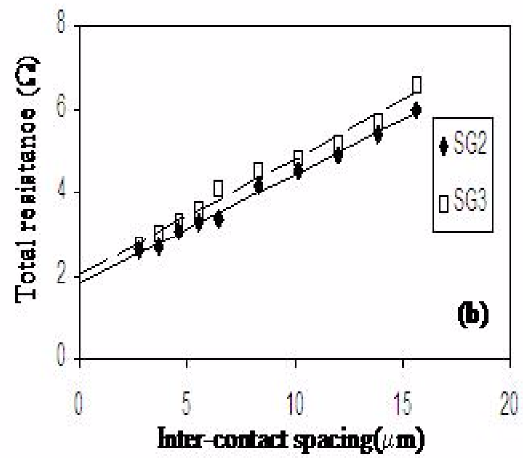

Figure 5.5: Total contact-to-contact resistance against inter-contact spacing for (a) nickel ohmic contact on p^+implanted material (b) nickel-chromium (80-20 wt%) ohmic contact on n^+epitaxial material

Target	4HSiC	t(nm)	Anneal condition	$r_c(\Omega - cm^2)$	$R_{sh}(\Omega/sq)$	M-$R_{sh}(\Omega/sq)$
$Al_{70}Ti_{30}$	p^+-impl.	240	$1000°C$/2min/Vac	1.10×10^{-3}	1.10×10^3	16.4/1.8
$Al_{70}Ti_{30}$	p^+-impl.	110	$1000°C$/2min/Vac	3.95×10^{-4}	9.43×10^2	40.2/7.2
$Al_{70}Ti_{30}$	p^+-epi.	100	$1000°C$/2min/Vac	3.70×10^{-4}	1.47×10^3	67.8/13.5
$Al_{70}Ti_{30}$	p^+-epi.	190	$1000°C$/2min/Vac	4.20×10^{-3}	5.07×10^2	15.7/1.9
$Al_{90}Ti_{10}$	p^+-impl.	300	$1000°C$/2min/Vac	2.10×10^{-4}	1.67×10^3	-/0.9
$Ni - 7\%V$	n^+-epi.	200	$1000°C$/2min/Vac	1.07×10^{-4}	43.6	11.9/2.0
$Ni - 7\%V$	p^+-impl.	140	$1000°C$/2min/Vac	8.33×10^{-5}	9.55×10^2	52.1/4.4
$Ni - 7\%V$	p^+-impl.	100	$900°C$/1min/Vac	5.79×10^{-5}	1.09×10^3	43.5/5.4
$Ni - 7\%V$	n^+-epi.	100	$950°C$/2min/Vac	1.95×10^{-5}	42.6	-
$Ni_{80}Cr_{20}$	n^+-epi.	50	$1000°C$/2min/Vac	8.10×10^{-5}	34.3	-/13.6
$Ni_{80}Cr_{20}$	n^+-epi.	100	$1000°C$/2min/Vac	6.90×10^{-6}	53.6	-/5.2
			$500°C$/120min/H_2	7.00×10^{-6}	53.6	5.2/4.2
$Ni_{80}Cr_{20}$	p^+-impl.	130	$1000°C$/2min/Vac	1.20×10^{-4}	9.71×10^2	48.9/5.9
$Ni_{80}Cr_{20}$	p^+-impl.	100	$900°C$/1min/Vac	2.09×10^{-4}	1.23×10^3	60.3/7.4
$Ni_{20}Cr_{80}$	p^+-impl.	90	$1000°C$/2min/Vac	2.00×10^{-4}	9.62×10^2	-
$Ni_{20}Cr_{80}$	n^+-epi.	100	$1000°C$/2min/Vac	3.10×10^{-4}	57.3	-/10.0
$Ni_{60}Cr_{40}$	n^+-epi.	100	$1000°C$/2min/Vac	9.50×10^{-5}	41.2	-/3.7
$Ni_{60}Cr_{40}$	n^+-epi.	50	$1000°C$/2min/Vac	4.80×10^{-5}	39.6	-/8.3
Al1% Si/ $Ni - 7\%V$	p^+-impl.	10/40	$925°C$/2min/Vac	1.20×10^{-4}	1.12×10^3	-/1.9
Ti/Al1% Si/ $Ni - 7\%V$	p^+-impl.	1/1/4	$925°C$/2min/Vac	1.51×10^{-4}	1.06×10^3	-

Table 5.1: Various ohmic contacts fabricated in this study. The metal in contact with the SiC is on the left for the case of two or more layers. The metal sheet resistance ($M - R_{sh}$) column has values before/after contact annealing. t is the contact metal thickness.

determined. Table 5.1 shows the list of various ohmic contacts that were fabricated during the course of this study.

RBS spectra of the as-deposited and annealed nickel contacts are shown in figure 5.6. These plots indicated the reaction of Ni with SiC at high temperature ($> 900°C$) to form nickel silicide which is ohmic on SiC. Nickel silicide sputter-deposited on SiC from a silicide target does not form an ohmic contact to SiC. A high temperature reaction is necessary, as reported previously [5].

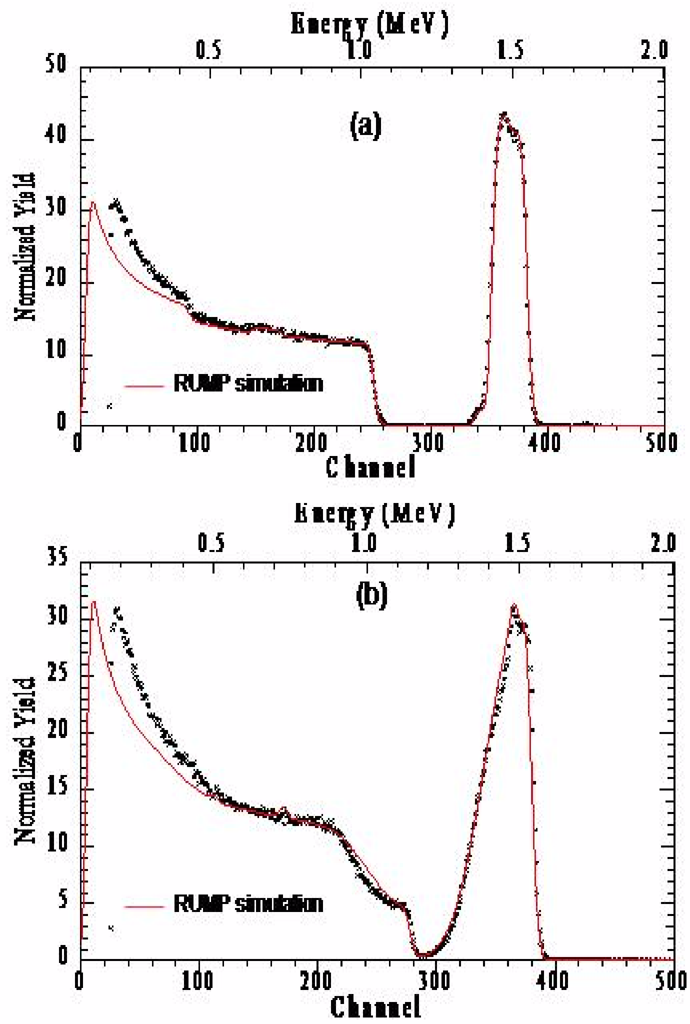

Figure 5.6: Experimental and RUMP simulated RBS spectra of (a) as-deposited nickel contact on SiC (b) nickel ohmic annealed on SiC

5.2.2 Ohmic Contact with Protective Metallization

Ohmic contact on p^+-4HSiC

The first sets of ohmic contacts on p^+ 4H-SiC were formed from 70-30wt% Al-Ti and 93-7wt% Ni-V. The protective stack was Ta-Si-N/Pt-N and the cap layer was Au/Sn/Au. Tin was sandwiched between Au layers to simulate the 80-20wt% Au-Sn preform that was later used for chip brazing. The percentages of N_2 flow in the sputter gas was 0, 1, 1.5 and 2. These percentages are the fractions of N_2 flow rate to the total flow rate (Ar plus N_2) during sputter-deposition. TLM results for the as-fabricated ohmic contacts with protective metallization stacks were analyzed to obtain the specific contact resistance and sheet resistance of the contacts. At certain times during the anneals of in air, the measurements were repeated. Figure 5.7 shows the plot of specific contact resistance and SiC sheet resistance as a function of annealing time up to 4000 hours for 0 and 2% nitrogen content in the stack.

The specific contact resistance and the sheet resistance for nickel contact were stable after 4000 hours of annealing. However, the Al-Ti contact without nitrogen in the protective stack showed significant changes in the specific contact resistance and sheet resistance values after about 2500 hour of anealing. The variations most probably mark the begining of the failure of Al-Ti contact due to the oxidation of Al. The Al-Ti contact with 2% nitrogen content in the protective stack was still very stable after 4000 hours of annealing. The observed electrical stability of the ohmic contacts testifies to the effectiveness of the protective stack on the p-type ohmic contact.

Mixing/diffusion and oxidation of the composite ohmic multi-layered metallization stack were monitored with RBS and AES. Little oxidation and inter-diffusion were observed in the RBS spectra of figure 5.8(a) for the broad area Ni contacts. However, mixing is apparent in

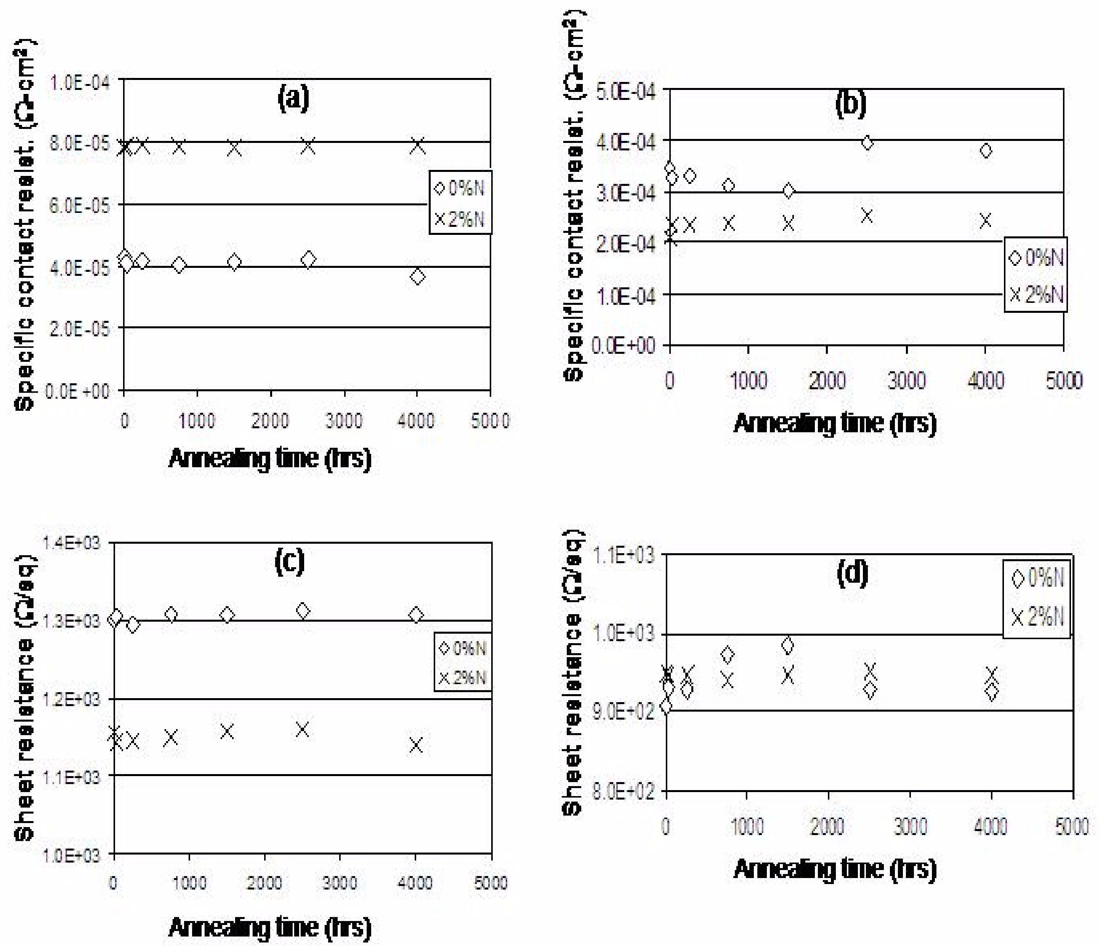

Figure 5.7: Specific contact resistance and SiC sheet resistance against annealing time for (a,c) SiC/Ni(ohmic)/Ta-Si-N/Pt-N/Au/Sn/Au (b,d) SiC/Al-Ti(ohmic)/Ta-Si-N/Pt-N/Au/Sn/Au

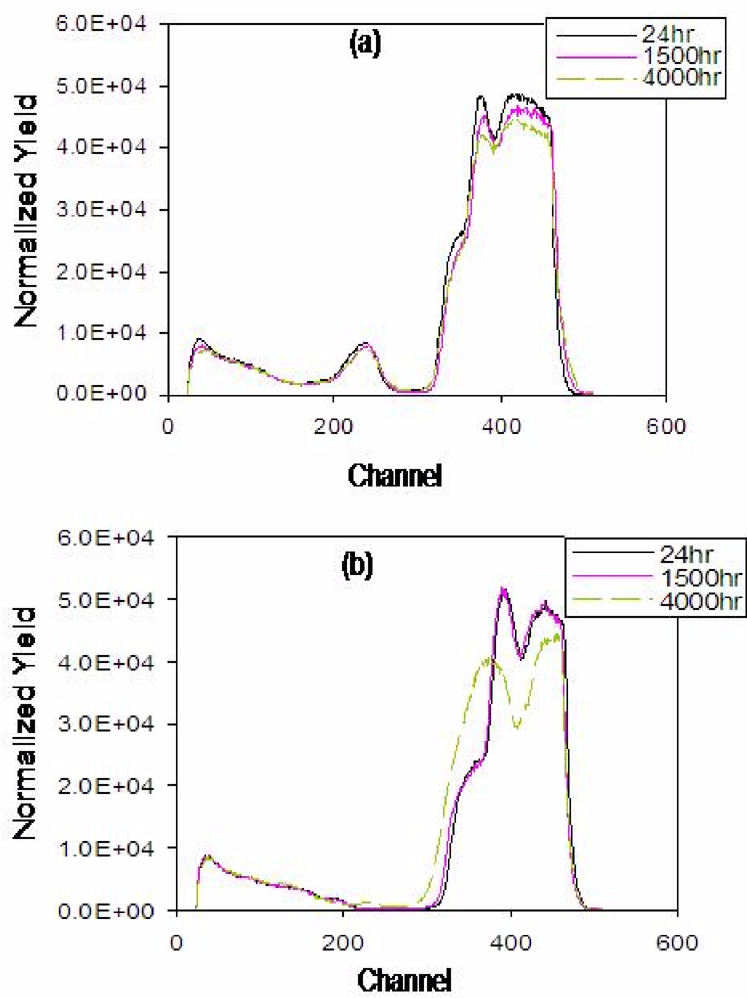

Figure 5.8: RBS spectra of p-ohmic contact after 24, 1500 and 4000hrs annealing (a) nickel ohmic contact with 2% nitrogen in the stack (b) Al-Ti ohmic contact with 2% nitrogen in the stack.

the Al-Ti contact after 4000hrs. AES data shows better resolution of the very light elements. Figure 5.9(a) is for an unannealed, as-deposited nickel contact. Oxygen at the nickel surface was observed, with less oxygen throughout the nickel and Ta-Si-N layers. The surface oxygen was picked-up when the sputter system was opened to change targets. Oxygen is also observed in the ohmic annealed nickel contact [figure 5.9(c)], but does not affect the electrical characteristics of the contacts adversely. During ohmic contact annealing, Ni reacts with Si in SiC leaving a carbon rich surface between SiC and the resulting Ni-Si contact. The opposite surface of the Ni-Si contact is also rich in C, and surface oxygen is clearly visible as shown in figures 5.9(b) and (d).

With or without nitrogen in the stack, the cap layers and the Pt layer do not diffuse through Ta-Si layer. Tantalum silicide effectively prevents the diffusion of Pt and Au, though limited mixing is observed at the Pt-Au and Pt-TaSiN interfaces after 1500 hours. The Sn layer sandwiched between Au layers diffuse into the Au layers with increasing annealing time.

Figures 5.10 shows that carbon diffuses more readily through the Ta-Si barrier layer if there is no nitrogen in the layer. 2% (by flow rate) nitrogen content in Ta-Si-N reduces the rate of C diffusion appreciably. Sputter-deposition of the tantalum silicide target in an Ar/N_2 gas mixture improves the barrier property of Ta-Si-N significantly. It is also true that after a 3000hr anneal in air the amount of O_2 in the stack does not increase significantly above the level observed in the as-deposited samples. As a result the electrical properties of the composite contacts remain stable after 4000hr of annealing in air at $350°C$.

Ohmic contact on n^{+}-4HSiC

Ohmic contact on n^{+}-epilayers were first fabricated with 80-20wt% Ni-Cr. The specific contact resistances with or without nitrogen content in the protective stack (Ta-Si-N/Pt-N/Au/Sn/Au)

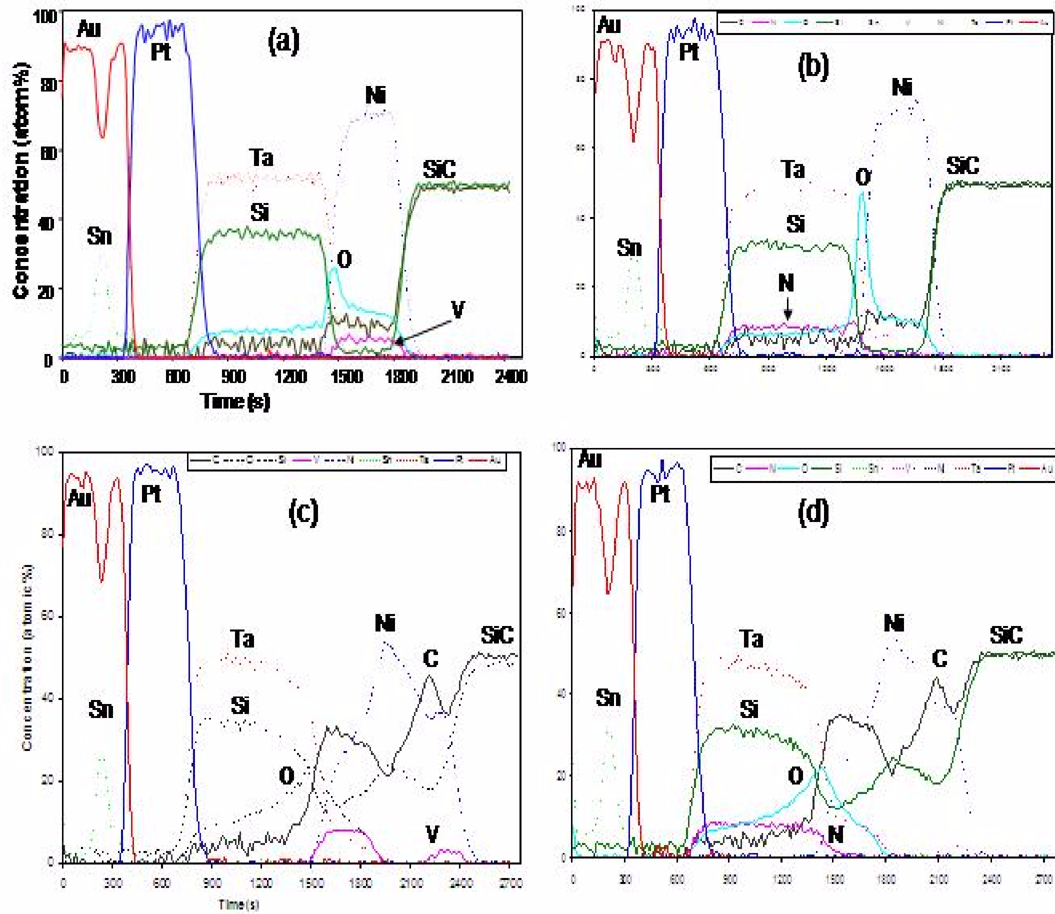

Figure 5.9: AES spectra for (a) as-deposited nickel contact with no nitrogen in the metallization stack (b) as-deposited nickel with 2% nitrogen in the stack (c) nickel ohmic contact with no nitrogen in the stack (d) nickel ohmic with 2% nitrogen in the stack

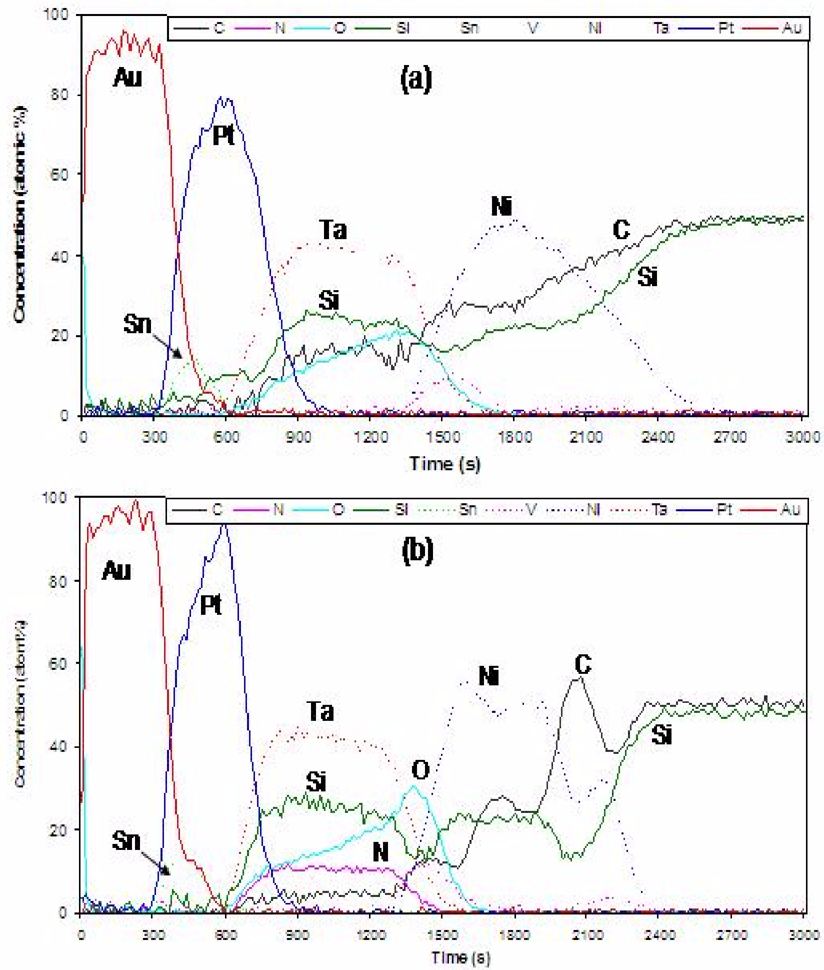

Figure 5.10: AES spectra of nickel ohmic contacts annealed in air at $350°C$ for 1500hrs (a) nickel ohmic contacts with no nitrogen in the stack (b) nickel ohmic contacts with 2% nitrogen in the stack

were very low prior to annealing the samples in air at $350°C$. For contacts without nitrogen content and with 1% (by flow rate) of N_2 in the stack, it was impossible to accurately measure the total contact-to-contact resistance after 24 hours of annealing in air at $350°C$. For stacks with 1.5% and 2% N_2 rate, the contact resistance increases after 24 hours of annealing by about a factor of four. After the initial increase, the specific contact resistance remains almost constant for up to 4000 hours of annealing. Figure 5.11 shows the plots of specific contact resistance and sheet resistance against the time of annealing. The reason for the sudden increase in contact resistance is not apparent from the RBS data where no appreciable oxidation or diffusion was observed. AES spectra, however, showed that there is high diffusion of carbon into the barrier layer as the time of annealing increases, so the increase in resistance may be due to the increase of carbon content and its accumulation at the interface between the ohmic contact and the Ta-Si-N layer. Figure 5.12 shows RBS and AES plots.

5.2.3 Metallization with Hot Platinum

Adhesion problems between Ta-Si-N and Pt-N in the metallization stack were identified during the brazing of the stack to a ceramic carrier. To overcome this problem, Pt was sputter-deposited on SiC/.../Ta-Si-N kept at $250°C$ during the period of Pt deposition. This modification increases adhesion between Pt and Ta-Si-N dramatically. The process of ohmic contact fabrication with the protective stack was subsequently modified because the photoresist normally used to pattern the metallization will carbonize at $250°C$ and become difficult to remove. Molybdenum was found to be suitable for lifting-off hot Pt in H_2O_2. An acid etch back of the hot Pt also worked well, except that very small features of TLM were difficult to etch.

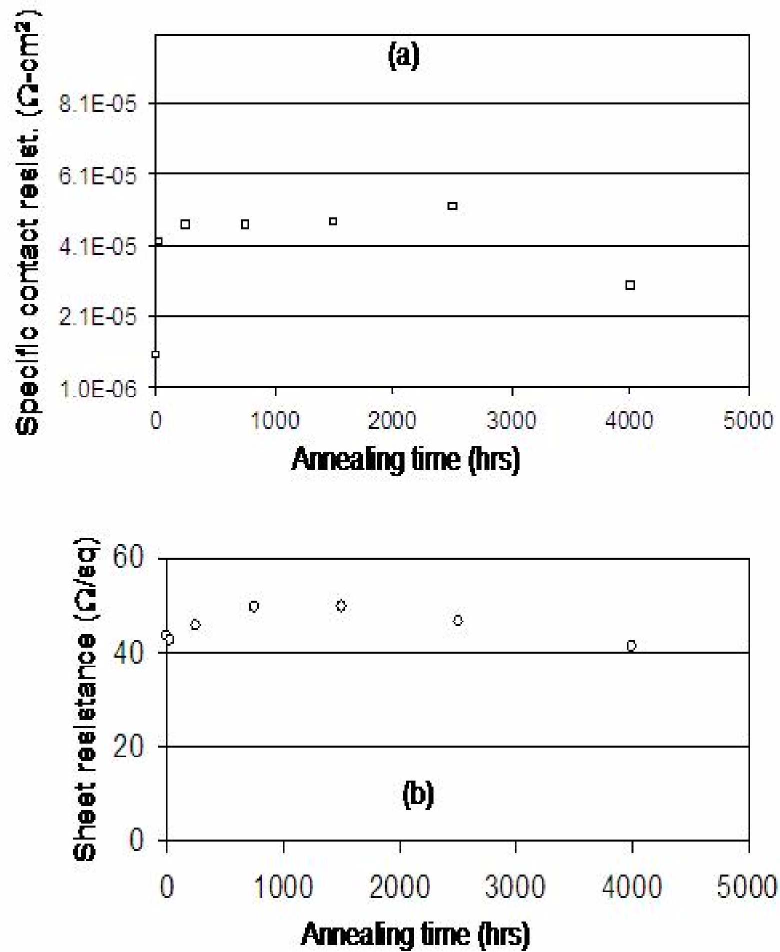

Figure 5.11: (a) Plots of specific contact resistance against annealing time for Ni-Cr (80-20 wt%) ohmic contacts with 2% nitrogen in the stack (b) Plots of SiC sheet resistance against annealing time for Ni-Cr (80-20 wt%) ohmic contacts with 2% nitrogen in the stack

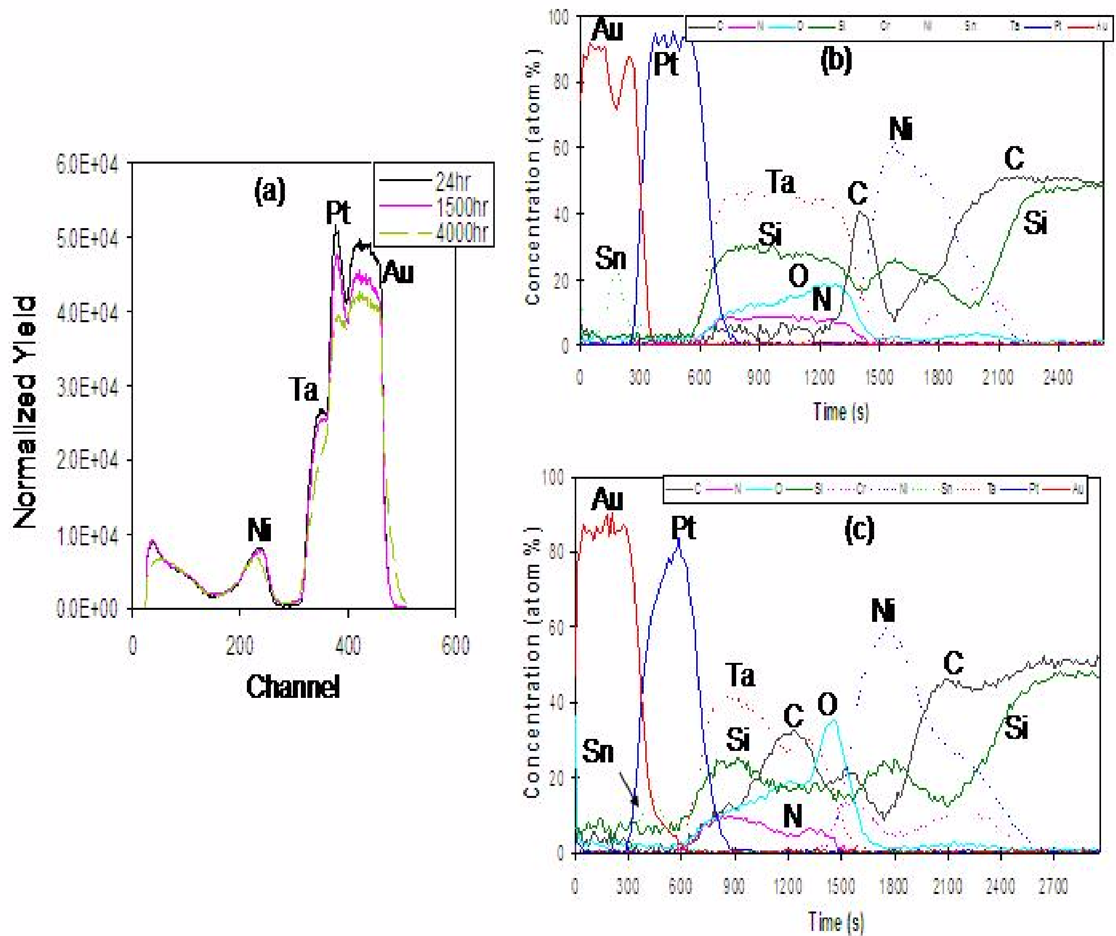

Figure 5.12: (a) RBS spectra of Ni-Cr (80-20 wt%) ohmic contacts after 24 and 4000hrs annealing; AES spectra of Ni-Cr (80-20 wt%) ohmic contacts with 2% nitrogen in the stack (b) before annealing in air (c) afer annealing in air for 1500hrs

All nickel ohmic contact with hot Pt metallization

Because of the success with nickel ohmic contacts on p^+-implanted 4H-SiC, the decision was made to use nickel ohmic contacts on both p^+ and n^+ material with Pt in the protective metallization stack sputtered on hot substrates. With this modified metallization scheme, TLM measurement on nickel ohmic contacts to p- and n-SiC were carried out. Nickel ohmic contacts on p^+-implanted 4H-SiC was very similar to those obtained before with cold Pt in the metallization stack. This implied that sputtering Pt at $250°C$ does not affect the contact resistance significantly (Figure 5.13). For the ohmic contact on n^+-epilayers, the contact resistance increases generally with annealing in air at $350°C$. However, the total contact-to-contact resistance for several pads increased sharply out of the normal range ($\sim< 10\Omega$) and the direct proportionality of the resistance to inter-contact spacing was lost after a few hundreds of hours annealing. It was difficult to determine the problem with the RBS (figure 5.14). Both RBS and AES did not indicate oxidation of the contacts as the cause of the problem.

Plots of total contact-to-contact resistance, specific contact resistance and SiC sheet resistance as a function of annealing time for nickel contacts on p- and n-SiC are shown in figures 5.15 and 5.16.

Contact resistance at elevated temperatures

TLM results at temperatures up to $350°C$ for implanted samples and the corresponding specific contact resistance and sheet resistance are shown in figure 5.17. Both r_c and R_{sh} approache minimum values at elevated temperatures. The contact properties measured at room temperature were reproduced after measurements at elevated temperatures.

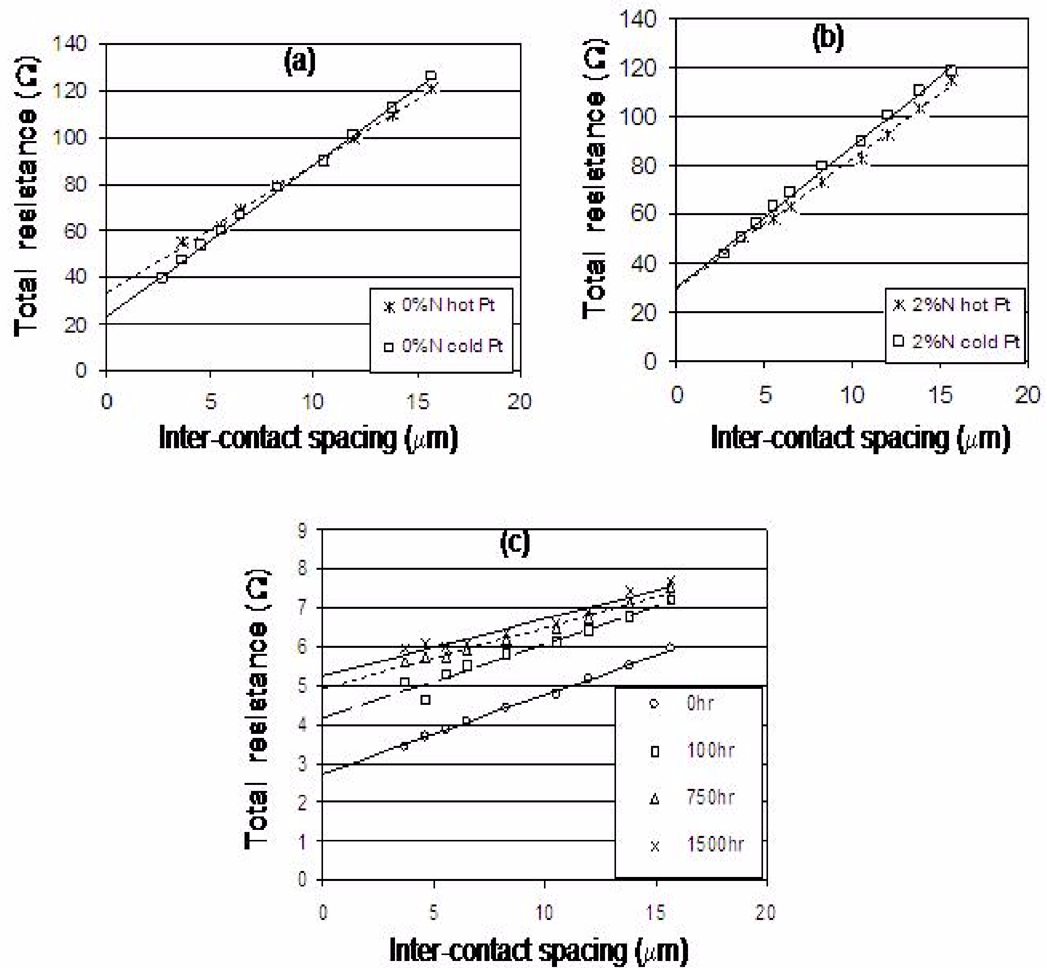

Figure 5.13: Total contact-to-contact resistance of (a) cold and hot Pt in the metallization stack with no nitrogen content (b) cold and hot Pt in the metallization stack with 2% nitrogen content (c) nickel ohmic contact on n^+epilayer SiC with hot Pt and 2% nitrogen in the metallization stack after different anneal times in air

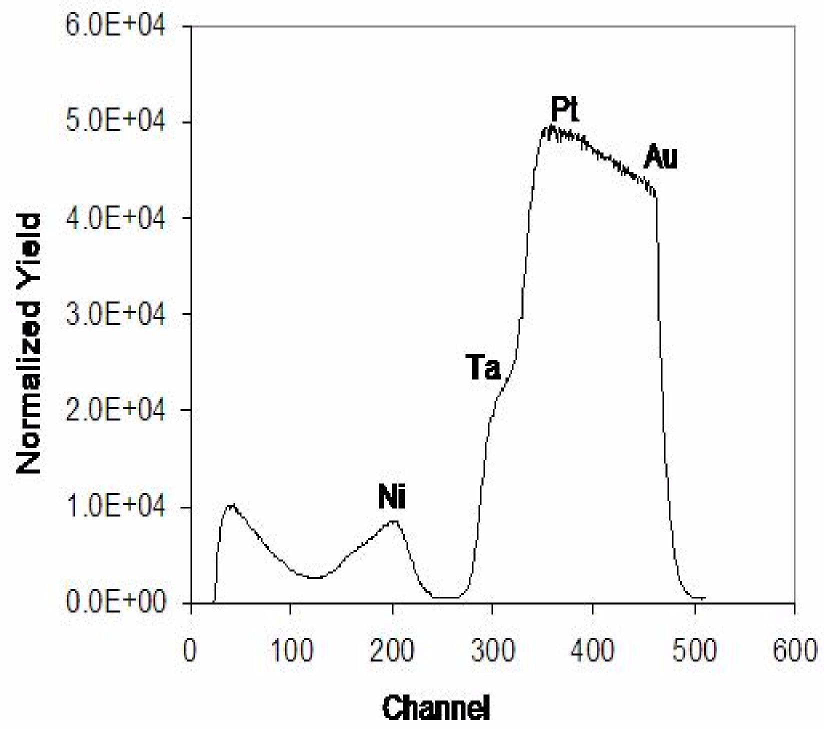

Figure 5.14: RBS spectrum of a nickel ohmic contact on n^+epitaxial 4H-SiC.

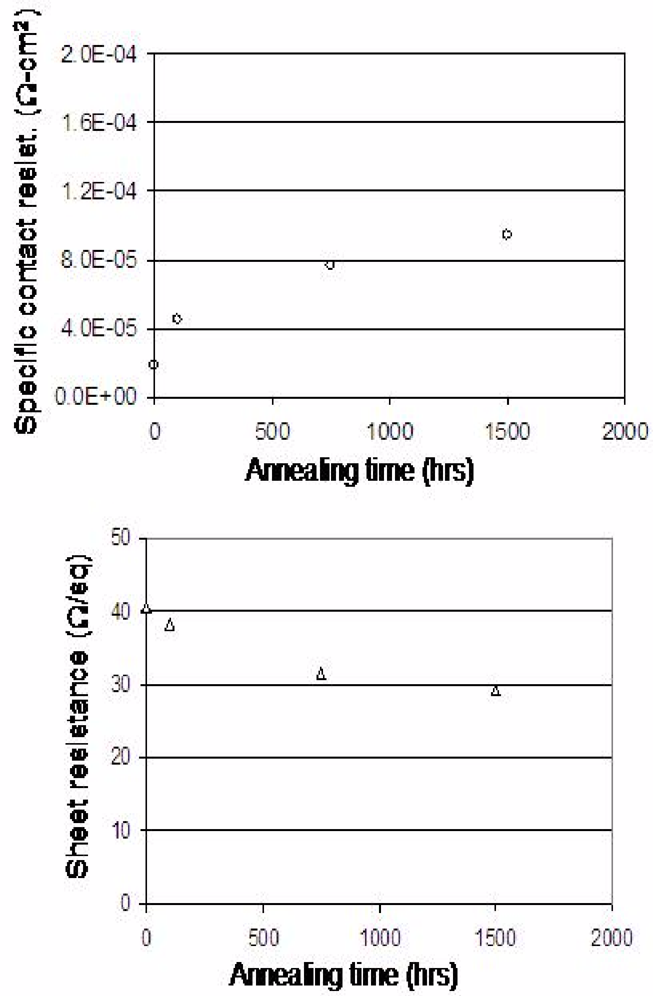

Figure 5.15: Specific contact resistance and SiC sheet resistance for nickel ohmic contacts on n^+epitaxial 4H-SiC with hot Pt and 2% nitrogen content in the metallization stack.

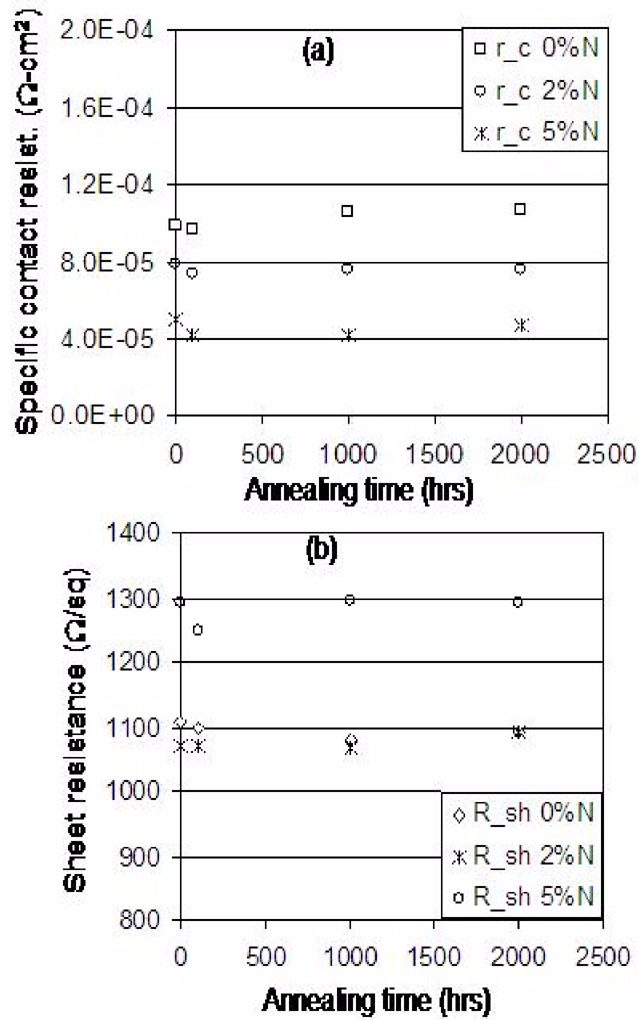

Figure 5.16: Specific contact resistance and SiC sheet resistance of nickel ohmic contacts on p^+implanted 4H-SiC with hot Pt in the metallization stack.

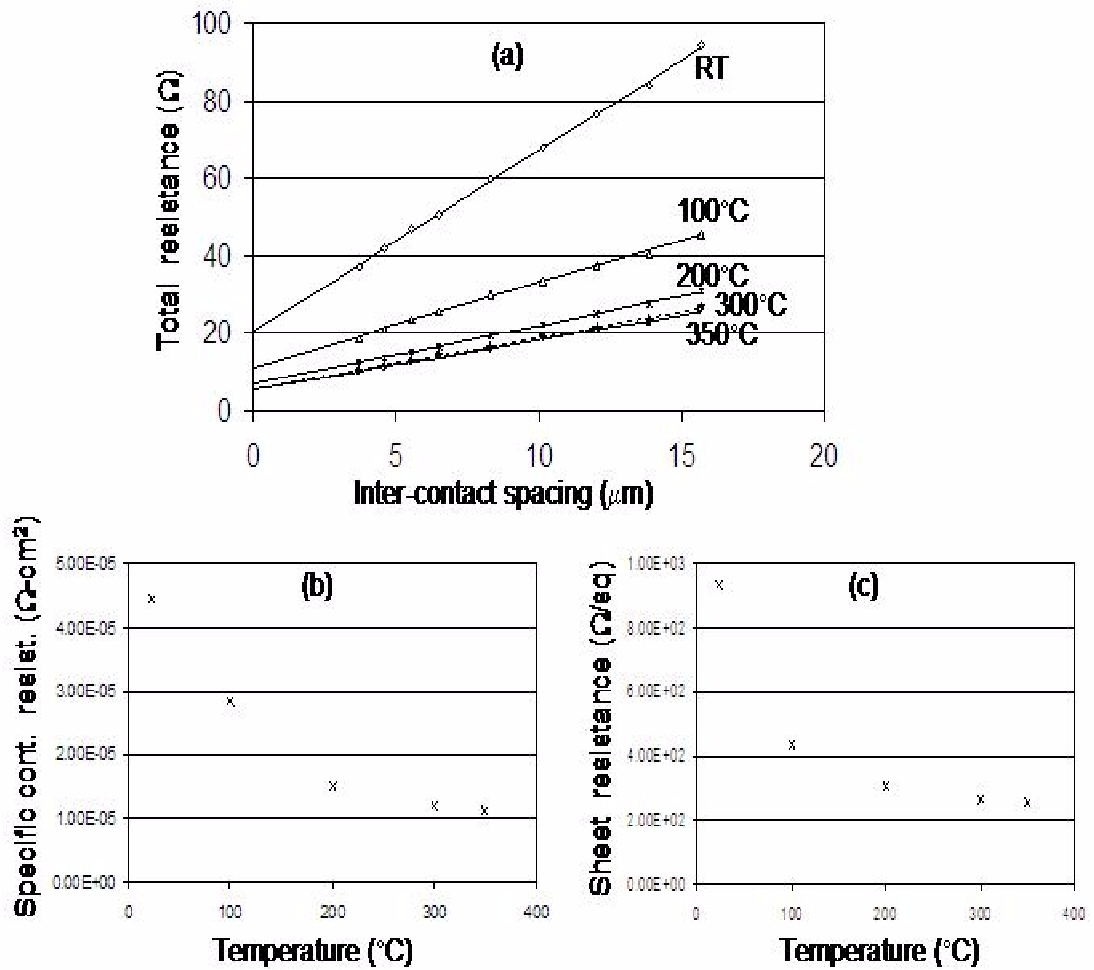

Figure 5.17: Plots of (a) total contact-to-contact resistance against inter-contact spacing (b) Specific contact resistance against temperature and (c) SiC sheet resistance against temperature for nickel ohmic contact on p^+implanted 4H-SiC with 2% nitrogen in the metallization stack.

5.3 Results for Schottky Contacts

5.3.1 I-V and C-V Results

The metal contact on the first set of Schottky diodes were sintered nickel silicide (Ni_2Si) with 0 - 2% nitrogen (by flow rate) in the stack metallization. A significant decrease in the number of good diodes with 0% nitrogen content was observed after only 24 hrs annealing. After 1500 hrs anneal, almost all devices with 0% and 1% nitrogen content were bad, and less than 50% of the diodes with 2% nitrogen in the stack were still functional. The first indication of problems with the diodes was the drop of 3 to 6 orders of magnitude in current at 2V forward bias. Because the structure of the diodes was such that the protective stack does not cover the whole of the silicide contact, it is believed that at $350°C$ the exposed silicides at the circumference of the diode oxidized and that the oxide grew laterally under the protective stack, thus causing an increase in the resistance of the contact metal. The barrier height or turn-on voltage of the devices incresed to more than double the initial value after 24 hrs anneal, but subsequently remained stable subsequently as shown in figure 5.18. The ideality factor also shows that the diodes behave more ideally after stabilizing. However, very few devices survived the 4000 hour anneal.

New Schottky devices

The new sets of Schottky devices were fabricated so that the protective stack overlayed the contact layer and a portion of the passivating oxide layer around devices. Two sets of diodes were fabricated, devices with unsintered nickel silicide contacts and devices with Ta-Si-N used as the contact metal. 0, 2, 5 and 10% by nitrogen flow rate was used in the stacks. The Pt in the metallization was sputter-deposited hot and etched-back in an acid solution.

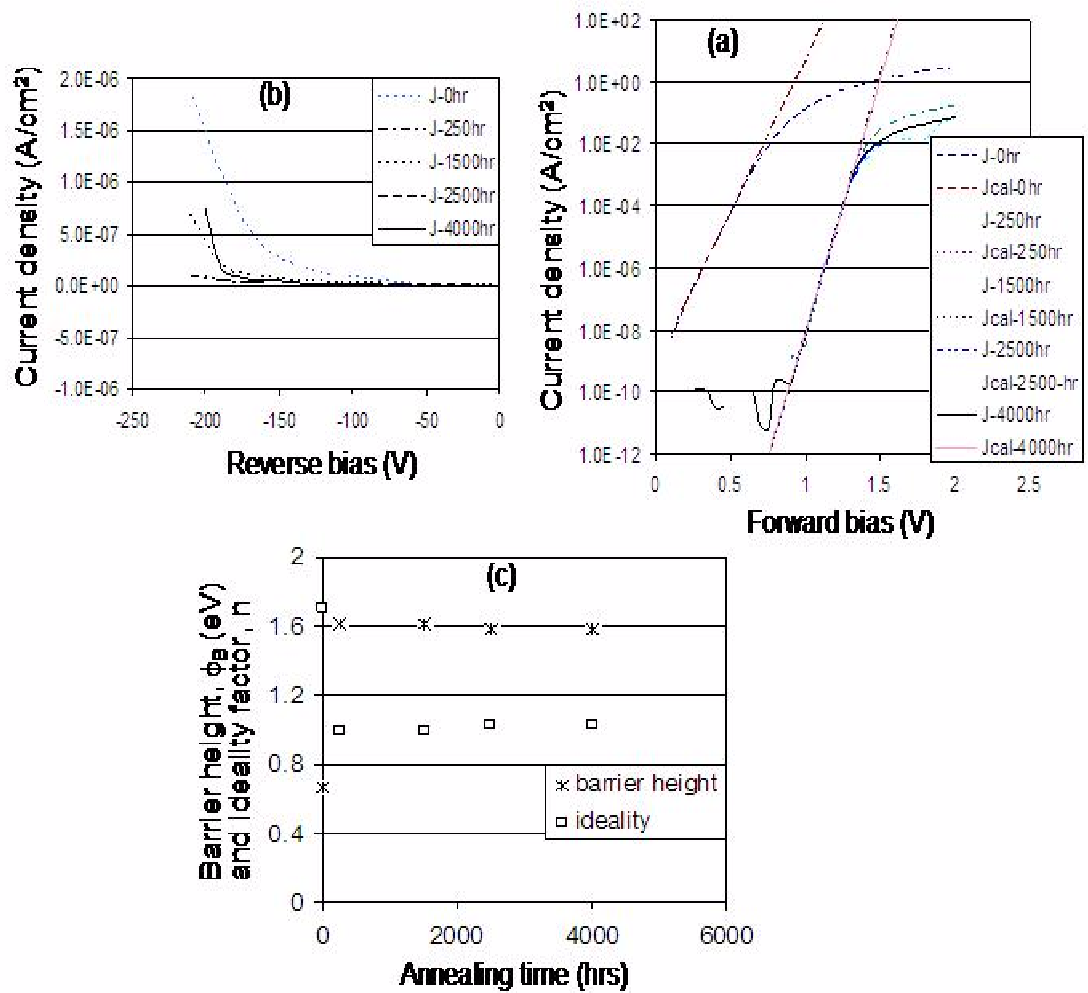

Figure 5.18: Nickel silicide Schottky devices (a) forward J-V dependence on annealing time (b) reverse J-V dependence on annealing time (c) barrier height and ideality factor against annealing time.

The yeild and distribution of the devices according to the leakage current at -10V reverse bias are shown on bar charts in figure 5.19. The Ta-Si-N Schottky have higher leakage than the nickel silicide Schottky, but Ta-Si-N devices are more stable as a function of annealing time.

The purpose of the Schottky device was to evaluate the effectiveness of the protective stack in air at $350°C$, since Schottky diodes are more sensitive to whatever is happening at the metal-semiconductor interface. The current density - voltage characteristics of the nickel silicide Schottky devices are shown in figures 5.20 and 5.21, while figures 5.22 and 5.23 show similar result for the Ta-Si-N devices. The forward characteristics up to 2V and the reverse characteristics out to -300V are shown for various nitrogen percentages. Very slight shifts to higher barrier height were generally observed for all devices, but more significantly for devices with 0% nitrogen content. Theoretical fits to the forward characteristics using the thermionic emission equations were plotted with the experimental data to monitor the barrier height and ideality factor as a function of anneal time. The barrier heights were generally stable with time of annealing for both set of devices. The ideality factors of the diodes also remain stable and near unity with annealing time. These results implied that the stack layer effectively protects the contacts for high temperature exposures in air. Figure 5.22 show plots of barrier height and ideality factors as a function of annealing time for devices with different nitrogen content in the stack metallization.

Capacitance measurements were made with the diodes under reverse bias to -4V, in order to extract barrier parameters. Plots of $(A/C)^2$ against the magnitude of reverse potential are shown in figures 5.25 and 5.26 for various annealing times and for different nitrogen content in the stack.

The linearity of $(A/C)^2$ indicated uniform doping concentration and the fact that the minority carrier concentration in these devices are negligible. More than 70% of the devices had linear characteristics that remained so after 1500 hr anneals in air. The barrier heights were

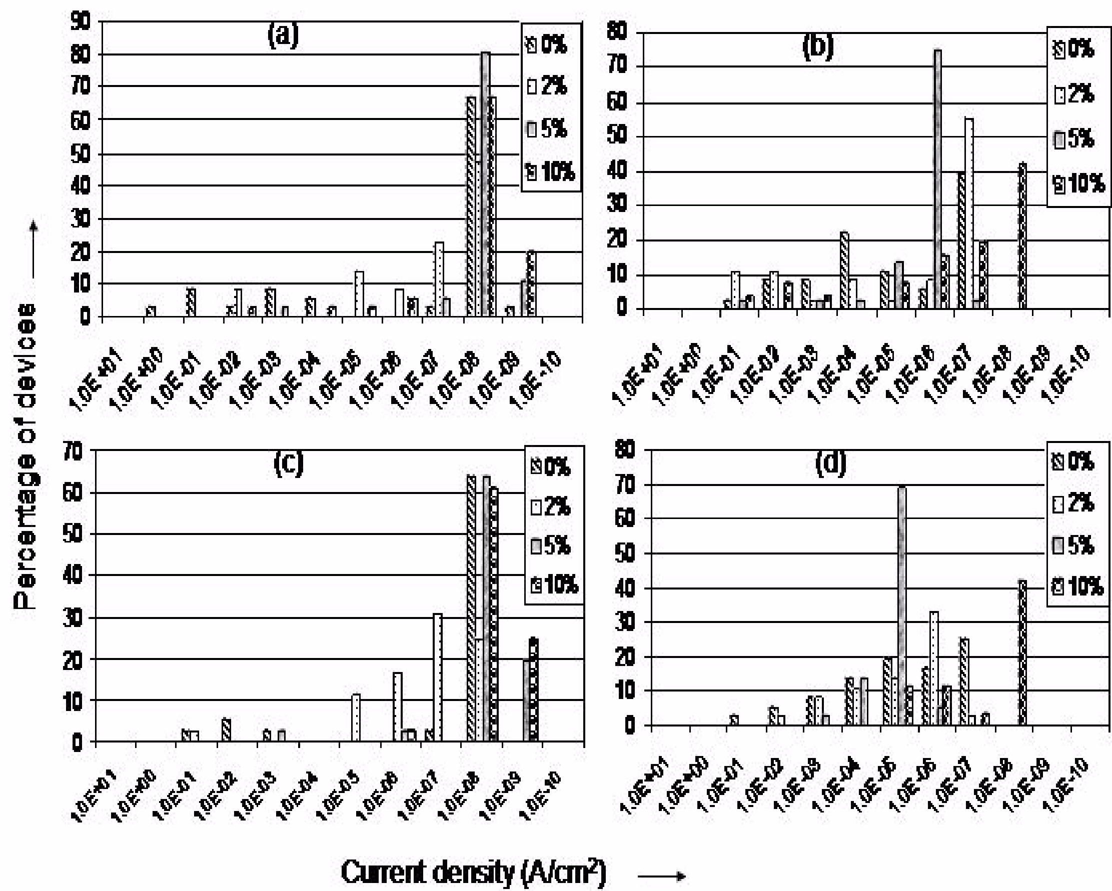

Figure 5.19: Bar chart of current density at -10V reverse bias for nickel silicide and Ta-Si-N Schottky devices (a) 0hr nickel silicide contacts (b) 0hr Ta-Si-N contacts (c) 1500hr nickel silicide contacts (d) 1500hr Ta-Si-N contacts

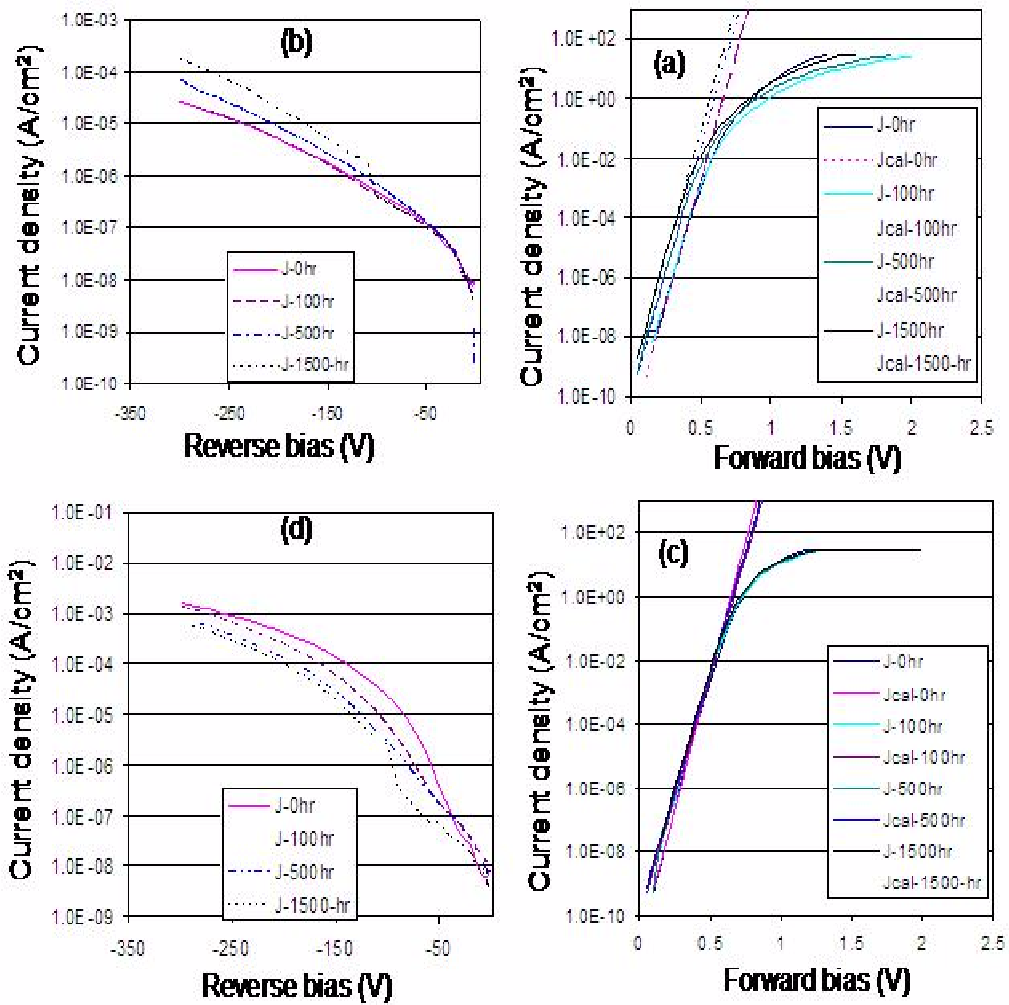

Figure 5.20: Nickel silicide Schottky devices (a) forward characteristics with 0% nitrogen (b) reverse characteristics with 0% nitrogen (c) forward characteristics with 2% nitrogen (d) reverse characteristics with 2% nitrogen.

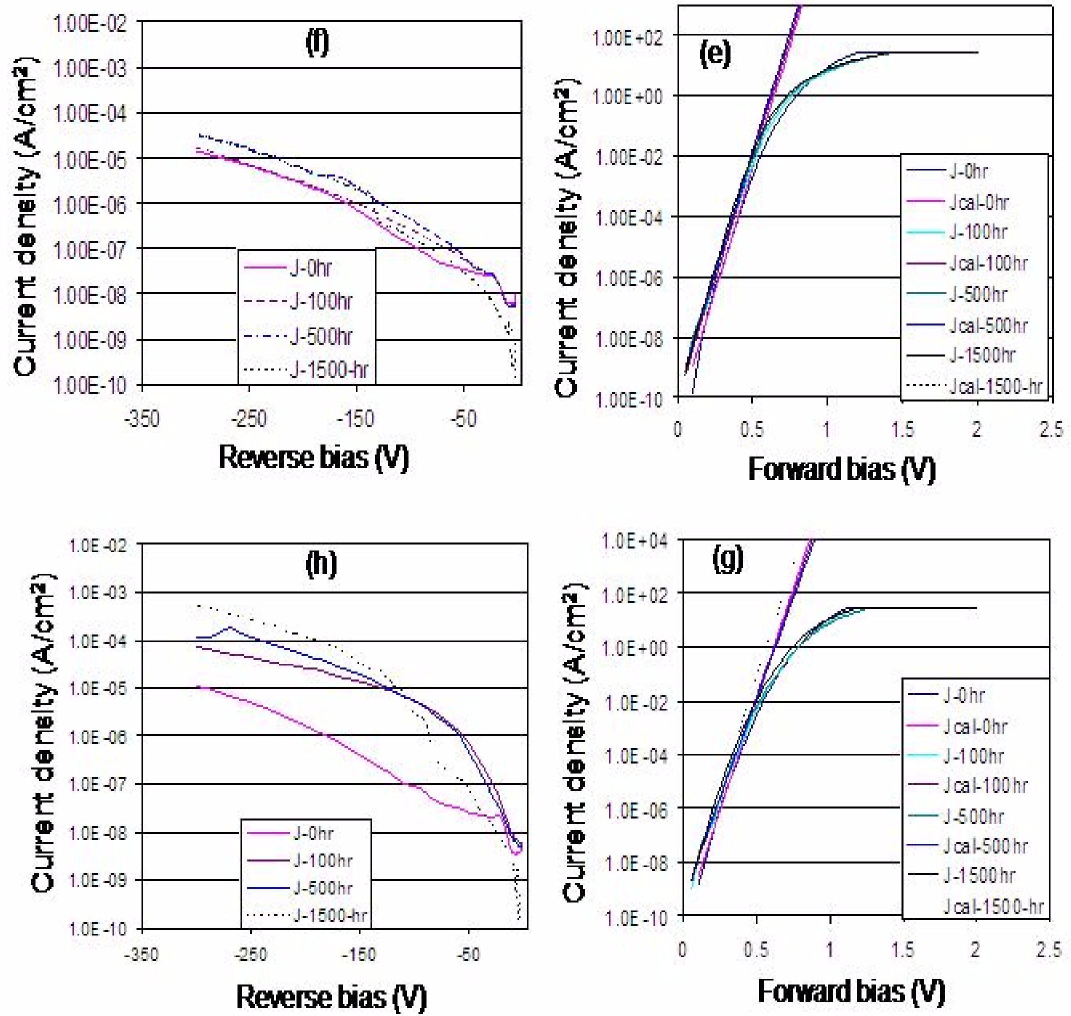

Figure 5.21: (e) Forward characteristics with 5% nitrogen (f) Reverse characteristics with 5% nitrogen (g) Forward characteristics with 10% nitrogen (h) Reverse characteristics with 10% nitrogen.

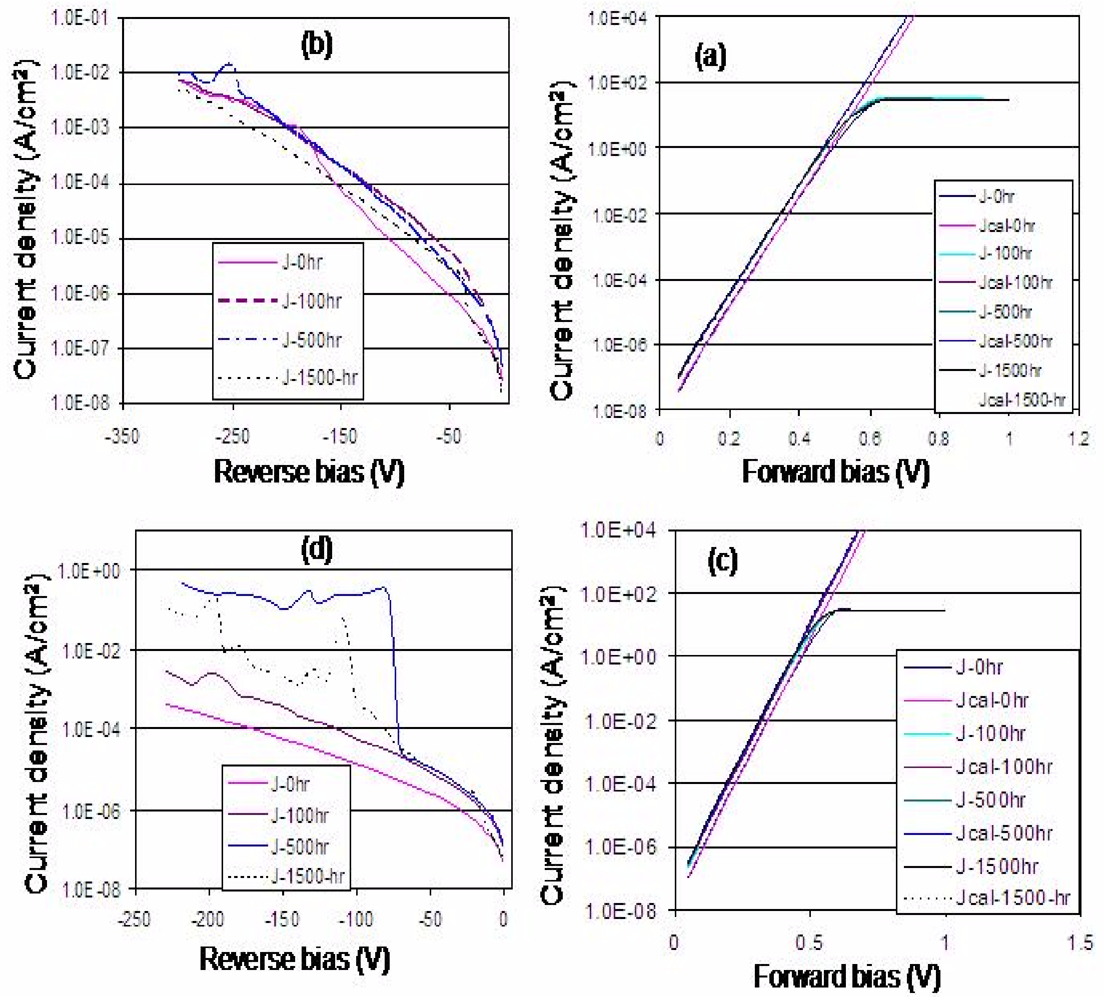

Figure 5.22: Ta-Si-N Schottky devices (a) forward characteristics with 0% nitrogen (b) reverse characteristics with 0% nitrogen (c) forward characteristics with 2% nitrogen (d) reverse characteristics with 2% nitrogen.

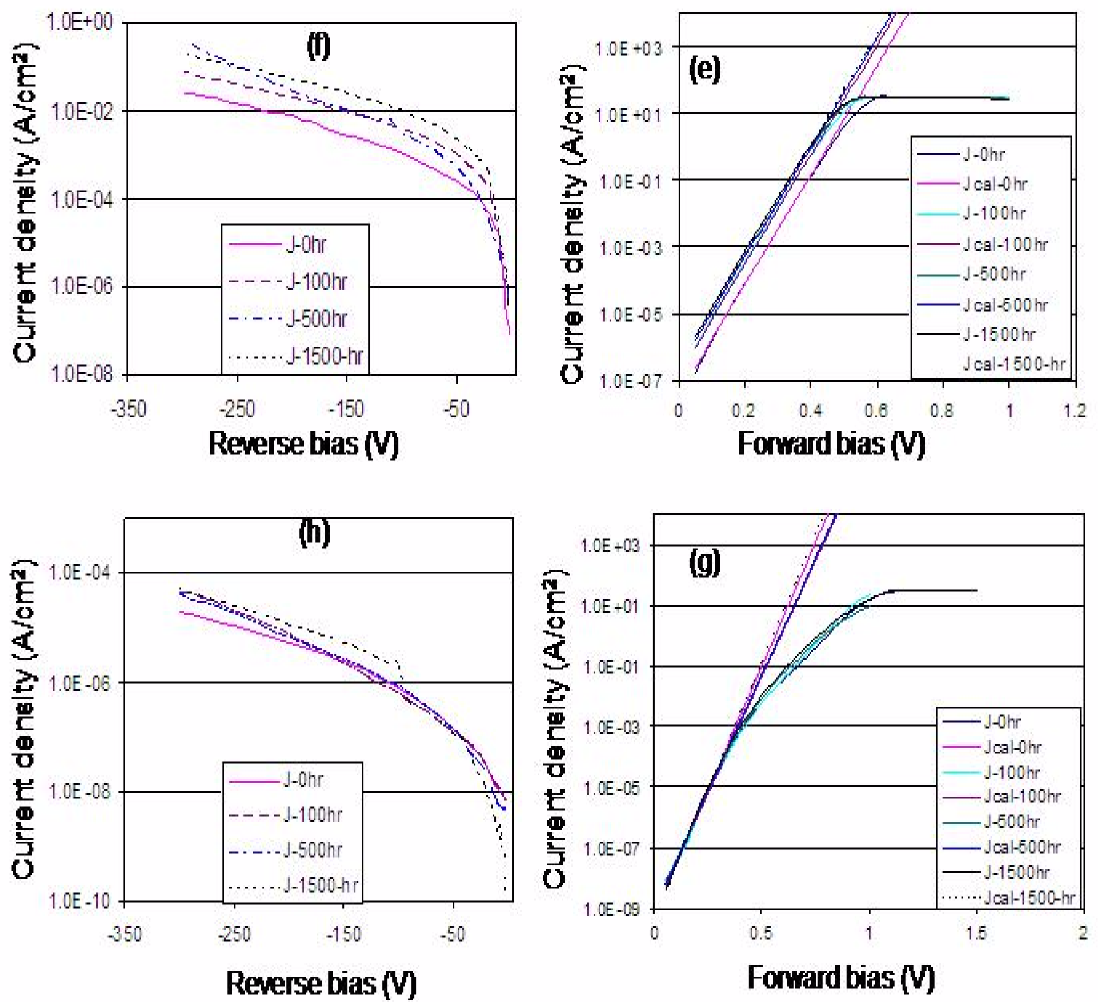

Figure 5.23: (e) Forward characteristics with 5% nitrogen (f) reverse characteristics with 5% nitrogen (g) forward characteristics with 10% nitrogen (h) reverse characteristics with 10% nitrogen.

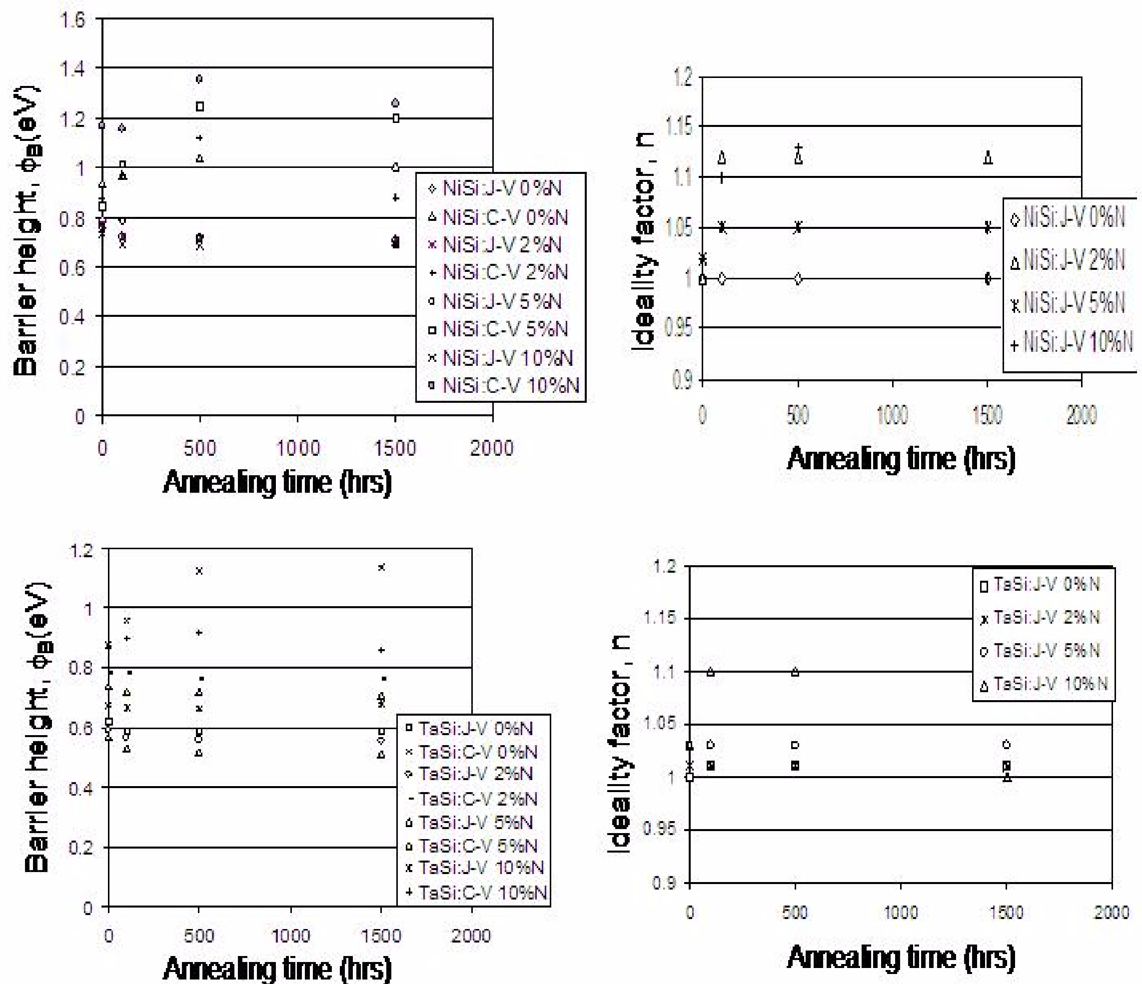

Figure 5.24: Nickel silicide Schottky devices (a) barrier height against annealing time (b) ideality factor against annealing time. Ta-Si-N Schottky devices (c) barrier height against annealing time (d) ideality factor against annealing time.

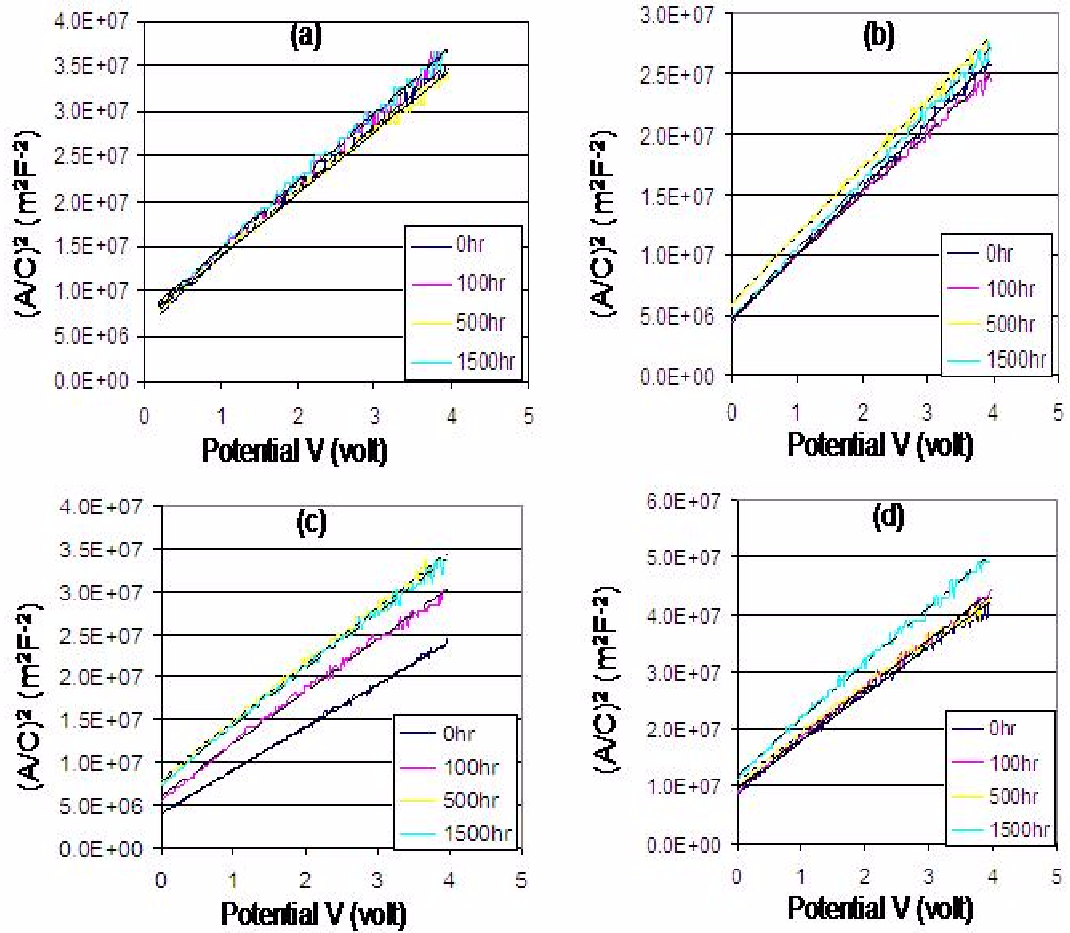

Figure 5.25: Plots of $(A/C)^2$ against applied bias for nickel silicide diodes with (a) 0% nitrogen (b) 2% nitrogen (c) 5% nitrogen (d) 10% nitrogen content in the metallization stack.

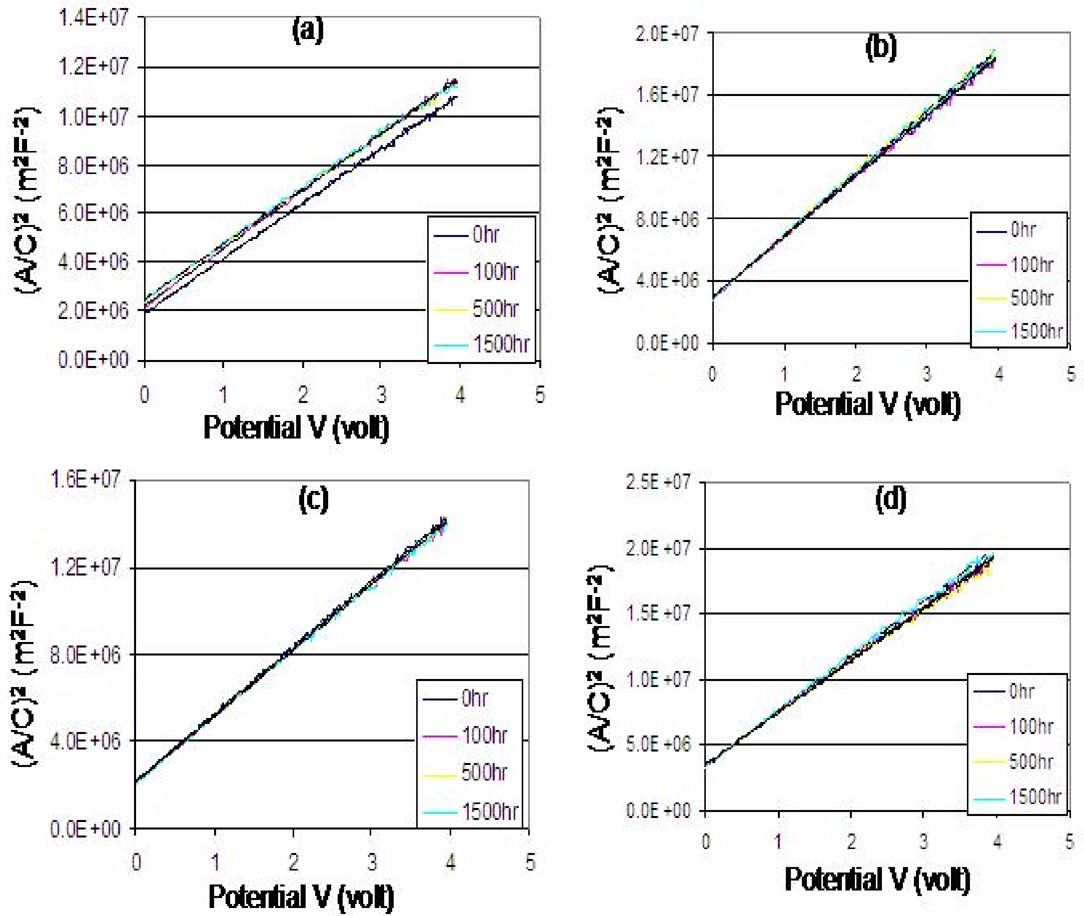

Figure 5.26: Plots of $(A/C)^2$ against applied bias for Ta-Si-N diodes with (a) 0% nitrogen (b) 2% nitrogen (c) 5% nitrogen (d) 10% nitrogen content in the metallization stack.

calculated from the intercept on the potential axis using the equation,

$$\phi_B = V_i + \frac{kT}{q}(1 + \ln(\frac{N_c}{N_D})) \tag{5.2}$$

where for 4H-SiC, $N_c \approx 4.82 \times 10^{15} M (m_c/m_o)^{3/2} T^{3/2} cm^{-3}$,

$m_c = 0.37 m_o$, the number of equivalent conduction band minima is M = 3.

Then for T = 300K, $N_c \approx 1.69 \times 10^{19} cm^{-3}$, and with the measured doping concentration of about $2.5 \times 10^{16} cm^{-3}$,

$E_c - E_F = (kT/q)(\ln(N_c/N_D) \approx 0.17 eV$ and $\phi_B \approx V_i + 0.20$

Figure 5.24 also shows the plot of the C-V barrier height versus the annealing time. The stability of the barrier height with annealing time supports the observed J-V characteristics though the barrier heights from the C-V measurements are higher compared to those from the J-V measurement. C-V data was obtained with the devices in depletion under reverse bias, while for the J-V characteristics, the barrier height was determined with the devices forward biased.

RBS and AES spectra for the Schottky contacts are shown in figure 5.27. Neither significant inter-diffusion nor oxidation of the contacts was observed. However, moverment of carbon within the stack was observed from the AES data.

5.4 Wirebonding and Brazing Results

5.4.1 Chip Shear Testing

Adhesion within the metallization stack as well as adhesion of the stack to thermal SiO_2 (indirect bonding) and to ohmic and Schottky devices (direct bonding) are essential parts of this study. Indications of adhesion problems were first noticed while brazing the Ta-Si-N/Pt-N/Au/Sn/Au stack to a thermal oxide. Though Ta-Si-N has good adhesion to SiO_2, the adhesion

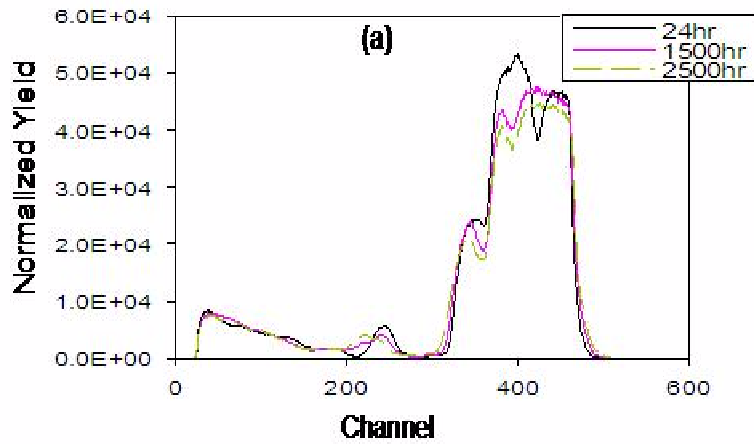

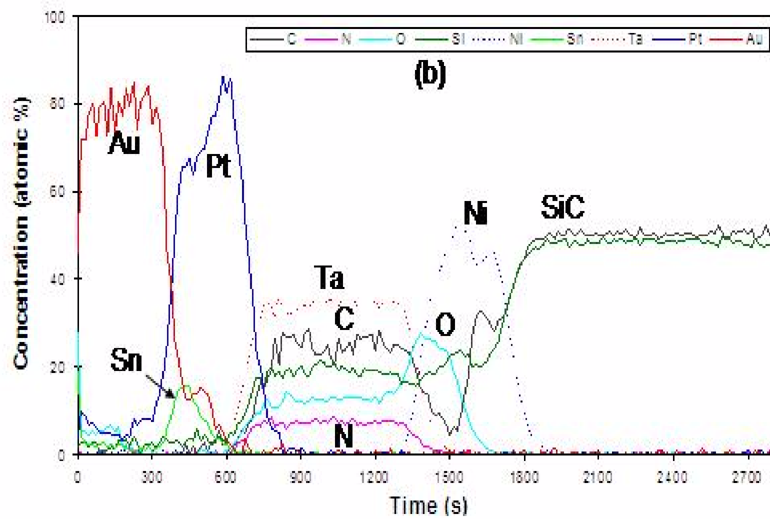

Figure 5.27: Nickel silicide Schottky contacts with 2% nitrogen in the metallization stack (a) RBS spectra (b) AES spectra after 1500hr anneal in air.

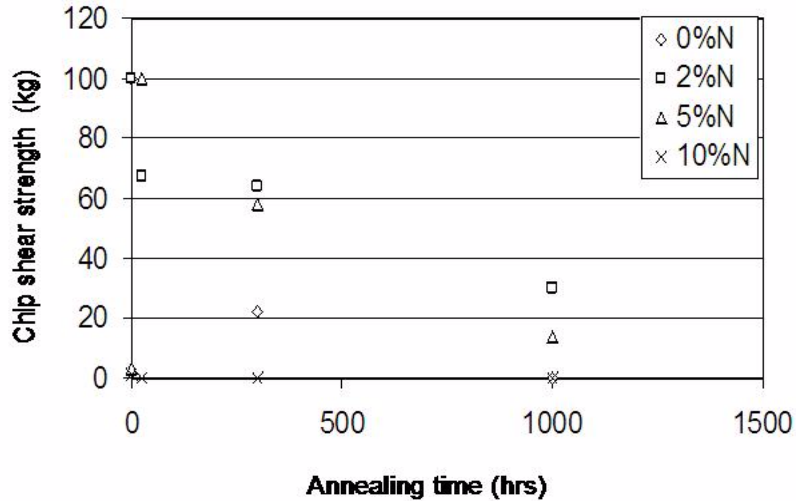

Figure 5.28: Chip shear strength with cold Pt in the metallization stack against annealing time.

of the brazed $5mm \times 5mm$ samples on their ceramic holders degraded significantly in air at $350°C$. Figure 5.28 shows the initial brazing results that indicates that high nitrogen content in the stack may be detrimental to adhesion.

RBS spectra of a sheared sample showed the interface between Ta-Si-N and Pt is the weakest link in the metallization stack. This adhesion was significantly increased when Pt was sputter-deposited on SiC/SiO_2/Ta-Si-N at $250°C$. With hot Pt, adhesion was very good, and the stack did not fail under maximum shear force (100 kg). The adhesion remain excellent with annealing time up to 1000hrs. Samples that passed the shear testing were subjected to additional shear testing after further annealing in air. The stress incurred during the first shear testing seems to heal with further annealing.

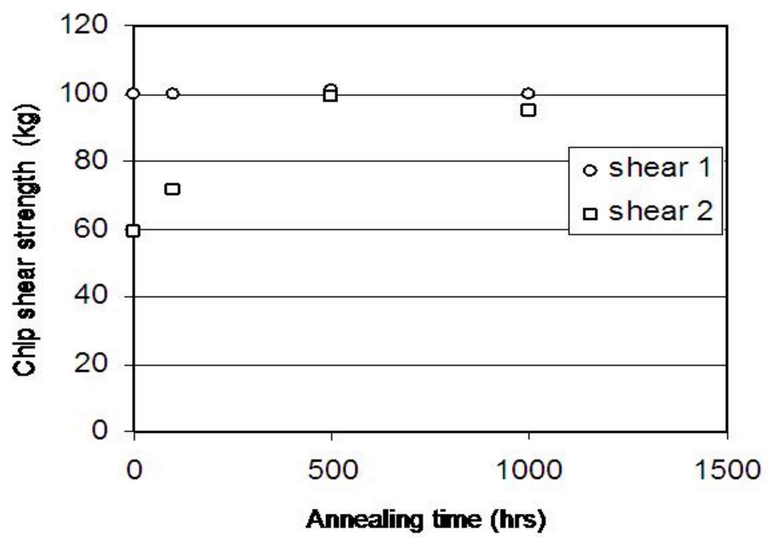

Figure 5.29: Chip shear strength with hot Pt and 2% nitrogen in the metallization stack against annealing time.

5.4.2 Wirebond Pull and Shear Testing

Bond pull and shear testing were carried out on the following metallization structures: SiC/SiO_2/Ta-Si-N/Pt-N/Au (indirect wirebonding), SiC/Ni-Si(ohmic)/Ta-Si-N/Pt-N/Au, SiC/NiSi(Schottky)/Ta-Si-N/Pt-N/Au. Metallizations with hot Pt on thermal SiO_2 and NiSi Schottkys held up very well. 100% of the time, it was the Au wire that broke while doing pull testing, and for the shear testing, the separation of the wirebond from the samples was above the Au cap layer on the samples. Figure 5.30(a) shows the bond pull and shear strengths against the time of annealing for the samples. The breaking mode of the Au wire during pull testing and shear testing are shown in figure 5.30(c).

Wirebond pull and shear tests results were not as good for hot Pt stacks deposited directly on annealed nickel ohmic contacts. Many bonds failed at the interface between the ohmic contact and the Ta-Si-N layer. The reason for the failure was attributed to carbon liberated during the contact anneal and left on the surface of the nickel silicide layer. The RBS and AES results in figures 5.31 and 5.32 show that a thin layer of carbon was left on the silicide surface for a starting nickel thickness of about 120nm. The carbon was primarily surface carbon, but there is considerable carbon thoughout the nickel silicide layer as well. Figures 5.31 and 5.32 also show that the surface carbon can be removed through either oxygen plasma etching or by ion milling with a low energy Ar beam (1keV, 5-8 minutes). The ratio of nickel to carbon at the surface of as-annealed contacts was about 1:2. On Ar ion cleaned samples the ratio was about 5:4 and on the oxygen etched samples it was about 3:1.

The result of cleaning showed that both cleaning procedures remove surface carbon; however, the Ar ion clean also removed a thin layer of left over nickel during incomplete ohmic

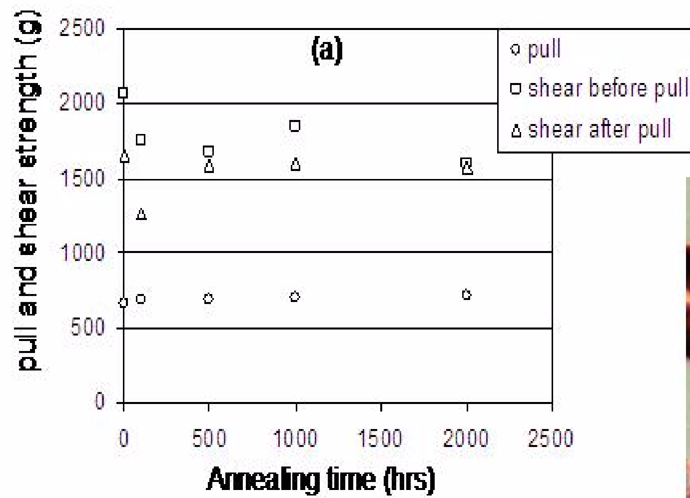

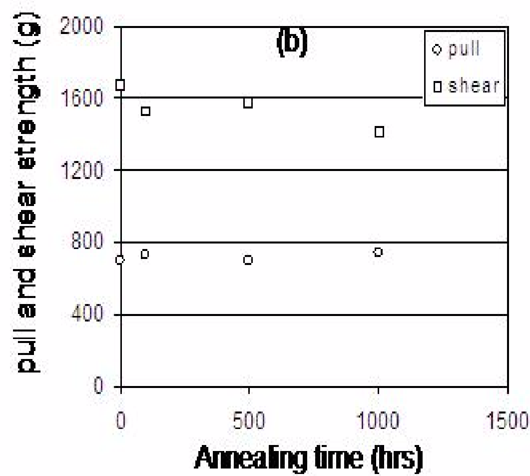

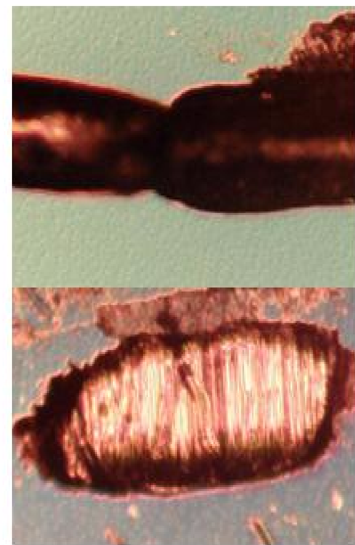

Figure 5.30: Wirebond pull and shear strengths against annealing time for (a) metallization with 2% nitrogen and hot Pt on a thermal oxide (b) metallization stack with 2% nitrogen and hot Pt on a nickel silicide Schottky contact (c) Au wire failure mode and sheared wedged bond.

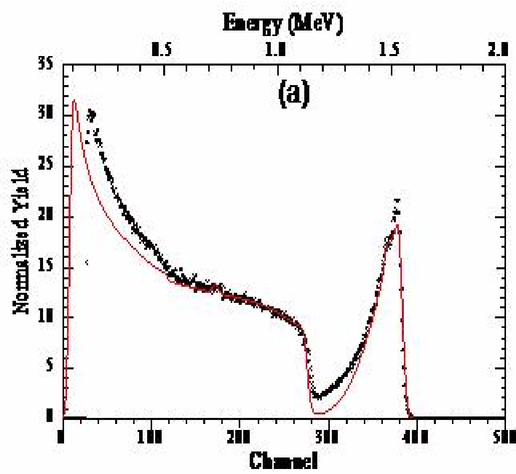

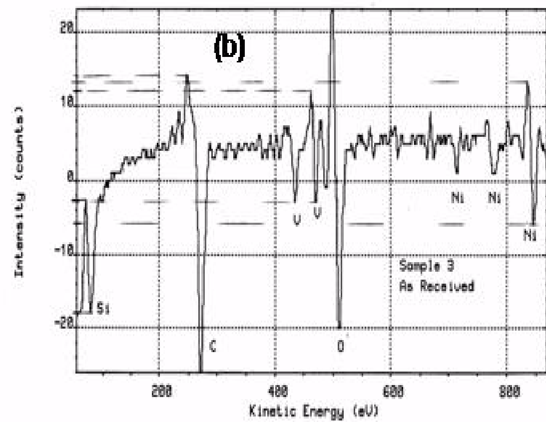

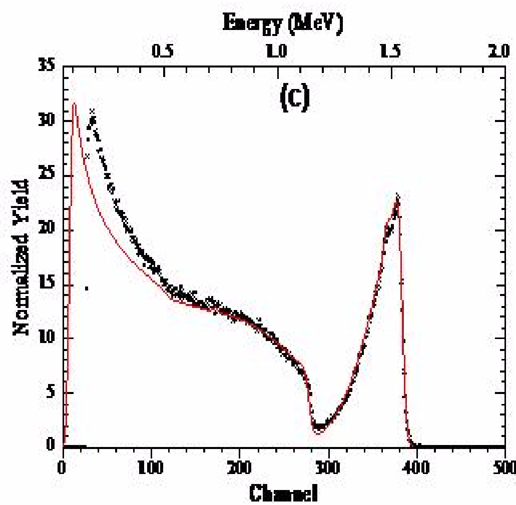

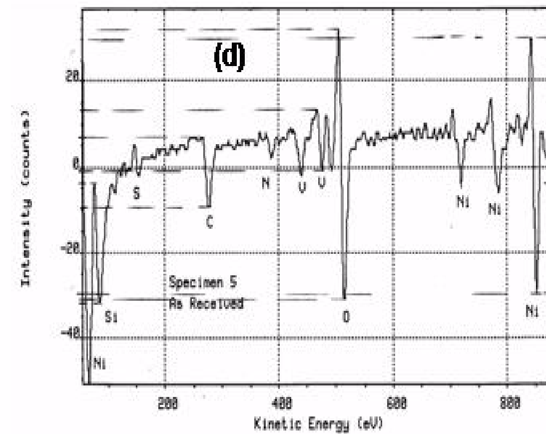

Figure 5.31: RBS and AES results for nickel ohmic contacts (a) RBS of ohmic annealed contacts (b) AES of ohmic annealed contacts (c) RBS of RIE cleaned ohmic contacts (d) AES of RIE cleaned ohmic contacts

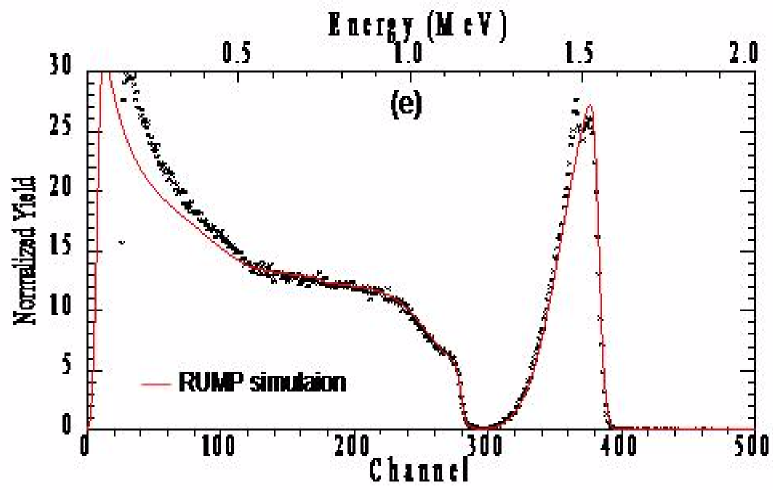

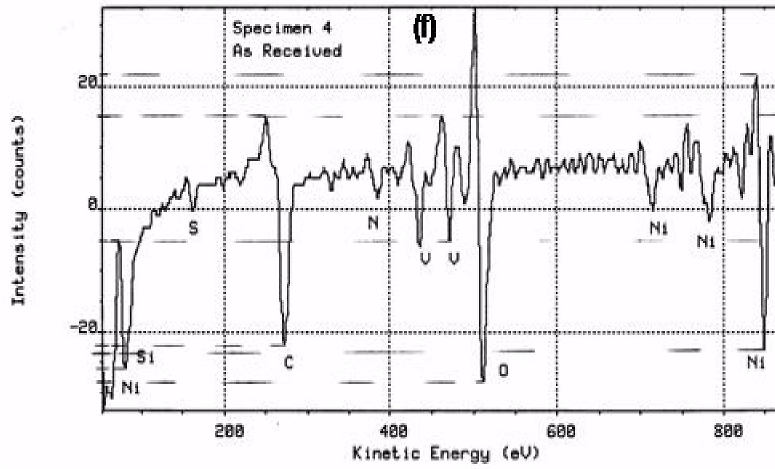

Figure 5.32: RBS and AES results for nickel ohmic contacts (a) RBS of Ar ion cleaned ohmic contacts (b) AES of Ar ion cleaned ohmic contacts.

contact annealing. Oxygen RIE could not remove the nickel which is sometimes used as protective mask during oxygen RIE. The result of wirebond pull and shear testing showed that RIE sample did not show much improvement in adhesion because of the unreacted nickel. However, for the samples cleaned using Ar, where both carbon and nickel surface layers were removed, there is significant improvement in the adhesion as shown in figure 5.33. At 1000hr annealing, the adhesion is still good. Pictures of failed metallization on nickel ohmic contacts are included in figure 5.33. Direct wirebond pull and shear test results on annealed 80-20 wt% Ni-Cr or as-deposited Ni with hot Pt were also not good as a result of the same problems described for the annealed nickel contacts.

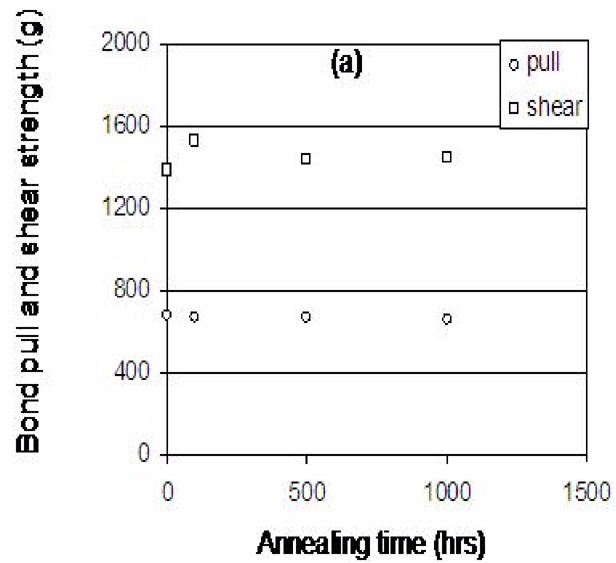

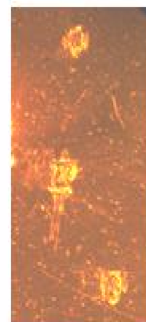

Figure 5.33: (a) wirebond pull and shear strength of Ar ion cleaned nickel ohmic contacts (b) picture of failed wirebond and (c) picture of good pull and shear bonding.

Chapter 6

Conclusions

Various ohmic contacts were fabricated in this study, and fabrication conditions were optimized to obtain very low specific contact resistance. Low contact resistance is essential to minimize power losses in high voltage/high current devices. Specific contact resistances in the range 1.1×10^{-3} to $6.9 \times 10^{-6} \Omega - cm^2$ were obtained.

RBS results showed that of four silicides studied for use as diffusion/oxidation barriers, tantalum silicide sputter-deposited from $TaSi_2$ was more resistant to oxidation and more effective as a diffusion barrier compared to Ta_5Si_3, molybdenum silicide and tungsten silicide. Even with Pt cap layers, Mo-Si and W-Si oxidize because of oxygen diffusion through the cap layers.

Tantalum silicide sputter-deposited from $TaSi_2$ in an Ar/N_2 gas mixture has lower sheet resistance compared to tantalum silicide from Ta_5Si_3. The sheet resistance of Ta-Si-N increases with increasing nitrogen content in the films. Ta-Si-N films with 0, 2, 5 and 10% by nitrogen flow rate in the sputter-gas were amorphous as-deposited, and they remain amorphous after annealing for 750 hours in air or vacuum at $350°C$. It was observed from XRD that increasing nitrogen content in the films made them more amorphous. The Ta-Si-N films are resistant to oxidation and amorphous with good diffusion barrier characteristics, so that they are suitable for the job of protecting ohmic and Schottky contacts operating at elevated temperature in air.

The protective metallization stack, Ta-Si-N/Pt-N/Au, was found to be very effective on ohmic or Schottky contacts annealed in air at $350°C$. Physical characterization (AES and RBS) showed that the protective metallization stack prevents rapid oxidation of the contacts and minimizes inter-diffusion/mixing within the contact/stack combination. RBS data after 4000 hour

anneals in air at 350°C and AES data after 1500 hours were analyzed for signs of oxidation and diffusion.

For ohmic contacts however, carbon generated during the high temperature ohmic contact anneal is very mobile, and it diffuses through the barrier layers, especially those with zero nitrogen content. Barrier layers with 2% nitrogen are much more resistant to carbon diffusion. For p^+ implanted 4H-SiC, the movement or accumulation of carbon does not affect the electrical characteristics (specific contact resistance and SiC sheet resistance) significantly. But for n^+ epitaxial SiC, the total contact-to-contact resistance between TLM adjacent pads increased significantly with increasing anneal time in air. The conclusion was that carbon accumulation/diffusion increased the resistance of the contact. The effect noticeable because initially, the contact-to-contact resistances for the n-epilayers were much lower than for the p^+ implanted material.

For Schottky devices, J-V characteristics and C-V characteristics were largely stable with annealing time. Ta-Si-N Schottky devices had higher reverse leakage currents than the nickel silicide Schottky devices. Barrier heights and ideality factors were determined from the J-V and C-V measurements by fitting the experimental data to theoretical transport equations. The barrier height from the J-V data were lower compared to the C-V data, and the barrier heights of Ta-Si-N Schottky devices were lower than those of the nickel silicide devices. This accounts for the higher leakage currents of the Ta-Si-N devices. Increasing nitrogen content in Ta-Si-N Schottky contact improves the stability of the barrier height and ideality factor with annealing time in air. Without the protective stack, oxidation of nickel silicide Schottky contact and Au diffusion into the contact was obvious after just 24 hours of annealing in air at 350°C.
Adhesion tests carried out on the samples resulted in the following observations.

1. Initial die attach shear testing showed degraded adhesion with annealing time in air and with

increased nitrogen content in the metallization stack.

2. Sputter-deposition of Pt at 250°C increased adhesion, with die shear strengths above the maximum possible of 100kg, for up to 1000 hour annealing in air.

3. Hot Pt metallization stacks on SiO_2 (for the purpose of indirect wirebonding) were wirebonded with 10mil Au wire. Wirebond pull and shear testing showed that the adhesion with the stack was excellent, with no degradation for up to 2000 hour of annealing and testing.

4. Direct wirebonding on nickel silicide Schottky contacts with hot Pt stacks showed that adhesion was very good. Bond pull and shear test results were very stable for anneal times up to 1000 hours.

5. Direct wirebonding on annealed nickel ohmic contacts with hot Pt stacks resulted in poor adhesion. However, Ar ion cleaning the samples just after the ohmic contact anneal improved adhesion dramatically and produced bond pull and shear results that are very stable for 1000 hour anneals (longer anneals are currently underway). It was concluded that the problem of adhesion on the as-annealed ohmic contacts was due to the surface carbon and unreacted surface nickel left after the contact anneal.

More detailed studies of the differences between ohmic contact characteristics for implanted and epitaxial layers is essential. Also, further study of the ability of the Ta-Si-N barrier layer to prevent diffusion and oxidation at higher temperatures, say 400 - 500°C, would be informative. Modification of the ohmic contact anneal process by the introduction of a protective layer on the contact metal during the anneal or by the addition of a sticking layer between the ohmic contact and the barrier layer may prevent the need for Ar ion cleaning of the contacts before stack metallization. These options need to be investigated.

This study has been based on the application of a comprehensive set of characterization techniques - electrical (I-V, C-V, LTLM), physical (RBS, AES) and mechanical (wirebond pull

and shear testing). Based on the application of these techniques for the contact metallizations studied, the following recommendations can be made for the formation of composite, high temperature contacts to 4H-SiC:

- A protective stack, Ta-Si-N/Pt-N/Au, with 2% nitrogen content and Pt sputter-deposited at 250$^\circ C$, is an effective diffusion/oxidation barrier for ohmic and Schottky contacts operating in air at 350$^\circ C$.

- Sputter-deposited nickel ($\sim$ 100nm thick) annealed at 900$^\circ C$ for 1 minute in vacuum makes an acceptable ohmic contact for heavily doped p-4H-SiC ($N_A \geq 3 \times 10^{19} cm^{-3}$).

- Sputter-deposited 80-20 wt% Ni-Cr ($\sim$ 100nm thick) annealed at 1000$^\circ C$ for 2 minutes in vacuum can be used for ohmic contacts on n^+ epitaxial SiC.

- Sputter-deposited nickel silicide forms a stable Schottky contacts on n^- epitaxial SiC.

- Nickel silicide Schottky contacts with the protective stack can be wirebonded directly (on silicide) or indirectly (on SiO_2)

- Argon ion cleaned nickel and nickel-chromium ohmic contacts with the protective stack can be wirebonded directly. Without ion cleaning, indirect wirebonding is necessary.

BIBLIOGRAPHY

[1] Materials for high temperature semiconductor devices, *National Research Control Report NMAB-747* (National Academy Press, Washington, DC, 1995).

[2] J.R. Williams and R.W. Johnson, *Contact Metallization and Packaging Technology Development for SiC Bipolar Junction Transistors, PiN Diodes and Schottky Diodes Designed for Long-term Operation at* $350°C$ (Proposal submitted to Wright-Patterson Air Force Base, AFRL, 2001).

[3] G.L. Harris (ed.), *EMIS Data Reviews Series, No 13*, (Short Run Press, Exeter, England, 1995).

[4] T. Uemoto, *Jpn. J. Appl. Phys.* **34** L7 (1995).

[5] J. Crofton, P.G. McMullin, J.R. Williams and M.J. Bozack, *J. Appl. Phys.* **77 (3)** 1317 (1995).

[6] S. Liu, K. Reinhardt, J. Scofield and C. Severt, *Workshop on High Temperature Power Electronics for Vehicles* (April 1995).

[7] T. Nakata, K. Koga, Y. Matsushita, Y. Ueda and T. Niina, *Amorphous and Crystalline SiC II* (Springer Verlag, Berlin, 26 1989).

[8] A. Suzuki, Y. Fujii, H. Saito, Y. Tajima and K. Furukawa, *J. Cryst. Growth* **115** 623 (1991).

[9] J. Crofton, L. Beyer, J.R. Williams, E.D. Luckowski, S.E. Mohney and J.W. DeLucca, *Solid-State Electron.* **41 (1)** 1725 (1997).

[10] N. Braslau, *J. Vac. Sci. Technol.* **19** 803 (1981).

[11] J. Crofton, S.E. Mohney, J.R. Williams and T. Isaacs-Smith, *Solid-State Electron.* **46 (1)** 109-113 (2001).

[12] J. Feitknecht, ”Silicon carbide as a semiconductor” *Springer Tracts in Modern Physics* G. H*ö*hler (ed.), **58** 48 (1971).

[13] A.G. Acheson, *Brit. Pat.* 17911 (1892).

[14] O.W. Lossew, *Telegraphy and Telephony* **18** 61 (1923).

[15] G. Busch, *Helv. Phys. Acta* **19** 463 (1946).

[16] http://www.ecn.purdue.edu/WBG/introduction/index.html

[17] D. Nakamura, I. Gunjishima, S. Yamaguchi, T. Ito, A. Okamoto, H. Kondo, S. Onda and K. Takatori, ”ultrhigh-quality silicon carbide single crystal”, *Nature* **430** 1009 (2004).

[18] W.F. Knippenberg and G. Verspui, *Mat. Res. Bull.* **4** S.45 (1969).

[19] W.F. Knippenberg and G. Verspui, *Mat. Res. Bull.* **4** S.33 (1969).

[20] V.A. Izhevskyi, L.A. Genova, J.C. Bressiani, A.H.A. Bressiani, "Review article: SiC. structure, properties and processing", *Ceramica* **46 (297)** (2000)

[21] T.N. Oder, "Fabrication and Characterization of Ohmic Contact to P- and N-type SiC with applications to P-N Junction diodes", *Auburn University Doctoral thesis* (1999).

[22] R.S. Ramsdell, *Am. Min.* **32** 64-82 (1947).

[23] G.R. Zhadanov, *Compte Rende Acad. Sci. URSS* **48** 39-42 (1945).

[24] K. Järrendahl and R.F. Davis, *SiC Materials and Devices* Y.S. Park (ed), **52** 1-20 (1998).

[25] P.G. Neudeck, *Silicon Carbide Electronic Devices, in Encyclopedia of materials: Science and Technology* K.H.J. Bushchow, R.W. Cahn, M.C. Flemings, B. Ilschner, E.J. Kramer and S. Mahajan, (eds) (Oxford: Elsevier Science) **9** 8508-8519 (2001).

[26] W.F. Knippenberg, *Philips Res. Rept.* **18** 16 (1963).

[27] P.T.B. Shaffer, *Mat. Res. Bull.* **4** S.13 (1969).

[28] D.J. Larkin, P.G. Neudeck, J.A. Powell and L.G. Matus, "5th Int. Conf. on SiC and related Matls." (Washington, DC, USA, 1993); *Inst. Phys. Conf. Ser. No 137* 51 (1994).

[29] M.S. Shur, *SiC Materials and Devices* Y.S. Park (ed), **52** 161-193 (1998).

[30] Y. Wang, W. Xie, Jr.J.A. Cooper, M.R. Melloch and J.W. Palmour, *Silicon Carbide and Related Materials* S. Nakashima, H. Matsunami, S. Yoshida, H. Harima (eds), (IOP Publishing, Bristol, UK, 809-812, 1995).

[31] D.M. Brown, E. Downey, J. Kretchmer, V. Krishnamurthy, W. Hennessy and G. Michon, *Phys. Status Solidi (a)* **162** 459-479 (1997).

[32] http://www.ecn.purdue/WBG/Device_Research/Power_Devices/ Index.html

[33] J. Spitz, M.R. Melloch and J.A. Cooper, Jr., *IEEE Device Research Conference* (Ft. Collins, CO, June 23-25, 1997).

[34] J. Spitz, M.R. Melloch, J.A. Cooper, Jr., and M.A. Capano, *IEEE Electron Device Lett.* **19** 100 (1998).

[35] F. Dahiquist, C.M. Zetterling, M. Ostling, and K. Rottner, *Silicon Carbide, III-Nitrides, and Related Materials* (Materials Research Forum 264-8, Trans Tech, Switzerland) G. Pensl, H. Morkoc, B. Monemar, E. Janzen (eds), 1061-1064 (1998).

[36] R. Held, N. Kaminski, E. Niemann, *Silicon Carbide, III-Nitrides, and Related Materials* (Materials Research Forum 264-8, Trans Tech, Switzerland) G. Pensl, H. Morkoc, B. Monemar, E. Janzen (eds), 1057-1060 (1998).

[37] R.J. Trew, *SiC Materials and Devices* Y.S. Park (ed), **52** 237-282 (1998).

[38] http://www.ecn.purdue/WBG/Device_Research/Microwave_Devices/ Index.html

[39] R.C. Clarke, A.K. Agarwal, R.R. Siergiej, C.D. Brandt and A.W. Morse, *IEEE Device Research Conf.* (Santa Barbara, CA, June 24-26, 1996)

[40] S.A. Lloyd, A. Baranzahi, P. Tobias, and I. Lundstrom, *Phys. Status Solidi (a)* **162** 493-511 (1997).

[41] G. W. Hunter, P.G. Neudeck, L.Y. Chen, D. knight, C.C. Liu, and Q.H. Wu, *Silicon Carbide, III-Nitrides, and Related Materials* (Materials Research Forum 264-8, Trans Tech, Switzerland) G. Pensl, H. Morkoc, B. Monemar, E. Janzen (eds), 1093-1096 (1998).

[42] M. Mehregany, C. Zorman, N. Narayanan and C.H. Wu, *Proc. IEEE* **14** 1594-1610 (1998).

[43] V. Saxena and A.J. Steckl *SiC Materials and Devices* Y.S. Park (ed), **52** 77-151 (1998).

[44] R.F. Pierret *Semiconductor Device Fundamentals* (Addison-Wesley Publishing Company, Inc, 1996).

[45] M.J. Bozack *Phys. Stat. Sol. (b)* **202** 549-579 (1997).

[46] J. Crofton, L.M. Porter, and J.R. Williams *Phys. Stat. Sol. (b)* **202** 581-603 (1997).

[47] J. Bardeen *Phys. Rev.* **71** 717 (1947).

[48] http://www.stanford.edu/class216/handouts/6-MS%20contacts.pdf

[49] A.M. Cowley and S.M. Sze *J. Appl. Phys.* **36** 3212 (1965).

[50] E.H. Rhoderick *Metal-semiconductor contacts* (Oxford University Press, 1978).

[51] J. Crofton, P.G. McMullin, J.R. Williams and M.J. Bozack, *Trans. 2nd High Temperature Electronics Conf.* Charlotte (NC) XIII-15 (1994).

[52] S. liu, S.R. Smith, S. Adams, C. Severt and J. Leonad, *Trans. 2nd High Temperature Electronics Conf.* Charlotte (NC) XIII-9 (1994).

[53] G. Kelner, S. Binari, M. Shur and J.W. Palmmour *Electronic Lett.* **27** 1038 (1991).

[54] J. Crofton, J.M. Ferrero, P.A. Barnes, J.R. Williams, M.J. Bozack, C.C. Tin, C.D. Ellis, J.A. Spitznagel and P.G. McMullin, *Amorphous Crystalline Silicon Carbide IV* C.Y. Yang, M.M. Rahman and G.L. Harris (eds) (Springer-Verlag, Berlin, p.176 1992).

[55] J.W. Palmour, H.S. Kong, E.D. Waltz, J.A. Edmond, and C.H. Carter, *In: First International High Temperature Electronic Conf.* D.B. King and F.V. Thome (eds) (Albuquerque, NM, 1991).

[56] R.C. Glass, L.M. Spellman and R.F. Davis, *Appl. Phys. Lett.* **59** 2868-2870 (1991).

[57] R.C. Glass, L.M. Spellman, S. Tanaka and R.F. Davis, *J. Vac. Sci. Technol. A* **10** 1625-1630 (1992).

[58] L.M. Porter and R.F. Davis, *Mat. Sci. and Eng.* **B34** 83-105 (1995).

[59] R.N. Hall, *J. Appl. Phys.* **29** 914 (1958).

[60] J. Crofton, P.A. Barnes, J.R. Williams and J.A. Edmond, *Appl. Phys. Lett.* **62** 384-386 (1993).

[61] J. Crofton and P.A. Barnes, *J. Appl. Phys.* **69** 7660 (1991).

[62] J. Crofton, P.A. Barnes and M.J. Bozack, *Amer. J. Phys.* **60** 499 (1992).

[63] J.B. Petit, P.G. Neudeck, C.S. Salupo, D.J. Larkin and J.A. Powell, (presented at the Silicon Carbide and Related Materials Conf., Washington DC, 1993) M.G. Spencer, R.P. Devaty, J.A. Edmond, M.A. Khan, R. Kaplan and M. Rahman (eds), *Inst. of Phys. Conf. Ser.* **137**, Inst. of Phys. 679-682 1993.

[64] N. Lundberg and M. Ostling, *Solid State Electronics* **39** 1559 (1996).

[65] H. Daimon, M. Yamanaka, E. Sakuma, S. Misawa and S. Yoshida, *Jpn. J. Appl. Phys.* **25** L592-L594 (1986).

[66] J.A. Edmond, J. Ryu, J.T. Glass and R.F. Davis, *J. Electrochem. Soc.* **135** 359-362 (1988).

[67] A.J. Steckl and J.N. Su, *IEDM* 695-698 (1993).

[68] H.J. Cho, C.S. Hwang, W. Bang, and H.J. Kim, (presented at the Silicon Carbide and Related Materials Conf., Washington DC, 1993) M.G. Spencer, R.P. Devaty, J.A. Edmond, M.A. Khan, R. Kaplan and M. Rahman (eds), *Inst. of Phys. Conf. Ser.* **137**, Inst. of Phys. 663 1993.

[69] T.B. Massalski, H. Okamoto, P.R. Subramanian and L. Kacprzak (eds), *Binary Alloy Phase Diagrams* **2** (ASM International, Materials Park, OH 1990).

[70] J.S. Shor, R.A. Weber, L.G. Provost, D. Goldstein and A.D. Kurtz, *J. Electrochem. Soc.* **141** 579-581 (1994).

[71] C.A. Mead, and W.G. Spitzer, *Phys. Rev.* **134**(3A) A713-A716 (1964).

[72] C.A. Mead, *Solid State Electronics* **9** 1023-1033 (1966).

[73] S.H. Hagen, *J. Appl. Phys.* **39**(3) 1458-1461 (1968).

[74] S. Yoshida, K. Sasaki, E. Sakuma, S. Misawa and S. Gonda, *Appl. Phys. Lett.* **46** 766-768 (1985).

[75] J.R. Waldrop, and R.W. Grant, *Appl. Phys. Lett.* **56** 557-559 (1990).

[76] P. Shenoy, A. Moki, B.J. Baliga, D. Alok, K. Wongchotigul and M. Spencer, in:*Tech. Digest Intl. Electron Dev. Meeting, IEEE Cat. No.* **94CH35706** 411-414 (1994).

[77] A. Itoh, T. Kimoto and H. Matsunami, *IEEE Electron Dev. Lett.* **16** 280-282 (1995).

[78] A. Itoh, T. Kimoto and H. Matsunami, (in Silicon Carbide and Related Materials VI - Kyoto 1995) *Inst. of Phys. Conf. Ser.* **142** 689-692 (1995).

[79] A. Itoh, T. Kimoto and H. Matsunami, *IEEE Electron Dev. Lett.* **17** 139-141 (1996).

[80] R. Raghunathan, D. Alok and B.J. Baliga, *IEEE Electron Dev. Lett.* **16** 226-227 (1995).

[81] C.E. Weitzel, J.W. Palmour, C.H. Carter, K. Moore, K.J. Nordquist, S. Allen, S. Thero and M. Bhatnagar, *IEEE Trans. Electron Dev.* **43** 1732-1741 (1996).

[82] V. Saxena and A.J. Steckl, in: *International Semiconductor Device Research Symposium* 539-542 (1997).

[83] V. Saxena and A.J. Steckl, (in: Silicon Carbide, III-Nitrides and Related Materials VII - Stockholm 1997) G. Pensl, H. Morkoc, B. Monemar and E. Janzen (eds) *Materials Science Forum* **264** 937-940 (1998).

[84] J.N. Su and A.J. Steckl, (Workshop on High Temperature Power Electronics - Ft. Monmouth, NJ) 50-53 (1995).

[85] A. Itoh, T. Kimoto and H. Matsunami, (in Silicon Carbide and Related Materials VI - Kyoto 1995) *Inst. of Phys. Conf. Ser.* **142** 697-700 (1996).

[86] V. Saxena, A.J. Steckl, M. Vichare, M.L. Ramalingam and K. Reinhardt, in: *Third Intl. High Temp. Electronic Conf. - Albuquerque* **1** VII/15-20 (1996).

[87] J. Crofton, E.D. Lukowski, J.R. Williams, T. Isaacs-Smith, M.J. Bozack, and R. Siergiej, (in: Silicon Carbide and Related Materials VI - Kyoto 1995) *Inst. of Phys. Conf. Ser.* **142** 569-572 (1996).

[88] C. Arnodo, S. Tyc, F. Wyczisk and C. Brylinski, (in Silicon Carbide and Related Materials VI - Kyoto 1995) *Inst. of Phys. Conf. Ser.* **142** 577-580 (1996).

[89] D. Alok, B.J. Baliga and P.K. Mclarty, *IEDM* 691-694 (1993).

[90] M.M. Anikin, M.G. Rastegaeva, A.L. Syrkin and I.V. Chuiko, *Amorphous Crystalline Silicon Carbide III - Springer-Verlag, Berlin* G.L. Harris, M.G. Spencer and C.Y. Yang (eds) **56** 183-189 (1992).

[91] J. Crofton, J.R. Williams, M.J. Bozack and P.A. Barnes, *Inst. of Phys. Conf. Ser.* **137** 719 (1994).

[92] J.B. petit, P.G. Neudeck, C.S. Salupo, D.J. Larkin and J.A. Powell, *Inst. of Phys. Conf. Ser.* **137** 679 (1994).

[93] S. Liu, K. Reinhardt, C. Severt and J. Scofield (in Silicon Carbide and Related Materials VI - Kyoto 1995) *Inst. of Phys. Conf. Ser.* **142** 589-592 (1996).

[94] A.K. Chaddha, J.D. Parsons, and G.B. Kruaval, *Appl. Phys. Lett.* **66** 760 (1995).

[95] J.S. Shier, *J. Appl. Phys.* **41** 771-773 (1970).

[96] J. Crofton, P.A. Barnes and J.R. Williams, *Appl. Phys. Lett.* **62** 384-386 (1993).

[97] L. Spiess, O. Nennewitz and J. Petzoldt, *Inst. of Phys. Conf. Ser.* **142** 585 (1996).

[98] N. Nordell, S. Savage and A. Schönder *Inst. of Phys. Conf. Ser.* **142** 573 (1996).

[99] M.I. Chaudhry, W.B. Berry and M.V. Zeller, *Int. J. Electronics* **71** 439-444 (1991).

[100] J.S. Chen, A. Bachli, M.-A. Nicolet, L. Baud, C. Jaussaud and R. Madar, *Mat. Sci. Eng. B* **29** 185-189 (1995).

[101] V. Kumar, L. Zhou, D. Selvanathan and I. Adesida, *J. Appl. Phys.* **29** (3) 1712-1714 (2002).

[102] J.M. Harris, E. Lugujjo, S.U. Capisano, M.-A. Nicolet and R. Shima *J. Vac. Sci. Technol.* **12** 524 (1975).

[103] J. Imahori, T. Oku and M. Murakami *Thin Solid Films* **301** 142 (1996).

[104] T. Oku, E. Kawakami, M. Uekebo, K. Takahiro, S. Yamaguchi and M. Murakami, *Appl. Surf. Sci.* **99** 265 (1996).

[105] J. Kwak, H.-K. Baik, J.-H. Kim and S.-M. Lee, *Appl. Phys. Lett.* **72** 2832 (1998).

[106] Y.-J. Lee, B.-S. Shu, S.-K. Rha and C.-O. Park *Thin Solid Films* **320** 141 (1998).

[107] E.D. Luckowski, J.M. Delucca, J.R. Williams, S.E. Mohney, M.J. Bozack, T. Isaacs-Smith and J. Crofton, *J. Electron. Mat.* **27** 330-334 (1998).

[108] R.S. Okojie, D. Lukco, Y.L. Chen, S. Spry and C. Salupo, *Mater. Res. Soc. Symp. Proc.* **423** 137 (2001).

[109] T. Laurila, K. Zeng, J.K. Kivilahti, J. Molarius, T. Riekkinen and I. Suni *Microelectronics Engineering* **60** 71-80 (2001).

[110] P.J. Pokela, C.-K. Kwok, E. Kolawa, S. Raud and M.-A. Nicolet, *Appl. Surf. Sci.* **53** 364-372 (1991).

[111] J. Molarius, T. Laurila, T. Riekkinen, K. Zeng, A. Niskanen, M. Leskela, I. Suni and J.K. Kivilahti *Advanced Metallization Conference* D. Edelstein (ed) (Proceedings of the conference), 355-359 (2000).

[112] J.S. Reid, E. Kolawa, R.P. Ruiz and M.-A. Nicolet *Thin Solid Films* **236** 319-324 (1993).

[113] J.S. Reid, X. Sun, E. Kolawa and M.-A. Nicolet *IEEE Electron Device Letters* **15** (8) 298-300 (1994).

[114] N.A. Papanicolaou, W.T.Jr. Anderson and A. Christou *Inst. Phys. Conf. Ser.* **65** 407 (1983).

[115] I. Suni, Mäenää, M.-A. Nicolet and M. Luomajärvi, *J. Electrochem. Soc.* **103** 1215 (1983).

[116] M. Östling, S. Nygren, C.S. Peterson, H. Norström, P. Wiklund, R. Buchta, H.-O. Blom and S. Berg, *J. Vac. Sci. Technol.* **A2** 281 (1984).

[117] J.R. Shappirio, J.J. Finnegan, R.A. Lux and D.C. Fox, *Thin Solid Films* **119** 23 (1984).

[118] D. Gupta, *Diffusion Phenomena in Thin Films and Microelectronic Materials* D. Gupta and P.S. Ho (eds) (Noyes publication, USA, 1 1988).

[119] L. Tian, M.O. Thompson, R. Dieckmann, C-Y Hui and Y-Y Lin, *J. Appl. Phys.* **90** (8) 3799-3808 (2001).

[120] L.G. Harrison, *Trans. Faraday Soc.* **57** 1191 (1961).

[121] D. Gupta, *Phys. Rev.* **7** 586 (1973).

[122] D. Gupta, *J. Appl. Phys.* **44** 4455 (1973).

[123] J. Shao and C.A. Angell, *Diffusion in Amorphous Materials* H. Jain and D. Gupta (eds) (Proceedings of an International Symposium, Pittburgh, USA, 1 1994).

[124] Y. Limoge, J.M. Delaye and J.L. Bocquet, *Diffusion in Amorphous Materials* H. Jain and D. Gupta (eds) (Proceedings of an International Symposium, Pittburgh, USA, 79 1994).

[125] Y. Limoge, G. Brebec and Y. Adda, *Trans. Tech. Pub.*, F.J. Kedves and D.L. Beke (eds), 285 1982.

[126] Y. Limoge, *Diffusion in Materials*, L. Laskar, G. Brebec, J.L. Bocquet and C. Monty (eds), (Nato ASI Series, Kluwer Acad. Press, 601 1990).

[127] Y. Limoge, *Defect and Diffusion Forum*, **83** 145 (1992).

[128] J.W. Haus and K.W. Kehr, *Physics Reports*, **150** 5-6 (1987).

[129] T. Laurila, *Tantalum-based diffusion barriers for copper metallization*, (Dissertation, Helsinki Univ. of Tech., Finland, 2001).

[130] L. Darken and R. Gurry, (Physical Chemistry of Metals, McGraw-Hill, 1953).

[131] E.A. Guggenheim, (Thermodynamics, Elservier Science, The Netherlands, 1967).

[132] E. Kolawa, J.S. Chen, J.S. Reid, P.J. Pokela and M.-A. Nicolet, *J. Appl. Phys.*, **70** (3) 1369-1373 (1991).

[133] J.D. Wiely, J.H. Perepezko, J.E. Nordman and K.-J. Guo, *IEEE Trans. Ind. Electron.*, **29** (1982).

[134] M.-A. Nicolet, I. Suni and M. Finetti, *Solid State Technol.*, **29** 129 (1983).

[135] L.S. Hung, F.W. Saris, S.Q. Wang and J.W. Mayer, *J. Appl. Phys.*, **59** 2416 (1986).

[136] Y.-J. Lee, B.-S. Suh and C.-O. Park, *Thin Solid Films*, **357** 237-241 (1999).

[137] E.R. Weber, *Appl. Phys. A*, 1 (1983).

[138] A. Broniatowski, *Phys. Rev. Lett.*, **62** 3074 (1989).

[139] M.-A. Nicolet, *Thin Solid Films*, **54** 415 (1978).

[140] J.W. Mayer and S.S. Lau, *Electronic Materials Science: For Integrated circuits in Si and GaAs*, (Macmillan publishing company, NY 1990).

[141] M.-A. Nicolet, *Diffusion in Amorphous Materials* H. Jain and D. Gupta (eds) (Proceedings of an International Symposium, Pittburgh, USA, 225 1994).

[142] M. Azuma, Y. Nakato and H. Tsubomura, *J. Electroanal. Chem.*, **255** 179 (1988).

[143] X. Sun, E. Kolawa, J.S. Chen, J.S. Reid and M.-A. Nicolet, *Thin Solid Films*, **236** 347 (1993).

[144] M. Thuillard, T.W. Workman, E. Kolawa and M.-A. Nicolet, *Jrnl Less-Common Metals*, **145** 505 (1988).

[145] K. Affolter, H. Kattelus and M.-A. Nicolet, *Mat. Res. Soc. Symp. Proc.*, **47** 167 (1985).

[146] J.A. Cunningham, C.R. Fuller and C.T. Haywood, *IEEE Trans. Reliab.*, **19** 182 (1970).

[147] M.L. Green, M.E. Gross, L.E. Papa, K.J. Schnoes and D. Brasen, *J. Electrochem. Soc.*, **132** 2677 (1985).

[148] K. Tominaga, T. Murayama, I. Mori, T. Okamoto, K. Hiruta, T. Moriga and I. Nakabayashi, *Vacuum*, **59** 546 (2000).

[149] R.B.H. Tahar, T. Ban, Y. Ohya and Y. Takahashi, *J. Appl. Phys.*, **83** 2631 (1998).

[150] Y. Abe, K. Kato, M. Kawamura and K. Sasaki, *Jpn. J. Appl. Phys.*, **39** 245 (2000).

[151] D.K. Schroder, *Seminconductor Material and Device Characterization*, (John Wiley and Sons, Inc. 1990).

[152] L.J. van der Pauw, *Phil. Res. Rep.*, **13** 1-9 (1958).

[153] L.J. van der Pauw, *Phil. Tech. Rev.*, **20** 220 (1958).

[154] R. Chwang, B.J. Smith and C.R. Crowell, *Solid-State Electron.*, **17** 1217 (1974).

[155] E.H. Rhoderick and R.H. Williams, *Metal-Semiconductor Contacts*, (2nd ed. Clarendon, Oxford, 1988).

[156] A.Y.C. Yu, *Solid-State Electron.*, **13** 239 (1970).

[157] F.A. Padovani, in: *Semiconductors and Semimetals*, R.K. Willardson and A.C. Beer (eds.), (Academic Press, New York **7A** 75 1971).

[158] F.A. Padovani and R. Stratton, *Solid-State Electron.*, **9** 695 (1966).

[159] G.K. Reeves and H.B. Harrison, *IEEE Electron Device Letters*, **EDL-3** (5) 111 (1982).

[160] http://ece-www.colorado.edu/ bart/book/book/chapter3/pdf/ ch3_5_3.pdf

[161] H.B. Harrison, *Proc. IREE Aust.*, **41** 95 (1980).

[162] N.T. Tam and T. Chot, *Phys. Stat. Sol.*, **93a** K91 (1986).

[163] N. Toyama, *J. Appl. Phys.*, **63** 2720 (1988).

[164] A.M. Goodman, *J. Appl. Phys.*, **54** 922 (1963).

[165] E.H. Rhoderick, *J. Phys. D: Appl. Phys.*, **5** 1920 (1972).

[166] L.C. Feldman and J.W. Mayer *Fundamentals of Surface and Thin Film Analysis*, (Elsevier Science Pub. Co., Inc. 1986).

[167] W.-K. Chu, J.W. Mayer and M.-A. Nicolet, *Backscattering Spectrometry*, (Academic Press, Inc. 1978).

[168] http://www.physics.auburn.edu/ condmatt/accellab.html

[169] National Electrostatics Corporation. Instruction Manual for Operation and Service: Charge Exchange RF Source, Model 2JA002110.

[170] R.J. Girnius and L.W. Anderson, *Nuclear Instruments and Methods*, **137** 373 (1976).

[171] http://www.pelletron.com/charging.htm

[172] G.F. Knoll, *Radiation Detection and Measurement*, (Wiley, 1979).

[173] D.F. Stein, *Auger Electron Spectroscopy*, C.L. Briant and R.P. Messmer (eds.) (Academic Press, Inc. 1988).

[174] M. Thomson, M.D. Baker, A. Christie and J.F. Tyson, *Auger Electron Spectroscopy*, (John Willey and Sons, Inc. **74** 1985).

[175] ”Handbook of Auger Electron Spectroscopy” A reference book of standard data for identification and interpretation of Auger electron spectroscopy data. 2nd ed. L.E. Davis, N.C. MacDonald, P.W. Palmberg, G.E. Riach and R.E. Weber, (Physical Electronic Industries, Inc. 1978).

[176] R.D. Tarey, R.S. Rastogi and K.L. Chopra, *The Rigaku Journal*, **4** (1/2) 11 (1987).

[177] M.F. Toney, *X-Ray Diffraction in Encyclopedia of Materials Characterization: surfaces, interfaces, thinfilms.*, C.R. Brundle and C.A. Evans (eds.) 198 (1992).

[178] A. Shegmuller, I.C. Noyan and V.S. Sperious, *Prog. Cryst. Growth and Charact.*, **18** 21 (1989).

[179] D. Rafaja, *Adv. in Solid State Phys.*, **41** 275 (2001).

[180] B.D. Cullity and S.R. Stock, *Elements of X-Ray Diffraction*, (3rd ed. Prentice-Hall, Inc. 2001).

[181] R.W. Johnson, *Professional Development Course*, (HiTEC 2004, Santa Fe, New Mexico, 2004).